CHALMERS
UNIVERSITY OF TECHNOLOGY

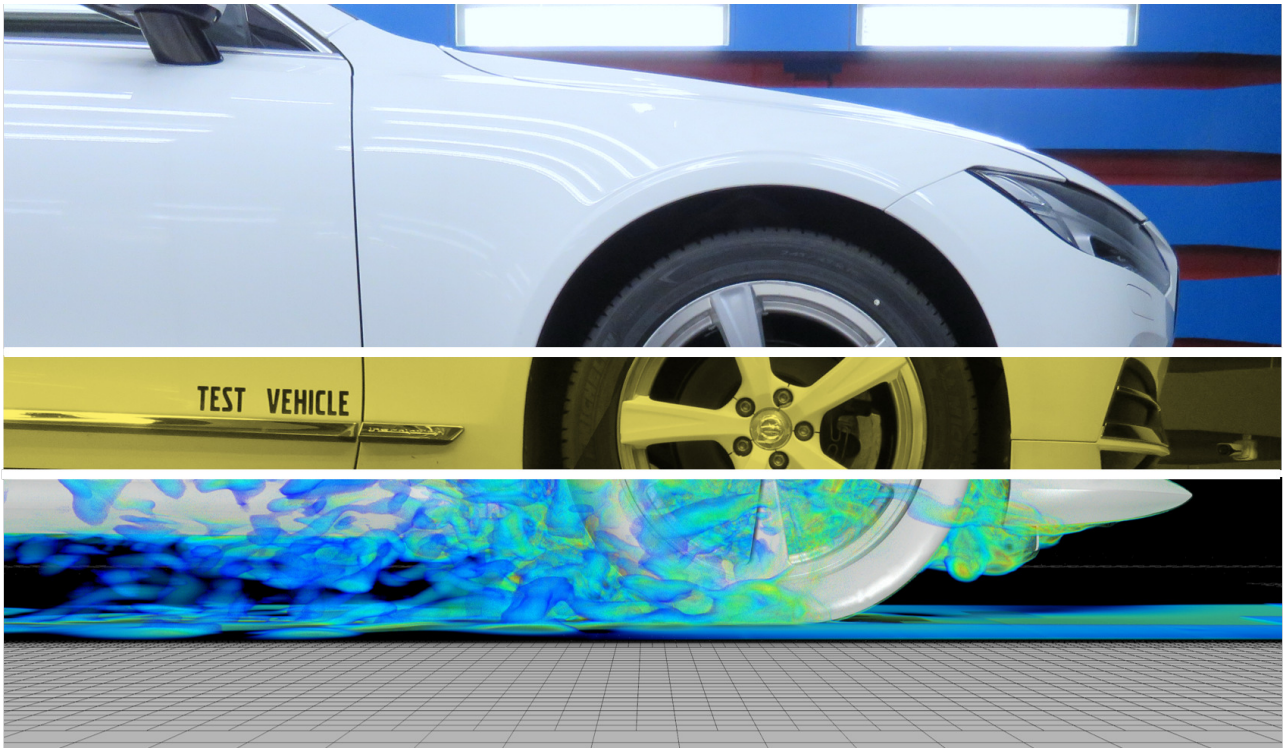

Investigation of Aerodynamic Wheel Design

Master's thesis in Applied Mechanics

HENRIK BERG
ADAM BRANDT

Department of Mechanics and Maritime Sciences
CHALMERS UNIVERSITY OF TECHNOLOGY
Göteborg, Sweden 2018

MASTER'S THESIS IN APPLIED MECHANICS

Investigation of Aerodynamic Wheel Design

HENRIK BERG
ADAM BRANDT

Department of Mechanics and Maritime Sciences
CHALMERS UNIVERSITY OF TECHNOLOGY

Göteborg, Sweden 2018

Investigation of Aerodynamic Wheel Design
HENRIK BERG
ADAM BRANDT

Master's thesis 2018:15
Department of Mechanics and Maritime Sciences
Chalmers University of Technology
SE-412 96 Göteborg
Sweden
Telephone: +46 (0)31-772 1000

Cover:
A three part illustration of a real wheel at the top, a replica of that wheel using a modular wheel concept in the middle and a numerically simulated vorticity field at the bottom.

Chalmers Reproservice
Göteborg, Sweden 2018

Investigation of Aerodynamic Wheel Design
HENRIK BERG
ADAM BRANDT
Department of Mechanics and Maritime Sciences
Chalmers University of Technology

Abstract

The passenger car has become a vital part of modern society, meaning that it accounts for 10 percent of the worldwide energy consumption. With an increasing number of vehicles produced, it is therefore necessary to utilise clean energy sources and to minimise the energy consumption of the vehicles. The aerodynamic drag is the dominating resistive force above 60 km/h and must therefore be reduced to increase the efficiency of the vehicles, especially since the new WLTP and CO_2 emission regulations put stricter demands on the automotive industry. Furthermore, the wheels and wheel housings accounts for up to 25 percent of the aerodynamic drag, making them important components for optimisation.

This thesis investigated the aerodynamic effect of different wheel designs. Both experimental and numerical tools were used to evaluate the importance of 14 wheel parameters. The experiments used a statistical design of experiments (DOE) setup and were performed in the Volvo Aerodynamic Wind Tunnel, where force measurements were taken along with flow field and surface pressure measurements in order to describe the flow around the wheels. The numerical CFD simulations implemented a transient IDDES turbulence model with a sliding mesh setup for the wheel rotation.

It was found that the coverage area was by far the most important design parameter of the wheel. The rim cover and the depth of centre were also found to be significant parameters. The flow field measurements described the important parameters' effects on the flow field at the wheels, where it was found that minimising the near-ground vortex at the front wheel could significantly decrease the aerodynamic drag. The numerical simulations proved to accurately model the flow at the front wheels and aided the understanding of the strong near-ground vortex formation.

In conclusion, it was found that a covered wheel with the cover surfaces flush to the tire wall (bead), was preferred for decreasing the aerodynamic drag and making the vehicle more energy efficient. Furthermore, the open wheels and the wheels with low outer rim coverage had an outflow through the lower part of the wheel, feeding energy to and strengthening the near-ground vortex. Thus, it could be concluded that limiting this outflow is one way of decreasing the aerodynamic drag caused by the wheels.

Keywords: Wheel aerodynamics, Vehicle aerodynamics, Wind tunnel, DOE, CFD, IDDES

Preface

The project presented in this 60 ECTS master's thesis was performed at the department of Mechanics and Maritime Sciences at Chalmers University of Technology, Göteborg. The project was launched in June 2017 and presented in May 2018. The work was mainly carried out at the aerodynamics group of Volvo Car Corporation (VCC) in Torslanda, Sweden.

We would like to acknowledge our examiner, Prof. Simone Sebben, for your support, feedback and valuable discussions during the project. We would also like to express our gratefulness and thank Linda Josefsson (Senior Analysis Engineer at VCC aerodynamics group) for your guidance, valuable inputs and supervision of this project. Also, a big thanks to Dr. Michael Bolzon (Postdoctoral Researcher at VCC and Chalmers) for all the help during the wind tunnel flow field measurements and for your discussions and challenges, which greatly improved the quality of this work.

The project could not have been done without the collaboration and guidance from several departments at VCC. Therefore, we would like to thank; all members at the aerodynamics group, Ole-Kristian Bjerke (Expert Senior Designer at the Exterior Design Dept.), Mikael Fransson (Master Black Belt at Complete Vehicle Engineering), Björn Brännvall and Rickard Camp (Additive Manufacturing Operators at Concept Centre).

In addition, we would also like to express our appreciation to all PhD students at the Road Vehicle Aerodynamics (RVAD) group at Chalmers, who shared their valuable knowledge and helped us throughout the project.

Henrik Berg, Göteborg, 2018 Adam Brandt, Göteborg, 2018

Table of contents

Nomenclature

Abbreviations

CAC	Charge Air Cooler
CFD	Computational Fluid Dynamics
CP	Centre Point
DDES	Delayed Detached Eddy Simulation
DES	Detached Eddy Simulation
DOE	Design Of Experiments
DPI	Detailed Parameter Investigation
EADE	European Aerodynamic Data Exchange
ECTS	European Credit Transfer and Accumulation System
EIA	The U.S. Energy Information Administration
EU	European Union
FFD	Fractional Factorial Design
FVM	Finite Volume Method
IDDES	Improved Delayed Detached Eddy Simulation
LES	Large Eddy Simulation
MW	Moving Wall
NEDC	New European Driving Cycle
OECD	Organisation for Economic Co-operation and Development
RANS	Reynolds Average Navier-Stokes
RDE	Real Drive Emissions
SLS	Selective Laser Sintering
VCC	Volvo Car Corporation
WLTC	Worldwide harmonized Light vehicles Test Cycle
WLTP	Worldwide harmonized Light vehicles Test Procedure

Symbols

α	Road inclination angle	[deg]
ϵ_S	Jet-expansion blockage effect	[-]
ϵ_W	Solid and wake blockage effect	[-]
η	Empirical constant	[-]
$\frac{q}{q_\infty}$	Dynamic pressure correction	[-]
γ	Coefficient accounting for the inertia of the rotating parts	[-]
κ	The von Kármán constant	[-]
μ	Viscosity	[kg/(s·m)]
ω	Vorticity	[1/s]
Φ	Viscous dissipation	[J/(m^{3}s)]
ψ	Coefficient of friction	[-]
ρ	Air density	[kg/m^3]
τ	Wind tunnel shape factor	[-]
τ_w	Wall shear stress	[Pa]
Re	Reynolds number	[-]
ε_{ijk}	Permutation tensor	[-]
A	Vehicle frontal area	[m^2]
B	The empirical logarithmic rule constant	[-]
C	Courant number	[-]
$C_{D,corr}$	Blockage corrected coefficient of drag	[-]
$C_{D,hb}$	Horizontal buoyancy effect	[-]
C_D	Coefficient of drag	[-]
C_{Lf}	Coefficient of front lift	[-]
C_{Lr}	Coefficient of rear lift	[-]
$C_{P,tot}$	Coefficient of total pressure	[-]
C_P	Coefficient of pressure	[-]
c_p	Specific heat capacity	[J/(kg·K)]

F_A	Inertial force	[N]
F_D	Aerodynamic drag force	[N]
F_G	Climbing force	[N]
F_{Lf}	Aerodynamic front lift force	[N]
F_{Lr}	Aerodynamic rear lift force	[N]
F_L	Aerodynamic lift force	[N]
f_p	Porous media resistance	[kg/m^{2}s^2]
F_R	Rolling resistance force	[N]
F_X	Driving force	[N]
g	Gravitational acceleration	[m/s^2]
k	Thermal conductivity	[J/(s·m·K)]
L	Wheel base	[m]
l	Reference length	[m]
L_f	Front axle position	[m]
L_r	Rear axle position	[m]
L_{tot}	Vehicle total length	[m]
M	Pitching moment	[Nm]
m	Mass	[kg]
p	Static pressure	[Pa]
p-value	Statistical probability value	[-]
p_∞	Ambient pressure	[Pa]
P_D	Power requirement for the aerodynamic drag	[W]
P_R	Power requirement for the rolling resistance	[W]
P_X	Driving power	[W]
q	Dynamic pressure	[Pa]
S	Wind tunnel cross section area	[m^2]
T	Temperature	[K]
t	Time	[s]

u_τ	Friction velocity	[m/s]
V	Vehicle volume	[m^3]
v	Velocity	[m/s]
v^+	Non-dimensional near wall velocity	[-]
v_∞	Freestream velocity	[m/s]
v_{mag}	Local velocity magnitude	[m/s]
v_X	Velocity component in X direction	[m/s]
v_Y	Velocity component in Y direction	[m/s]
v_Z	Velocity component in Z direction	[m/s]
y^+	Non-dimensional wall distance	[-]

Chemical symbols

CO	Carbon monoxide
CO_2	Carbon dioxide
HC	Hydrocarbons
NO_X	Nitrogen oxides

Definitions

1 drag count	$\Delta C_D = 0.001$
Base wheel	A thin wheel design used in the modular wheel concept
Donor wheel	A set of regular production wheels
Test object 1	The Volvo S90
Test object 2	The Volvo V90

1 Introduction

This chapter gives an introduction to the topic of this thesis. The background explains why vehicle aerodynamics, and wheel aerodynamics in particular, is important for automotive manufacturers. Furthermore, the purpose and the scope of the project are stated.

1.1 Background

For the last few decades, the passenger car has accounted for 80-85 percent of the inland passenger transport in the European Union [1]. This demonstrates its vital part of modern society. However, this also implies that the passenger car significantly affects the overall worldwide energy consumption. The U.S. Energy Information Administration (EIA) has presented that the transport sector represented 25 percent of the overall energy consumption worldwide in 2012 and has predicted that the quota will remain stable until 2040 [2]. In turn, the passenger car represented 45 percent of the energy consumption within the transport sector in 2012 and is predicted to represent 39 percent in 2040 [2]. In total, this means that the passenger car accounts for approximately 10 percent of the overall worldwide energy consumption. Thus, the net passenger car energy consumption will increase since the overall energy consumption is predicted to increase, especially in the non-OECD countries [2]. This agrees well with the trend of a steadily increasing number of vehicles produced [3], see Fig. 1.1.

To cope with the environmental challenges that this implies, the automotive industry must continue to strive towards more energy efficient vehicles and work together with the rest of the society to develop cleaner energy resources. The electrification of passenger vehicles decreases the direct environmental impact, with a zero-emissions

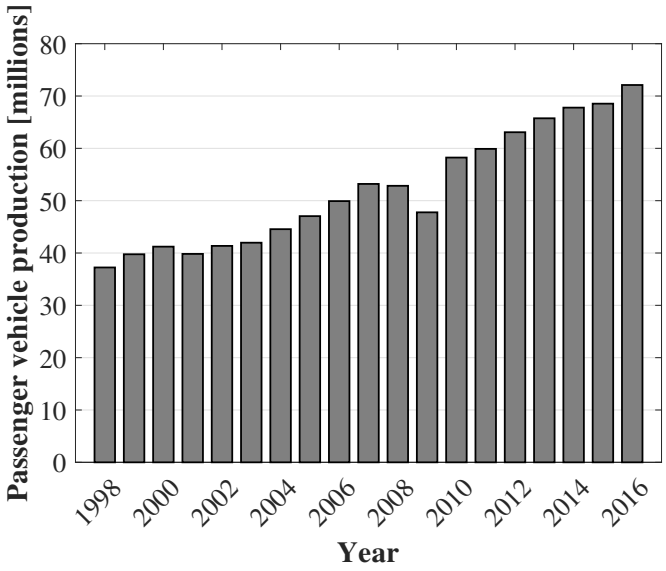

Figure 1.1: Global passenger vehicle production, by year [3].

propulsion system. However, the fuel (electric energy) will indirectly impact the environment if it is not generated by sustainable energy systems. It is therefore vital to ensure that the energy efficiency of the vehicle is high, regardless of the propulsion system. This can be done by minimising the power needed to drive the vehicle, where vehicle aerodynamics has a significant impact.

1.1.1 The importance of vehicle aerodynamics

The power needed to propel the vehicle, P_X, is the product of the vehicle velocity, v, and the driving force, F_X. The driving force can be expressed as in Eq. 1.1 [4], where the terms must balance during any driving condition. The first term on the right-hand side, F_A, is the inertial force due to the acceleration of the vehicle, where m represents the vehicle mass and γ is a constant accounting for the inertia of the rotating parts such as wheels and shafts. The road inclination angle, α, affects both the climbing force, F_G, and the rolling resistance, F_R, where ψ represents the coefficient of friction and g is the gravitational acceleration. Lastly, the aerodynamic drag force, F_D, is affected by the density of air, ρ, the coefficient of drag, C_D, the vehicle frontal area, A, and the vehicle velocity, v.

$$F_x = \underbrace{\gamma m \frac{dv}{dt}}_{F_A} + \underbrace{mg\sin(\alpha)}_{F_G} + \underbrace{\psi mg\cos(\alpha)}_{F_R} + \underbrace{\frac{1}{2}\rho C_D A v^2}_{F_D} \tag{1.1}$$

It is evident that the vehicle mass, m, has great impact on the required driving force, since three out of the four terms in Eq. 1.1 depend on it. Assuming a flat road ($\alpha = 0$) eliminates the climbing force, F_G, and while cruising at constant speed the rolling resistance, F_R, and the aerodynamic drag, F_D, are the only forces affecting the required driving force. At these conditions, the magnitude of the power requirements for these two forces can easily be compared with respect to the vehicle velocity, see Fig. 1.2. The power requirement for the aerodynamic drag, P_D, is

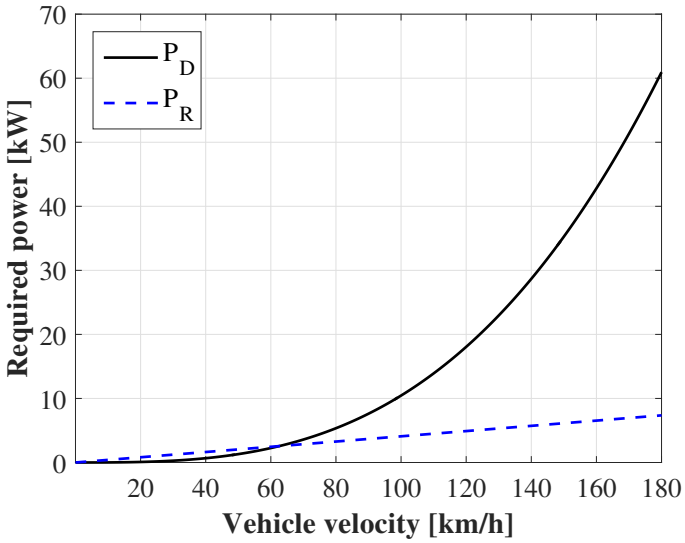

Figure 1.2: Required power for a regular passenger car, in terms of aerodynamic drag, P_D, and rolling resistance, P_R, [based on Eq. 1.1].

dominant above 60 km/h, since it has a cubic dependence on the velocity whereas the rolling resistance, P_R, is linearly dependent. This exemplifies the importance of the aerodynamic drag, especially at higher velocities.

The total aerodynamic drag of the vehicle can further be divided into regions contributing to the drag, such as: exterior body, underbody, engine bay, wheels and wheel housings. It is important to note that the local drag of these regions cannot be summed up to the total drag of the vehicle, due to the complex nature of fluid mechanics [4]. However, when removing the wheels and covering the wheel housings, the drag of the vehicle has been shown to decrease by 25 percent [5, 6]. This indicates that the wheels and wheel housings have a great influence on the vehicle aerodynamics. The development of aerodynamic wheels has therefore become crucial for automotive manufactures, especially when new regulations, drive cycles and test procedures are introduced.

1.1.2 New regulations, drive cycles and test procedures

To understand the environmental and technical advancements in the automotive industry, it is necessary to give a brief background about the regulations and the certification procedures. This background will be taken from a European point of view, but similar regulations apply for other regions as well.

The European Union (EU) has a long history of emission regulations. The first emissions regulation on carbon dioxide (CO), hydrocarbons (HC), nitrogen oxides (NO_X) and particle matter was introduced 1993 as *Euro 1* [7]. Since then, new regulations have been implemented (currently: *Euro 6*) and these harmful emissions from passenger cars have gradually been reduced [8]. However, the *Euro* regulations do not put regulations on the carbon dioxide (CO_2) emissions, which are harmless locally but have a greater global impact as a greenhouse gas [9]. Therefore, in 2012 the European Commission decided to implement mandatory CO_2 targets for the average fleet of every automotive manufacturer. The 2015 target is 130 g CO_2/km and the 2021 target will be 95 g CO_2/km. If a manufacturer fails to reach the fleet target one year, they have to pay an excess emissions premium for every car registered that year [10]. Similar vehicle regulations for emissions are enforced worldwide.

In 2016 (four years after the implementation of the EU CO_2 emissions target regulations), the average fleet emissions were reduced to 118.1 g CO_2/km, which was well below the 2015 target [10]. However, it has become evident that these certified emission values did not represent the real-world fuel consumption. The standardised New European Driving Cycle (NEDC) was found to poorly represent real-world driving conditions. In addition, it has also been found that this difference between certified CO_2 emission values and the real-world emissions has increased over the last years after the introduction of EU fleet targets [11]. This has therefore enforced the implementation of a new test procedure called Worldwide harmonized Light vehicles Test Procedure (WLTP) in the EU, Japan and India. NEDC was a good tool for standardising all fuel consumption test and enabled comparison between automotive manufacturers. Its urban cycle was introduced in 1970 and the highway cycle was added in 1990. To minimise the gap between certified and real-world emission

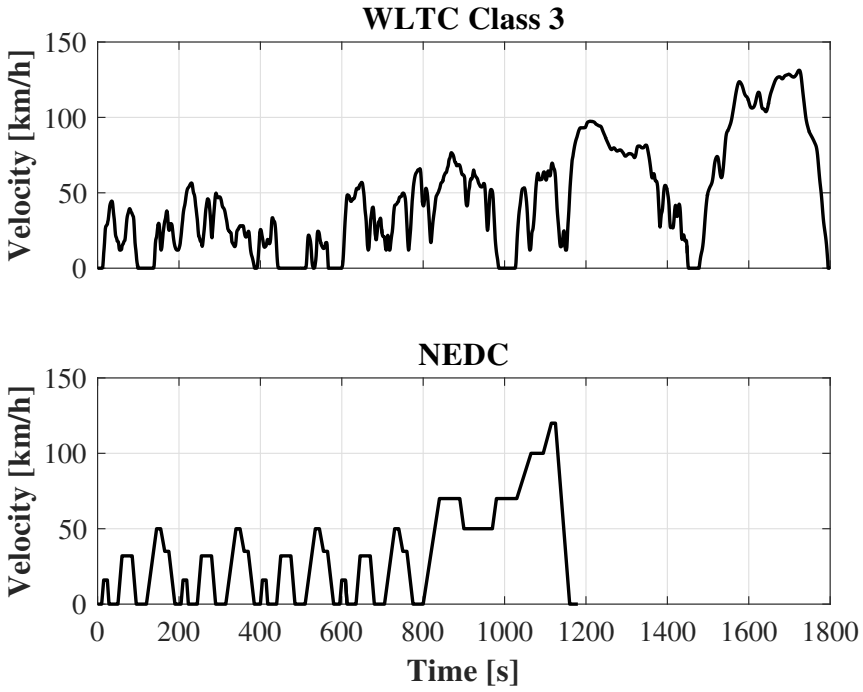

Figure 1.3: Comparison between the new test cycle, WLTC Class 3, and the old, NEDC, in terms of vehicle velocity and duration [14].

values, the new Worldwide harmonized Light vehicles Test Cycle (WLTC) is more irregular and has higher maximum and mean velocities, which is more similar to real-world driving conditions [12], see Fig. 1.3. The higher maximum and mean velocities imply that vehicle aerodynamics becomes even more important, see Fig. 1.2. The WLTP will further be complemented with real drive emissions (RDE) tests, where the measuring equipment is mounted on the tailpipe and the vehicle is driven on regular roads [13]. The aim is to ensure that the gap between certified emission values and real-world emissions stay small for the new WLTP standard.

More strict fleet targets along with new test cycles of higher mean velocity put greater requirements on vehicle aerodynamics, for the manufacturer to stay competitive. In addition, electric and hybrid electric vehicles will suffer from a shorter range if they are not designed with an aerodynamic focus. A profound understanding of wheel aerodynamics will therefore be needed to improve the energy efficiency of the vehicle and to design the aerodynamic wheels of the future.

1.2 Project purpose

The overall purpose of this master's thesis is to investigate the aerodynamic influence of different wheel geometries. The geometry of the wheel can be defined with a set of design parameters. The objective is to investigate how these parameters affect the aerodynamic drag and to find what characterises an aerodynamic wheel design. The aim can be further divided into four specific research questions, where the last should be seen as an extension goal:

- Which wheel parameters are critical, in terms of aerodynamic drag, and which are less important?
- How much do the critical wheel parameters affect the aerodynamic drag and can synergies be found among certain design parameters?
- How does the flow around the wheels change when altering the most important critical wheel parameters?
  - Can numerical simulation methods be used to predict the same trends as the wind tunnel experiments, when altering wheel geometries?

Once these questions have been answered, the goal is to develop design guidelines to be used in an early development phase to predict the aerodynamic performance of the wheel.

1.3 Delimitations and project scope

Physical testing is the primary method of evaluation. The tests are performed in full-scale in the Volvo Aerodynamic Wind Tunnel at VCC. The project is limited to 64 test configurations and the tests are performed on the Volvo S90 model primarily and the Volvo V90 model secondarily. The wind tunnel tests will yield a specific coefficient of drag, C_D, value for each configuration as a response. That response is used in the statistical experimental methods to evaluate the different wheel configurations. Measurements of the flow field will only be performed on a select few of the configurations. The secondary method of evaluation is the numerical method of computational fluid dynamics (CFD). CFD is used to investigate if the numerical method can predict the correct trends, in terms of C_D value, and also to explain certain flow phenomenon around the wheels in comparison with the flow field measurements. The CFD part of the thesis will have a close collaboration with the on-going post-doc project "Aerodynamic simulation of rotating wheels", at Chalmers University of Technology, to avoid unnecessary overlap.

The thesis only considers the 18 inch wheel dimension and one type of tire geometry, to limit the scope. Furthermore, the chosen method will not allow for geometry changes on the backside of the wheel spokes. The wind tunnel tests are performed at 140 km/h, at zero yaw angle. The same limitations are implemented in the CFD simulations.

Since the thesis focuses on the aerodynamics of wheels, other wheel attributes such as; weight, brake cooling and contamination shall be considered but are not factors for optimisation.

1.4 Thesis outline

To aid the reader throughout the report, this section describes the outline of the report where the content of each chapter is briefly described. Some readers might, for example, be interested in the theory (Chapter 2) to learn more about the subject, while others may skip this chapter. The report is divided into the seven chapters described below along with References and Appendices at the end.

Chapter 1 (Introduction) gives a brief background about the subjects and highlights the importance of wheel aerodynamics. The project's purpose and scope are also stated.

Chapter 2 (Theory) will present the theory of fluid dynamics and further describe vehicle and wheel aerodynamics. The theory behind CFD is also described along with some statistics used in the project. This chapter shall give the reader sufficient knowledge to fully comprehend the methodology used and the results found in this thesis.

Chapter 3 (Methodology) describes the experimental and numerical procedures used in the project. Reading this chapter should give sufficient information on how to replicate the study.

Chapter 4 (Results and discussion) presents and analyses the most important findings in the thesis work.

Chapter 5 (Conclusions) summarises and states the most important conclusions made in this project.

Chapter 6 (Recommendations for Future Work) gives recommendations on how this field of science can be further explored by building from this work.

2 Theory

Some theory has already been described in Chapter 1, to explain the background of this thesis. This chapter will handle a wider range of theory with more comprehensive explanations. The first section will cover the basics of fluid dynamics and further explain the theory of vehicle aerodynamics. The second section describes the important aspects of computational fluid dynamics (CFD). Lastly, some statistics theory is presented since this will be used throughout the experimental testing setups.

The Einstein notation rules are used throughout the chapter to enable compact and simple equations [15].

2.1 Fluid dynamics

Fluid dynamics is the study of fluids in motion. A fluid is defined as a substance which continuously deforms under an applied shear stress, meaning that both gases and liquids are fluids [16]. Aerodynamics is a sub field of fluid dynamics studying the effect of air flow (or other gases) around bodies. A few important aspects of basic fluid dynamics are further explained below, along with more specific theory on vehicle aerodynamics.

2.1.1 Basic fluid dynamics

All theory in fluid dynamics is based on the fundamental governing equations. Therefore, it is essential to understand these equations and to know the applied assumptions. Furthermore, to fully understand the work in this thesis, the areas of boundary layer flow and vorticity are also described.

2.1.1.1 Governing equations

The three governing flow equations are the continuity, momentum and energy equations. These equations apply some fundamental laws of physics to the flow. Approximations and assumption of the terms in these laws are often made to simplify the calculations for certain flow cases.

The continuity equation; ensures that the fundamental law of mass conservation is balanced, see Eq. 2.1.

$$\frac{d\rho}{dt} + \rho\frac{\partial v_i}{\partial x_i} = 0 \tag{2.1}$$

If incompressible flow is assumed (constant density), the continuity equation can further be simplified to Eq. 2.2. This assumption is regarded valid for air flows lower than Mach 0.3 (approx. 100 m/s or 360 km/h), and can thus be used in vehicle aerodynamics [4].

$$\frac{\partial v_i}{\partial x_i} = 0 \tag{2.2}$$

The momentum equation; states that the sum of all forces is equal to the momentum of the flow (Newton's 2nd law), see Eq. 2.3. The last term containing the gravity vector, g_i, is often neglected in flows of higher velocities such as vehicle aerodynamics.

$$\rho \frac{dv_i}{dt} = \frac{\partial \sigma_{ij}}{\partial x_j} + \rho g_i \tag{2.3}$$

The term containing the stress tensor, σ_{ij}, can be written as in Eq. 2.4 for a Newtonian viscous fluid, if the incompressible flow condition in the continuity equation is assumed together with constant viscosity, μ. The Newtonian viscous fluid assumption assumes that the viscous stresses are linearly proportional to the local strain rate. This hold true for common fluids such as air and water. Re-writing Eq. 2.3 using Eq. 2.4 develops the momentum equation to Eq. 2.5 (the Navier-Stokes equations), where p is the pressure.

$$\frac{\partial \sigma_{ij}}{\partial x_j} = -\frac{\partial p}{\partial x_i} + \mu \frac{\partial^2 v_i}{\partial x_j \partial x_j} \tag{2.4}$$

$$\rho \frac{dv_i}{dt} = -\frac{\partial p}{\partial x_i} + \mu \frac{\partial^2 v_i}{\partial x_j \partial x_j} + \rho g_i \tag{2.5}$$

The energy equation; is the last of the governing flow equation and it ensures conservation of energy (1st law of thermodynamics), see Eq. 2.6. The left-hand side of the equation corresponds to the internal energy rate where c_p is the heat capacity of the fluid and T the temperature. On the right-hand side, Φ denotes the viscous dissipation and the last term is the conductive heat flux, containing the coefficient of thermal conductivity, k. The energy equation is seldom used in pure vehicle aerodynamic, but it is vital in thermodynamics and supersonic flows.

$$\rho c_p \frac{dT}{dt} = \Phi + \frac{\partial}{\partial x_i}\left(k \frac{\partial T}{\partial x_i}\right) \tag{2.6}$$

2.1.1.2 Boundary layer flow

When an object is exposed to a flow, there will be a relative velocity difference between the freestream and the object's wall. At the wall, a no-slip condition is assumed meaning that the fluid has the same velocity as the wall. The intermediate region where the velocity gradually changes from the wall to the freestream is called a boundary layer. The boundary layer thickness varies depending on the Reynolds number, Re, [16]. The Reynolds number is the ratio between the inertial forces and the viscous friction forces, see Eq. 2.7, with the reference length, l [16].

$$\mathrm{Re} = \frac{\rho v l}{\mu} \tag{2.7}$$

Since the thickness of the boundary layer varies, it is customary to compare the non-dimensional wall distance, y^+, and the near-wall velocity, v^+, when examining the boundary layer, see Eq. 2.8 - 2.10. The friction velocity, u_τ, is based on the wall shear stress, τ_w, and is used to make the quantities non-dimensional.

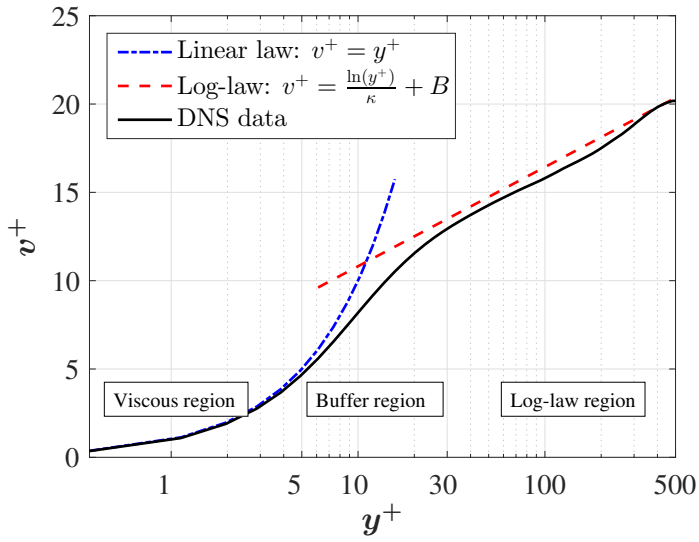

Figure 2.1: Velocity profile near the wall for a turbulent boundary layer. The Direct Numerical Simulation (DNS) data [18] compared with the linear law (Eq. 2.11) and the log-law (Eq. 2.12).

$$y^+ = \frac{u_\tau y}{\nu} \tag{2.8}$$

$$v^+ = \frac{v}{u_\tau} \tag{2.9}$$

$$u_\tau = \sqrt{\frac{\tau_w}{\rho}} \tag{2.10}$$

When comparing the non-dimensional quantities, it is evident that the boundary layer itself has multiple regions, see Fig. 2.1. At low y^+ values (near the wall) the viscous diffusion dominates, and a linear law can be used to approximate the v^+ value, see Eq. 2.11. At higher y^+ values (>30) the boundary layer is dominated by turbulent diffusion and a logarithmic rule can be applied, see Eq. 2.12, where κ and B are constants. The intermediate buffer region ($5 < y^+ < 30$) cannot be predicted with the same accuracy by any of the rules, see Fig. 2.1 [17].

$$v^+ = y^+ \tag{2.11}$$

$$v^+ = \frac{\ln(y^+)}{\kappa} + B \tag{2.12}$$

2.1.1.3 Vorticity

An important aspect of fluid dynamics is the understanding of vortices, i.e. circulating flow structures generated by a wing tip, for example. It must be noted that vorticity and a vortex are not interchangeable expressions. A vortex generally refers to a rotating flow structure while vorticity is a measurement of the flow's tendency to

rotate the fluid particle. There can be vorticity without a vortex forming and a vortex can have no vorticity, even though a vortex generally has vorticity [17]. Energy is taken from the mean flow to form these vortex structures, which locally increase the aerodynamic drag (vortex drag). To calculate the vorticity in a direction, the two perpendicular velocity components are used, see Eq. 2.13.

$$\omega_i = \varepsilon_{ijk} \frac{\partial v_k}{\partial x_j} \tag{2.13}$$

Hence, the vorticity in the X-direction can be expressed as Eq. 2.14.

$$\omega_X = \frac{\partial v_Y}{\partial z} - \frac{\partial v_Z}{\partial y} \tag{2.14}$$

2.1.2 Vehicle aerodynamics

As mentioned in Section 1.1.1, the aerodynamic drag is the dominant force acting on the vehicle at higher velocities, see Fig. 1.2. This drag force can be divided into friction drag, acting tangentially to the surface, and pressure drag, acting normal to the surface of the vehicle. On a bluff body, as a passenger car, the pressure drag generally accounts for more than 90 percent of the total drag. A wind tunnel is generally used when evaluating vehicle aerodynamics.

2.1.2.1 Wind tunnel testing

To analyse the aerodynamic performance of a vehicle, a controlled environment with accurate measurement equipment is preferred.

By measuring the aerodynamic drag force, F_D, it is possible to calculate the coefficient of drag, C_D, by re-arranging the last term in Eq. 1.1 into Eq. 2.15.

$$C_D = \frac{2F_D}{\rho A v^2} \tag{2.15}$$

In a similar way, the coefficient of front lift, C_{Lf}, can be calculated by knowing the front lift force, F_{Lf}, given by the total lift force, F_L, the wheel base, L, the front axle positioning, L_f, and the pitching moment, M, see Eq. 2.16. Similarly, the coefficient of rear lift, C_{Lr}, can be calculated according to Eq. 2.17 by using the rear axle positioning, L_r.

$$\begin{aligned} C_{Lf} &= \frac{2F_{Lf}}{\rho A v^2} \\ F_{Lf} &= \frac{1}{L}\left(F_L L_r + M\right) \end{aligned} \tag{2.16}$$

$$\begin{aligned} C_{Lr} &= \frac{2F_{Lr}}{\rho A v^2} \\ F_{Lr} &= \frac{1}{L}\left(F_L L_f - M\right) \end{aligned} \tag{2.17}$$

However, all the force measurements in the wind tunnel will yield an incorrect result if not corrected. This effect occurs since the vehicle blocks a relatively large section of the wind tunnel, forcing the flow to accelerate around the vehicle. This solid blocking along with the wake blockage need to be corrected. Eq. 2.18 shows the correction method used in the Volvo Aerodynamic Wind Tunnel [19].

$$C_{D,corr} = \frac{C_D - C_{D,hb}}{\frac{q}{q_\infty}} \tag{2.18}$$

The dynamic pressure correction, $\frac{q}{q_\infty}$, can further be described as a jet-expansion effect, ϵ_S, and a solid and wake blockage effect, ϵ_W, see Eq. 2.19. This is the preferred dynamic pressure correction for a slotted wind tunnel section [20].

$$\begin{aligned} \frac{q}{q_\infty} &= (1 + \epsilon_S + \epsilon_W)^2 \\ \epsilon_S &= \tau\sqrt{\frac{V}{L_{tot}}}\sqrt{\left(\frac{A}{S}\right)^3} \\ \epsilon_W &= \frac{A}{S} \cdot \left(\frac{C_D}{4} + \eta\right) \end{aligned} \tag{2.19}$$

The vehicle size is in terms of volume, V, frontal area, A, and total length, L_{tot}, is needed for this correction along with the wind tunnel cross section, S, the tunnel shape factor, τ, and the empirical constant, η. The other unknown in Eq. 2.18 is the effect of horizontal buoyancy, $C_{D,hb}$. This entity can be divided into the horizontal buoyancy of the empty tunnel (which can be measured) and the horizontal buoyancy caused by the vehicle (defined by a large set of empirical data, provided by the European Aerodynamic Data Exchange (EADE) test in 2010 [21]).

A useful parameter for flow analysis in the wind tunnel is the non-dimensional coefficient of pressure, C_P. The difference between the local static pressure, p, and the ambient pressure, p_∞, is normalised with the dynamic pressure, $q = \frac{1}{2}\rho v^2$, see Eq. 2.20. Hence, the C_p value is a useful non-dimensional variable to visualise regions of high and low pressure. The pressure on a surface can be directly linked to the local force, thus the C_P value can visualise local drag and lift forces.

$$C_P = \frac{p - p_\infty}{\frac{1}{2}\rho v^2} \tag{2.20}$$

A similar coefficient commonly used is the coefficient of total pressure, $C_{P,tot}$, see Eq. 2.21. Apart from the C_P value, the $C_{P,tot}$ value incorporates the local velocity magnitude, v_{mag}, of the flow and is thus better at visualising regions of high energy losses. The total pressure coefficient is often preferred when measuring the flow field, while the pressure coefficient is used on the vehicle surface.

$$C_{P,tot} = \frac{\frac{1}{2}\rho v_{\text{mag}}^2 + p - p_\infty}{\frac{1}{2}\rho v^2} \tag{2.21}$$

To further study the local cause of increased drag, a quantity named *local drag* can be calculated. The formula uses the total pressure coefficient, $C_{P,tot}$, along with

the three spatial velocity components, v_X - v_Y - v_Z, which are compared to the freestream velocity, v_∞, see Eq. 2.22 [22]. This quantity accounts for the loss of energy due to total pressure loss as well as redirected and accelerated flow.

$$C_D A = \int_A (1 - C_{P,tot})\, dA - \int_A \left(1 - \frac{v_X}{v_\infty}\right)^2 dA + \int_A \left(\frac{v_Y}{v_\infty}\right)^2 dA + \int_A \left(\frac{v_Z}{v_\infty}\right)^2 dA \quad (2.22)$$

2.1.2.2 Wheel aerodynamics

As mentioned earlier, removing the wheels and covering the wheel housings have been shown to decrease the drag by 25 percent [5, 6]. Hence, it is important to have an understanding of wheel aerodynamics and the flow structures generated by the wheels.

By beginning to observe an isolated simple wheel in the air stream it is evident that this geometrical shape is not streamlined and will generate vortices, see Fig. 2.2. However, placing the isolated wheel on the ground will vastly change the flow around the wheel. The flow near the ground is forced outwards on each side of the wheel. This phenomenon is called the *jetting* effect. The jetting effect becomes weaker when the wheel rotates, giving more energy to the flow in that region [24], see Fig. 2.3. The jetting vortex (1) is present for both the stationary and the rotating isolated wheel, but the stationary wheel has an extra weak near ground horse shoe vortex (4) as well. The dominating vortex structure of the isolated wheel is the horse shoe vortex behind the wheels (2), which highly influences the global flow around the wheel [24]. This vortex becomes less powerful when rotating the wheel. The stationary wheel has a C-shoulder vortex pair (3), which keeps the flow attached over the wheel and is inducing more vorticity to the horse shoe vortex (2), see Fig. 2.3a. Hence, the flow accelerates over the wheel causing more lift [24]. When rotating the wheel, a ring vortex (3) forms instead of the C-shoulder vortex pair, due to flow separation, see Fig. 2.3b. This will reduce the lift and drag of the rotating wheel [24].

The flow structure becomes even more complex when the wheel is enclosed in the wheel house, see Fig. 2.4. The lower part of the wheel has similar vortex structures to the isolated wheel, with a jetting vortex (1) and a horse shoe vortex (2). However, the horse shoe vortex is much weaker for the enclosed wheel [24]. When the

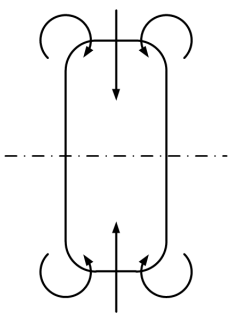

Figure 2.2: Vortices generated by a stationary wheel off the ground, viewed from behind [23].

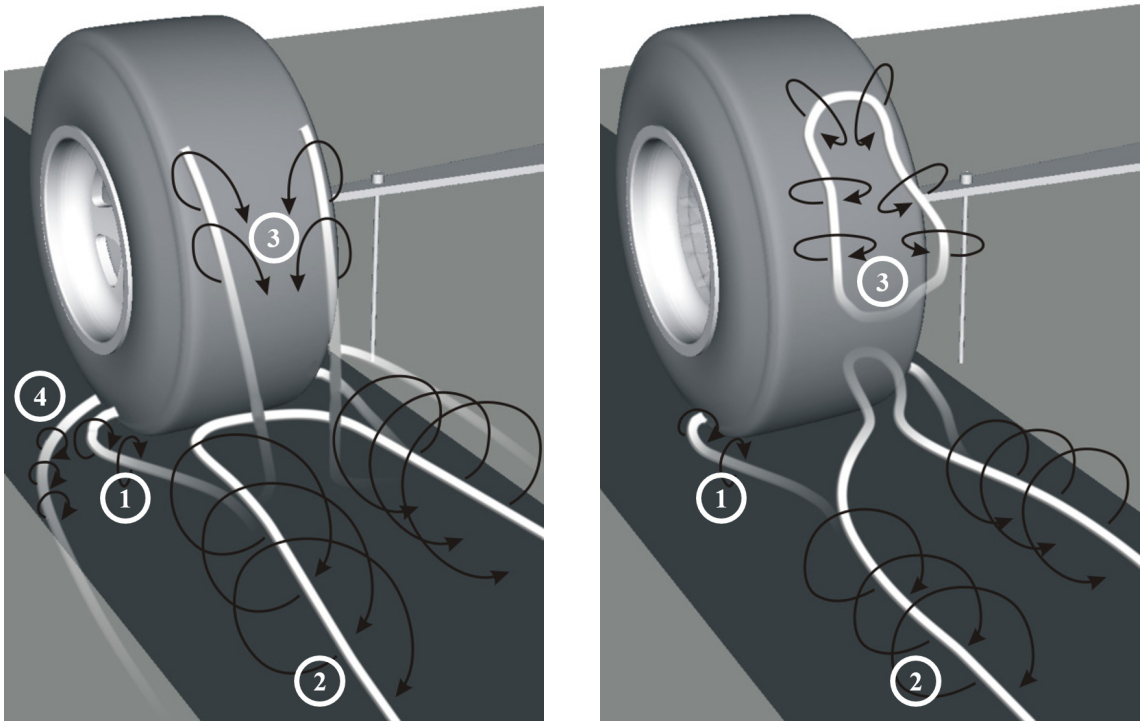

(a) Stationary wheel. **(b)** Rotating wheel.

Figure 2.3: Vortex structure behind a single isolated wheel [24].

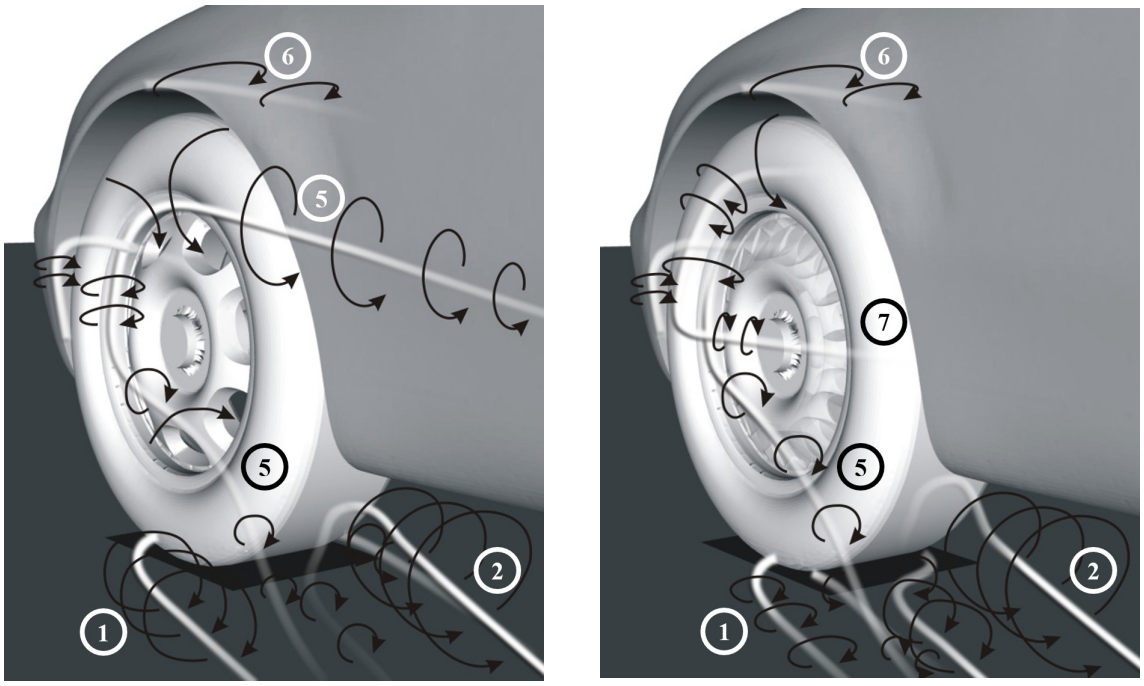

(a) Stationary wheel. **(b)** Rotating wheel.

Figure 2.4: Vortex structure behind the front wheel in the wheel house [24].

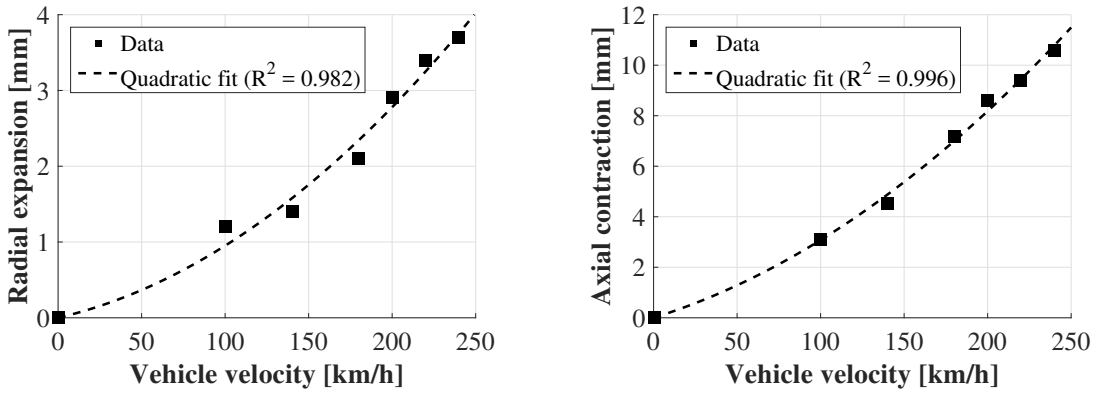

(a) Radial expansion. **(b)** Axial contraction.

Figure 2.5: Tire deformation due to rotation of the wheel [25].

flow passes over the rim flange, another horse shoe vortex (5) can be seen for the stationary wheel, see Fig. 2.4a. The upper part of this horse shoe vortex disappears when rotating the wheel, see Fig. 2.4b. A weak trailing vortex (6) from the wheel house arch can often be seen. Lastly, an extra side vortex (7) is generated by the wheel rotation [24].

Furthermore, when the wheel is rotated its outer geometry changes. It has been shown that the tire expands radially with increasing rotational velocity, due to the centrifugal force [25]. Similarly, an axial contraction of the tire can be seen, see Fig. 2.5. It is evident that for both the radial expansion and for the axial contraction there is a quadratic relation with increasing velocity. The change in tire geometry will change the wheel centre height and thus the trim height of the vehicle. Therefore, it is important to set the correct trim height during wind tunnel experiments and to use accurate tire geometries when using numerical simulations. The axle load will also deform the tire near the contact patch, causing a bulge on the sides of the tire, see Fig. 2.6. To achieve accurate numerical simulations, this bulge also needs to be included accurately in the tire geometries.

Figure 2.6: Tire bulge at the contact patch.

2.2 Computational fluid dynamics

Computational fluid dynamics (CFD) is a numerical method using finite volume cells to analyse fluid flows. The method is generally based on the fundamental Navier-Stokes equations and is commonly used in vehicle aerodynamics to simulate flow and analyse the forces acting on the vehicle.

The CFD theory will focus on the modelling of wheel rotation, since that is vital for the thesis. Before that, the theory of the applied turbulence modelling method will be explained.

2.2.1 Turbulence modelling

The flow around passenger vehicles is highly turbulent. The non-linear Navier-Stokes equations cannot be solved for every time instance and need to be re-written and partly modelled. The Reynolds average Navier-Stokes (RANS) turbulence model will be presented along with the large eddy simulation (LES) approach, where the two combined form the improved delayed detached eddy simulation (IDDES). Finally, the theory of the Courant number will be presented to explain time stepping in transient simulations.

2.2.1.1 Reynolds average Navier-Stokes

Turbulent flow can be decomposed into a mean ($\bar{\cdot}$) and a fluctuating ($'$) value of the velocity and pressure components ($v_i = \bar{v}_i + v_i'$, $p = \bar{p} + p'$). The continuity and Navier-Stokes equations (Eq. 2.1 and 2.5) can be re-written, using this decomposition, to the Reynolds average Navier-Stokes (RANS) equations, see Eq. 2.23.

$$\begin{aligned} \frac{\partial \bar{v}_i}{\partial x_i} &= 0 \\ \frac{\partial \bar{v}_i \bar{v}_j}{\partial x_j} &= -\frac{1}{\rho}\frac{\partial \bar{p}}{\partial x_i} + \frac{\partial}{\partial x_j}\left(\nu \frac{\partial \bar{v}_i}{\partial x_j} - \overline{v_i' v_j'}\right) \end{aligned} \tag{2.23}$$

The Reynolds stress tensor, $\overline{v_i' v_j'}$, adds six more unknowns to the four equations meaning that this quantity must be modelled. The shear stress transport (SST) k-ω turbulence model [26] is one way of modelling this term.

2.2.1.2 Large eddy simulation

Instead of decomposing the components into a mean and fluctuation part, the large eddy simulation (LES) approach filters (volume averages) them based on the grid scale (mesh). The larger flow structures (eddies) can then be resolved, while the subgrid stresses are modelled. These stresses are smaller than the Reynolds stresses, making LES more accurate than RANS [17]. However, LES requires an extremely fine mesh in the boundary layer making it unsuitable for vehicle aerodynamics.

2.2.1.3 Improved delayed detached eddy simulation

A more usable turbulence model for vehicle aerodynamics is the detached eddy simulation (DES) model, which uses RANS in the boundary layer and LES outside making the simulation accurate while keeping the cell count low. The cutoff criteria between RANS and LES was improved twice resulting in the IDDES model [27].

2.2.1.4 Courant number

The Courant number, C, is a measurement of the number of cells a fluid particle travels through each time step, Δt. The 1-dimensional case can be seen in Eq. 2.24 where Δx is the cell size and v the fluid velocity. The Courant number can be used to set a desired time step in transient simulations.

$$C = \frac{v\Delta t}{\Delta x} \tag{2.24}$$

2.2.2 Modelling motion

To model motion several methods are being used, all with different strengths and weaknesses. In this project there are three methods used: the moving wall boundary condition, the actual displacement of the mesh vertices (sliding mesh) and finally a method developed for steady state simulations using multiple reference frames (MRF) to simulate motion. The motions simulated in this project were the rotation of the wheels and the fan. Hence, this theory section will only cover rotational motion.

2.2.2.1 Moving wall

The wall boundary condition normally applies a no-slip condition, with zero velocity at the wall. The moving wall (MW) boundary condition applies a tangential velocity to the nodes at the wall. The limitation of this modelling method is that any motion occurring normal to the wall surface cannot be captured, since the boundary condition only can apply tangential velocity components at the surface [28].

2.2.2.2 Sliding mesh

In order to create an actual displacement of the mesh vertices, the simulation software rotates a smaller sub-domain containing the mesh and the rotating geometry. This implies that the simulation must be transient. For wheel aerodynamics, a rotational sliding mesh domain at the wheels can be used to model their rotation. However, this method implies that the rotational domain must have rotational symmetry. The tires are not symmetric, as described in Section 2.1.2.2, and can thus not be included in the rotational domain with the software currently available. The sliding mesh method, used on the wheels excluding the tires, has nevertheless been proven to give the best results while still being an affordable method to model the rotating motion of the wheels [28]. However, this transient method requires more simulation time compared to other methods.

2.2.2.3 Multiple reference frame

While the sliding mesh method moves the mesh and requires a transient simulation, the multiple reference frame (MRF) can model motion with a steady state simulation. The MRF method can still be used in transient simulation. The method uses a rotating coordinate system on these domains. The velocities can hence be transformed from the stationary (inertial) frame of reference into the rotational frame, mimicking a rotation. This method has proven to be an improvement compared to the moving wall boundary for steady state simulation, but it is not as good at modelling motion as the transient sliding mesh method [28].

2.3 Statistics

Statistics can be used to set up experimental test plans, in order to efficiently evaluate a large number of parameters with a few number of tests. This can be referred to as design of experiments (DOE). In this theory section, the basic statistics of DOE matrices will be presented along with methods used to decrease the number of tests. The statistical methods evaluate the parameters' effects based on a response (in this thesis the C_D value). The methods define each parameter at two levels, a geometrical minimum and a maximum. Both the individual first order (main) effects of the parameters and their combined (synergy) effects of higher orders can be found using these statistical methods.

2.3.1 Two level full factorial design

A DOE matrix constructed by a full factorial design will investigate all main and synergy effects of the included parameters. A full factorial design of three parameters can be represented by a 3-dimensional cube, where each corner represents the yield of a test configuration, see Fig. 2.7. Each dimension of the cube represent the change of one parameter, for e.g. y_4 has coordinates (+,−,+) meaning that parameter A is set to maximum, parameter B is set to minimum and parameter C is set to its maximum geometrical value. This implies that all included parameters must be able to geometrically exist together at both levels. A full factorial design requires 2^P number of test configurations, where P is the number of parameters included.

The configuration responses y_1 to y_8 are then used to evaluate the parameter effects, see Eq. 2.25 and 2.26 for examples of the main effect of A and the second-order synergy effect between B and C.

$$\Delta A = \frac{y_2 + y_4 + y_6 + y_8}{4} - \frac{y_1 + y_3 + y_5 + y_7}{4} \tag{2.25}$$

$$\Delta BC = \frac{y_1 + y_2 + y_7 + y_8}{4} - \frac{y_3 + y_4 + y_5 + y_6}{4} \tag{2.26}$$

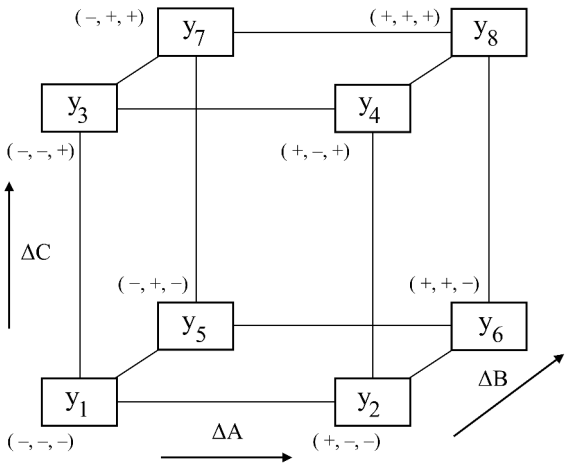

Figure 2.7: A 3-dimensional cube visualising all test configurations with their corresponding response, y_n, for a full factorial design of three parameters.

2.3.2 Fractional factorial design

Since the number of required test runs of a full factorial design doubles for each added parameter, the method becomes unsuitable for investigations including many parameters. The fractional factorial design (FFD) reduces the number of tests required.

The number of tests is reduced by combining the lower order effects with the higher order effects and then assuming the higher order effects to be negligible. For example, the measured effect $I = A + BC$ combines the main effect of A and the synergism between B and C. By adding Eq. 2.25 and 2.26, Eq. 2.27 shows the test configurations needed to get the combined effect. This is visualised in Fig. 2.8.

$$\Delta A + \Delta BC = \frac{y_2 + y_8}{2} - \frac{y_3 + y_5}{2} \tag{2.27}$$

Hence this is halving the number of tests required. However, this implies that the second-order synergy BC can be neglected to get the main effect of A. Second-order effects are often significant in physics and this assumption is therefore not valid. The effect $I = A + BC$ have resolution III which is thus not recommended. However, by including more than three parameters, higher resolutions can be received using the same mathematics, see Table 2.1. The resolution of V gives $I = A + BCDE$, which makes the assumption that the fourth-order synergism between B, C, D and E can be neglected. This assumption is valid in the physics field of fluid dynamics.

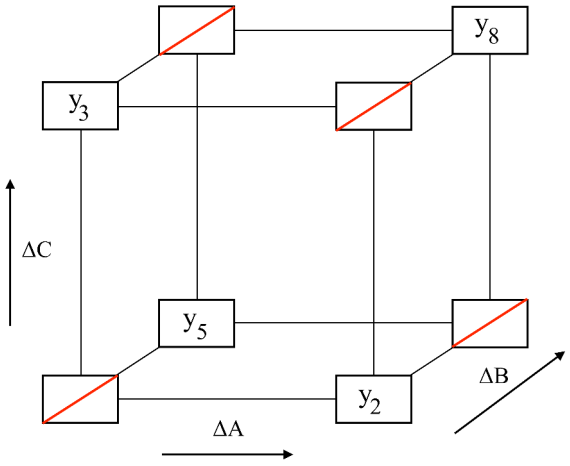

Figure 2.8: A 3-dimensional cube visualising the reduced test configurations with their corresponding response, y_n, for a fractional factorial design of three parameters.

Table 2.1: The number of test configurations (runs) needed depending on the number of parameters (factors). The *Full* boxes represent a full factorial design, where the roman numbers represent the resolutions of the fractional factorial designs. Green boxes are recommended for usage, where yellow can be used if synergies are known to be small and red is not recommended [29].

	Factors													
Run	2	3	4	5	6	7	8	9	10	11	12	13	14	15
4	Full	III												
8		Full	IV	III	III	III								
16			Full	V	IV	IV	IV	III	III	III	III	III	III	III
32				Full	VI	IV	IV	IV	IV	IV	IV	IV	IV	IV
64					Full	VII	V	IV	IV	IV	IV	IV	IV	IV
128						Full	VIII	VI	V	V	IV	IV	IV	IV

2.3.3 Plackett-Burman design

To further reduce the number of tests required, the Plackett-Burman design can be used. The design is based on a matrix structure using a multiple of 4 but not a power of 2 as the number of test (i.e. 12, 20, 24, 28, 36...). Each test matrix has the capacity to screen the same number of parameters (or fewer) as the number of tests minus one.

This reduction can be done by neglecting all synergy effects. Any synergy effect would therefore increase or decrease the effect of the corresponding main effects. Hence, the method can be used in a screening process where the main goal often is to rate the most important parameters and to neglect the insignificant ones. A Pareto chart is often used for this evaluation, see Fig. 2.9. The X axis shows the standardized effect, which is a measure of the offset in standard deviations from the

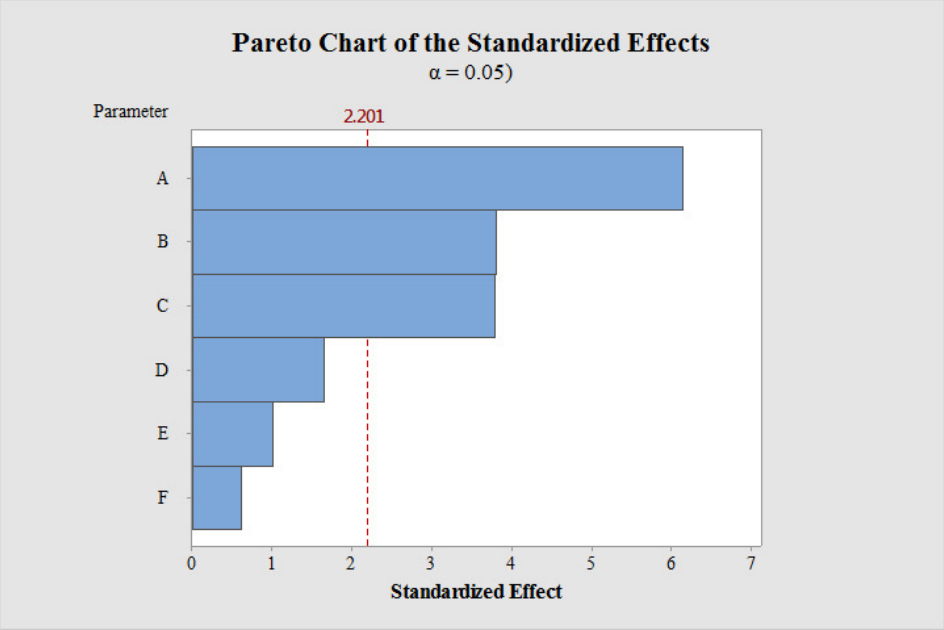

Figure 2.9: Example of a Pareto chart of the results for a Plackett-Burman screening evaluation.

normal distribution around zero. Hence, a standardized effect close to zero can be seen as insignificant whereas a high value is extremely unlikely to be insignificant. The red dashed vertical line represents the number of standard deviations for a corresponding p-value of 0.05, often regarded as the significance limit.

2.3.4 Centre points

When analysing the results from any two level DOE test matrix, the parameters' effects are assumed to be linear between their minimum and maximum levels. This is the case for all designs described above. By using a centre point, it is possible to analyse if this assumption of linearity is correct. The centre point is placed between the maximum (+) and minimum (−) level of all parameters, a position of coordinates 0. The centre point for the cubes in Fig. 2.7 and 2.8 would be placed at coordinate $(0, 0, 0)$. Hence, the centre point represents the middle value of all parameters. Fig. 2.10 visualises a centre point of two parameters where the centre point confirms the linearity. In Fig. 2.11, the centre point proves non-linearity of both parameter A and B, whereas Fig. 2.12 visualises a result where the centre point proves non-linearity of parameter B and confirms the linearity of parameter A.

If any of the parameters included in the test matrix is defined as an integer instead of a continuous parameter, a geometrical centre point may not exist (for example 5 and 10 number of spokes would yield a centre point at 7.5 spokes). In this case, two centre points have to be used, one with 5 spokes and the other with 10 spokes.

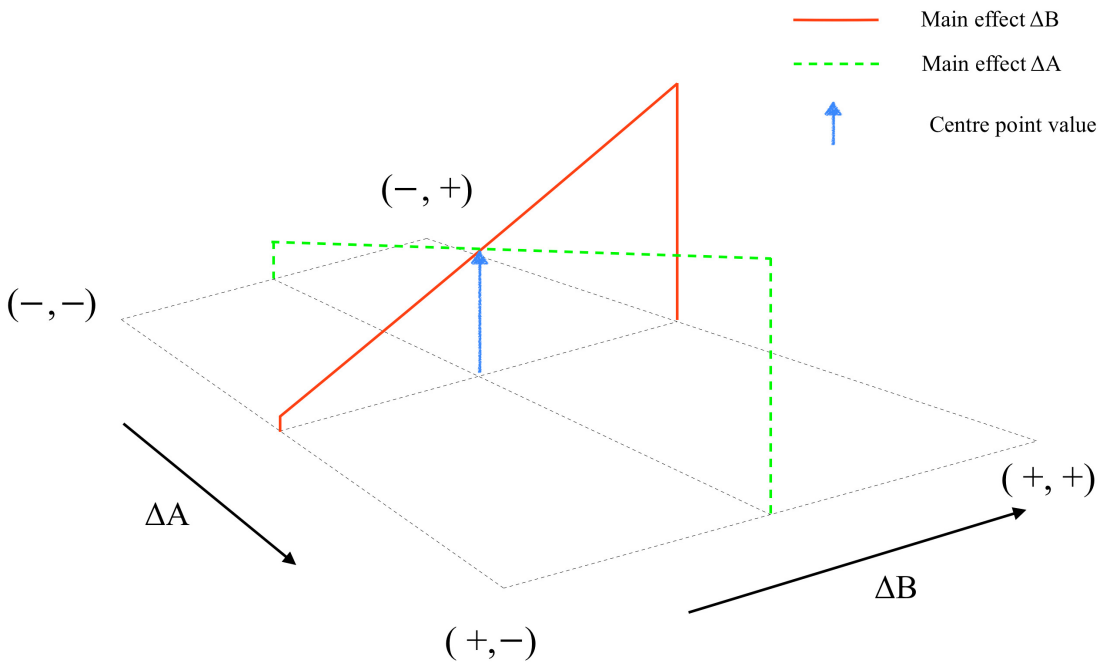

Figure 2.10: The centre point confirms linearity for the main effects ΔA and ΔB.

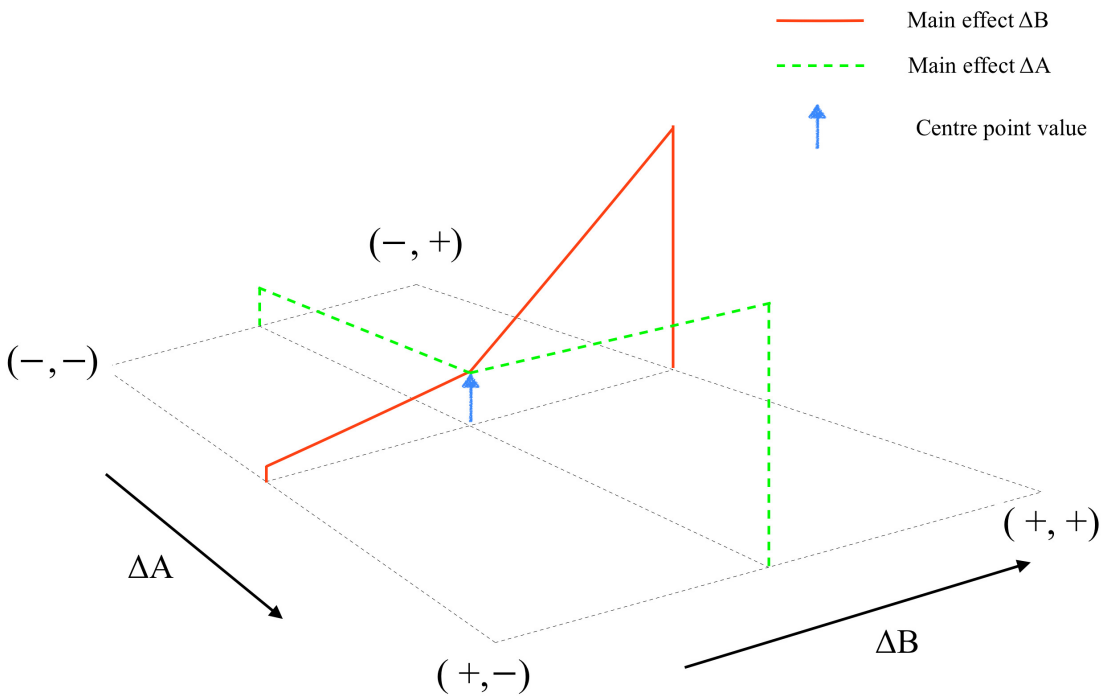

Figure 2.11: The centre point proves non-linearity for the main effects ΔA and ΔB.

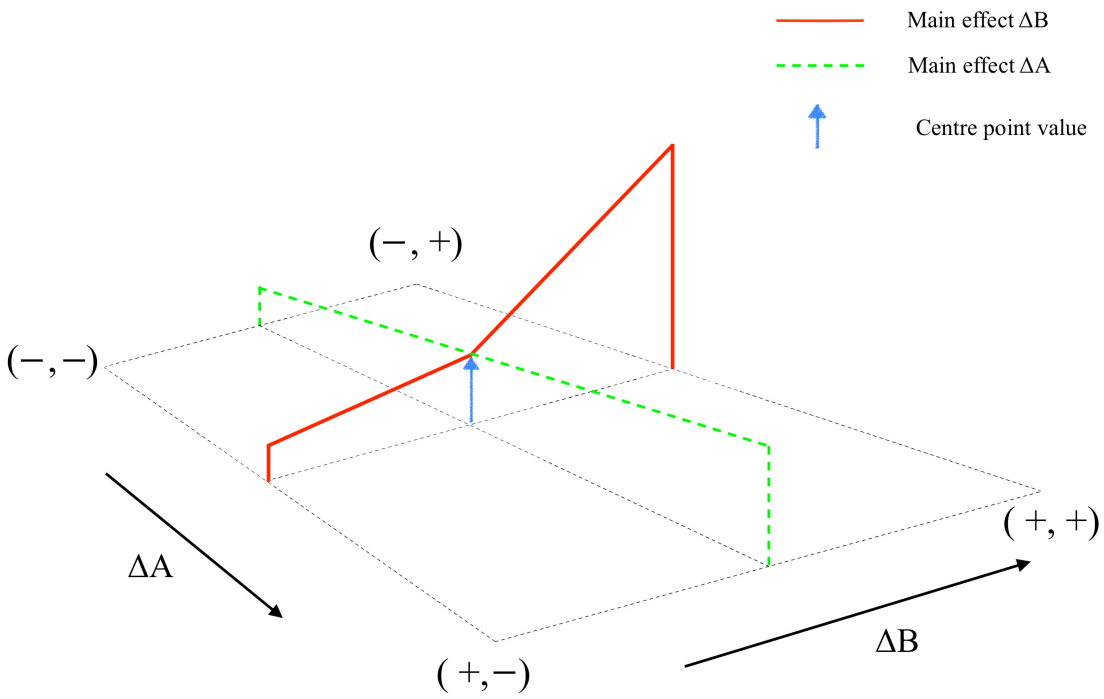

Figure 2.12: The centre point confirms linearity of the main effect ΔA and proves the non-linearity of ΔB.

3 Methodology

Both experimental and numerical investigations were performed in this thesis work. This chapter describes the methodologies used during these investigations along with information about the investigated wheel geometries and the evaluation method.

3.1 Experimental procedure

All experimental work was performed in the Volvo Aerodynamic Wind Tunnel at VCC. The wind tunnel is of the closed return type, with a cross section of 27 m^2 at the nozzle end, equipped with a 5 MW fan and a slotted wall test section. The test section is further equipped with a 5-belt moving ground system and a boundary layer control system consisting of a basic suction scoop, two distributed suction zones and tangential blowers behind the wheels and behind the centre belt, see Fig. 3.1. The moving ground system consists of one centre belt under the vehicle and four wheel drive unit belts which make the wheels rotate. A more detailed description and performance review of the wind tunnel's moving ground and boundary layer control systems can be found in the work by Sternéus et. al [30]. Both of these systems

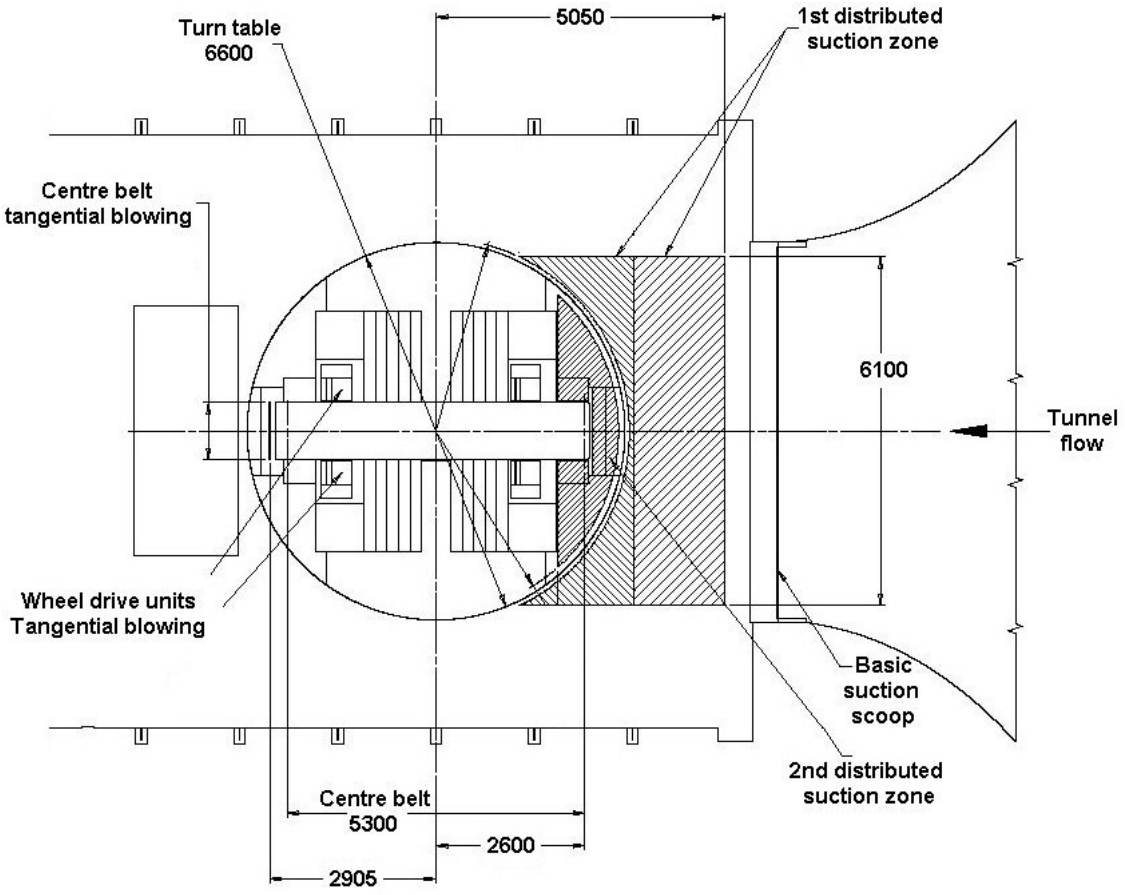

Figure 3.1: Layout of the test section in the Volvo Aerodynamic Wind Tunnel [30].

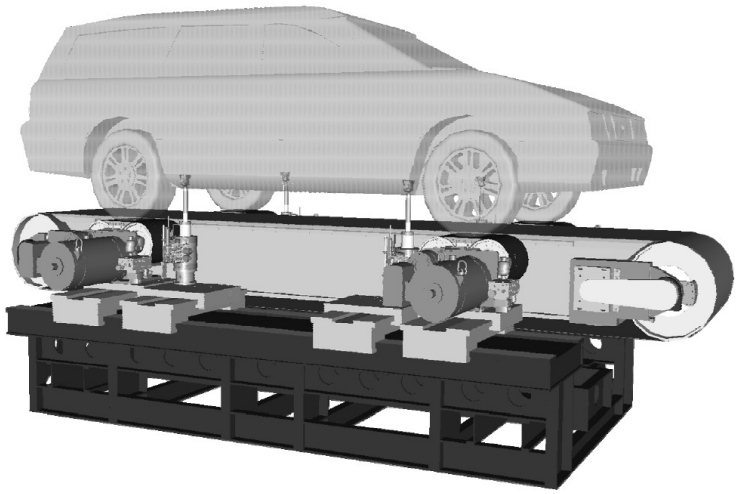

Figure 3.2: Illustration of the vehicle installation in the wind tunnel, with the struts and the 5-belt system connected to the under floor balance (courtesy of VCC).

are used to create more realistic road conditions in the wind tunnel. For wheel and underbody analysis, it has been found that it is vital to use a moving ground system (with rotating wheels) and sufficient minimisation of the floor boundary layer [31]. The vehicle is held in place by four struts. Two behind the front wheels and two in front of the rear wheels. The struts and the whole platform, including the wheel drive units, are connected to the under floor balance, see Fig. 3.2. The balance is used to measure the forces and moments acting on the vehicle.

The wind tunnel coordinate system defines the X axis as the vehicle driving direction, whereas the Y and Z are the horizontal and vertical axes, respectively.

3.1.1 Force measurements

Forces and moments in all directions can be measured by the balance, by knowing the position of the struts and wheel drive units together with the forces acting on them. The wheel drive units rotate the wheels and must thus overcome the rolling resistance, F_R. This becomes an internal force for the wheel drive units and is therefore eliminated from the force measurements performed by the balance. This arrangement ensures that the balance will only measure the aerodynamic forces. However, this will also neglect the ventilation resistance of the rotating wheels, which is an aerodynamic force affected by the wheel and tire design [25]. This wind tunnel setup was therefore limiting the thesis to not include measurements of this quantity in the experimental investigation.

The forces and moments measured by the balance can then be used to calculate the coefficient of drag, C_D, the coefficient of front lift, C_{Lf}, and the coefficient of rear lift, C_{Lr}, by using Eq. 2.15 - 2.17. Furthermore, the effect of the vehicle blocking a part of the test section must be taken into account. The Volvo Aerodynamic Wind Tunnel uses a blockage correction method adopted for a slotted wall test section [19], see Section 2.1.2.1 for in depth explanation of the applied method.

Table 3.1: Measurement uncertainties, in terms of drag and lift coefficients, for a standard test case at 140 km/h in the Volvo Aerodynamic Wind Tunnel.

Test case	ΔC_D	ΔC_{Lf}	ΔC_{Lr}
Difference within the same test session	0.001	0.001	0.005
Difference for the same vehicle, but different test session	0.003	0.004	0.008

The wind tunnel is, as described above, a complex measurement system. It has been found that the same test object can yield slightly different results, due to the uncertainties of the wind tunnel. Table 3.1 shows these uncertainties for the drag and lift coefficients for a standard test case at 140 km/h. It is evident that it is preferred to make comparisons within the same test session. The force measurements for this thesis was performed at 140 km/h at zero yaw angle.

3.1.2 Pressure and flow field measurements

In order to further explain the results from the force measurements, it was decided to expand the study to include surface pressure and flow field analyses. The pressure in the front wheel house was analysed along with the base pressure. The flow structures near the wheels was analysed with four streamwise-normal planes. All measurements were taken using DEWESoft equipment and software. The data was then processed and analysed using MATLAB software.

3.1.2.1 Wheel house pressure measurements

The wheel house pressure measurements were taken at the front left wheel house, see Fig. 3.3. Transient sensors were used, sampling at 5000 Hz for 5 s each sample. The measurement samples were taken along with the force measurements at 140 km/h. The sensors (circled in the figure) were mounted on the back of the wheel house to eliminate their flow interference.

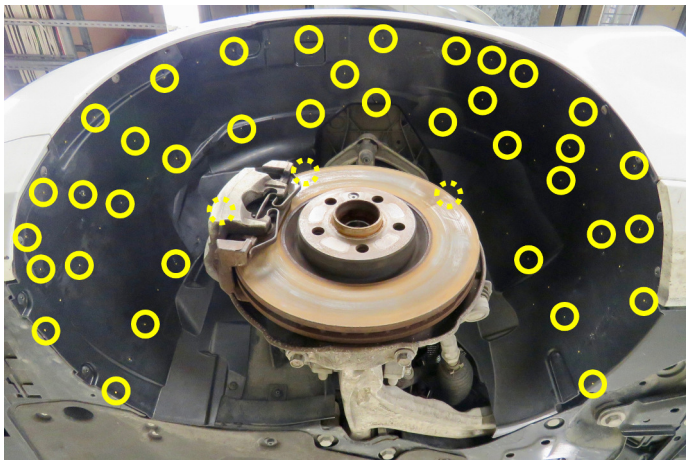

Figure 3.3: Front wheel house pressure setup.

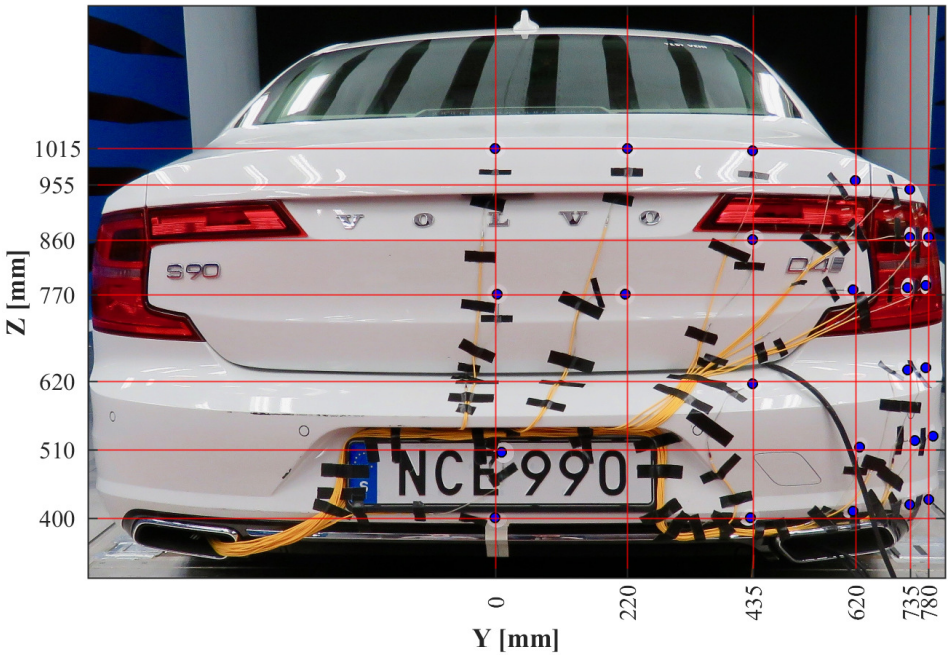

Figure 3.4: The base pressure grid.

3.1.2.2 Base pressure measurements

For the surface pressure of the base, 25 sensors were aligned according to the grid in Fig. 3.4. A laser alignment tool was used to place the sensors in the grid, but the curvature of the rear end and the angle of the photograph misaligned some of the sensors from the grid in the figure.

3.1.2.3 Flow field measurements

A portable traverse gear was used to take the flow field measurements, see Fig. 3.5a. The traverse could move in the Y and Z directions, but had to be manually moved

(a) The traverse gear

(b) The two 12-hole omniprobes mounted on the traverse arm.

Figure 3.5: Flow field measurement setup.

into a new X position. Two 12-hole omniprobes were mounted onto the traverse arm. The omniprobes enabled precise measurements of velocity magnitude, flow direction and pressure. Flow field measurements were taken on a selected few of the wheel configurations. Four wake planes were measured, two at the front wheel and two at the rear wheel, see Fig. 3.6. The plane numbering was set as the order of prioritisation. The wind tunnel testing time limited the project to the four planes shown in the figure. *Plane 1* was at $X = 0$ mm (at the front axle), *Plane 2* was 500 mm downstream of the front axle. *Planes 4* and *3* was 500 mm upstream and downstream of the rear axle, respectively. All the planes were located 30 mm from the vehicle and 25 mm off the ground, with a grid spacing of 50 mm.

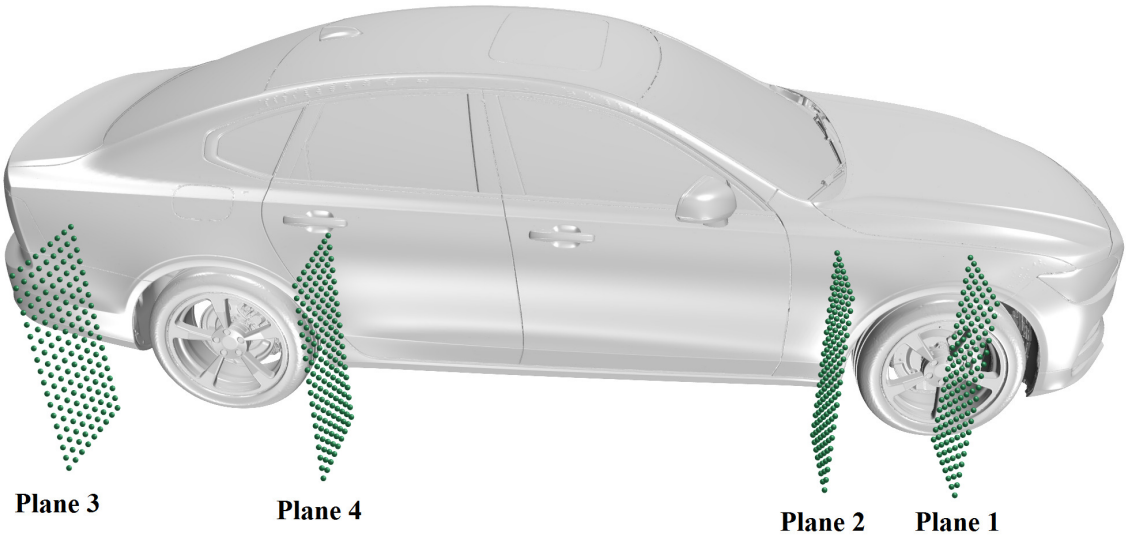

Figure 3.6: The sampling points in the four wake planes, numbered in order of prioritisation.

(a) Test object 1 (main): the Volvo S90.

(b) Test object 2 (secondary): the Volvo V90.

Figure 3.7: The test vehicles used throughout the project.

3.2 Test setup

The experimental investigation was divided into two wind tunnel sessions. The first session focused on a screening of a large number of wheel parameters, to exclude those that did not affect the aerodynamic drag and to find the most important parameters. Only the main test object, see Fig. 3.7a, was used during this screening. A more detailed parameter investigation of the important wheel parameters, was then performed in the second wind tunnel session, where both test objects were included.

3.2.1 Test objects

The study used two test objects, see Fig. 3.7. Both the numerical and the experimental investigation was performed using test object 1. Test object 2 was added to expand the study in the second wind tunnel session, taking force measurements only. The pressure and flow field measurements were only performed on test object 1. Two sets of wheels were used during the thesis, the *base wheels* (further explained below) and a set regular production wheels, called the *donor wheels*. Both these sets of wheels were equipped with new 245/45 R18 tires of the same model, although not from the same manufacturing batch.

3.2.2 Modular wheel concept

The experimental testing concept used in the project was a further development of a previous thesis work at Volvo Cars [32]. The concept included a slim wheel, see Fig. 3.8a, called the base wheel on which plastic inserts were mountable, see Fig. 3.8b. The additive manufacturing technique of selective laser sintering (SLS) was used to produce the nylon (polyamide) inserts, allowing for high design freedom. Since the inserts were easy to mount and dismount, the wheel geometries could time-efficiently be changed during the wind tunnel sessions. In addition, this also proved to be a cost-efficient way of testing many wheel configurations [32]. The design process and fatigue analysis of the base wheel along with a more detailed description of the plastic inserts can be found in Appendix A.

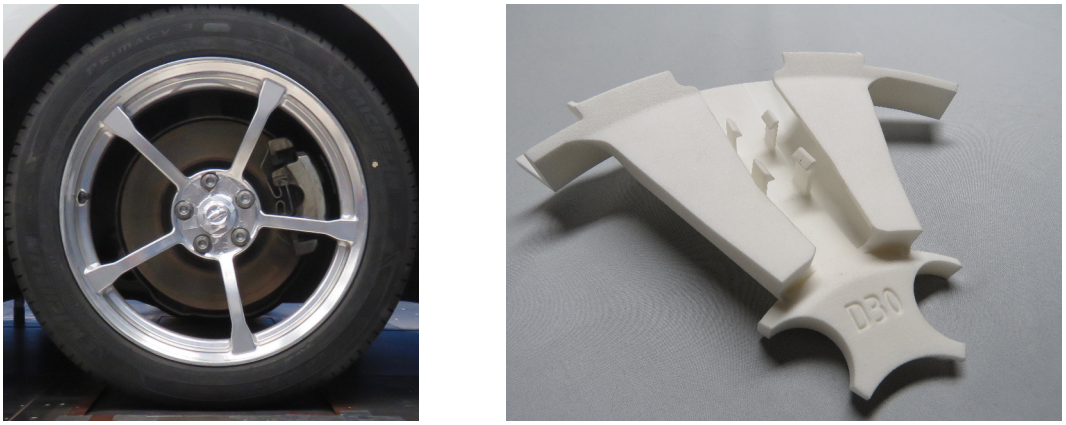

(a) Base wheel. **(b)** Plastic insert.

Figure 3.8: The experimental testing concept.

3.2.3 Wheel parameters

A wheel can be geometrically constructed by many different parameters. To choose the most useful parameters for aerodynamic wheel development, the project had a close collaboration with the design department at VCC. By doing so, the results found in this thesis could more easily be used when designing a new stylish aerodynamic wheel. This collaboration resulted in 14 parameters to investigate, see Table 3.2. An already known parameter, in terms of aerodynamic drag, is the projected coverage area of the wheel (No. 1) [33]. Another basic parameter is the number of spokes (No. 14). Parameters No. 2-8 is shown in Fig. 3.9a, while parameters No. 9-13 is shown in Fig. 3.9b.

Previous studies indicated that covering the outer part of the wheel has a high impact on the aerodynamic performance [33]. Hence, three parameters were chosen to investigate the rim cover (No. 2-4), see Fig. 3.9a. Parameter No. 5 and 6 dictates when the spoke breaks in towards the centre and to what depth, respectively. These are general features used by the designers to create visually interesting wheels. Another important design feature was the drop angle (No. 7), which did not affect the coverage area, but made the top surface of the spokes smaller and created angled sides of the spokes. Lastly in Fig. 3.9a, the spoke end radius (No. 8) is visualised.

The concavity of the spoke (No. 9) is a measure determining how concave or convex the spoke is. The centre value of this feature will generate a normal flat spoke. The spoke edge radius (No. 10) and the spoke window width (No. 11) were interesting parameters for both the styling of the wheel and for the understanding of wheel aerodynamics. Finally, the rim track design (No. 13) is visualised in the cross section view in Fig. 3.9b, in this case with the concave profile. Three different rim track profiles where chosen (concave, convex and technical) to find if any of them were preferred, from an aerodynamic perspective.

Table 3.2: The wheel parameters investigated during the thesis work.

No.	Name	Screening	DPI
1	Coverage area		x
2	Rim cover distance		x
3	Rim cover depth	x	x
4	Rim cover angle	x	x
5	Position of break	x	
6	Depth of centre	x	x
7	Drop angle		x
8	Spoke end radius	x	
9	Concavity of spoke	x	
10	Spoke edge radius	x	
11	Spoke window width	x	x
12	Diamond cut	x	
13	Rim track design	x	
14	Number of spokes	x	
		$\sum$ **11**	$\sum$ **7**

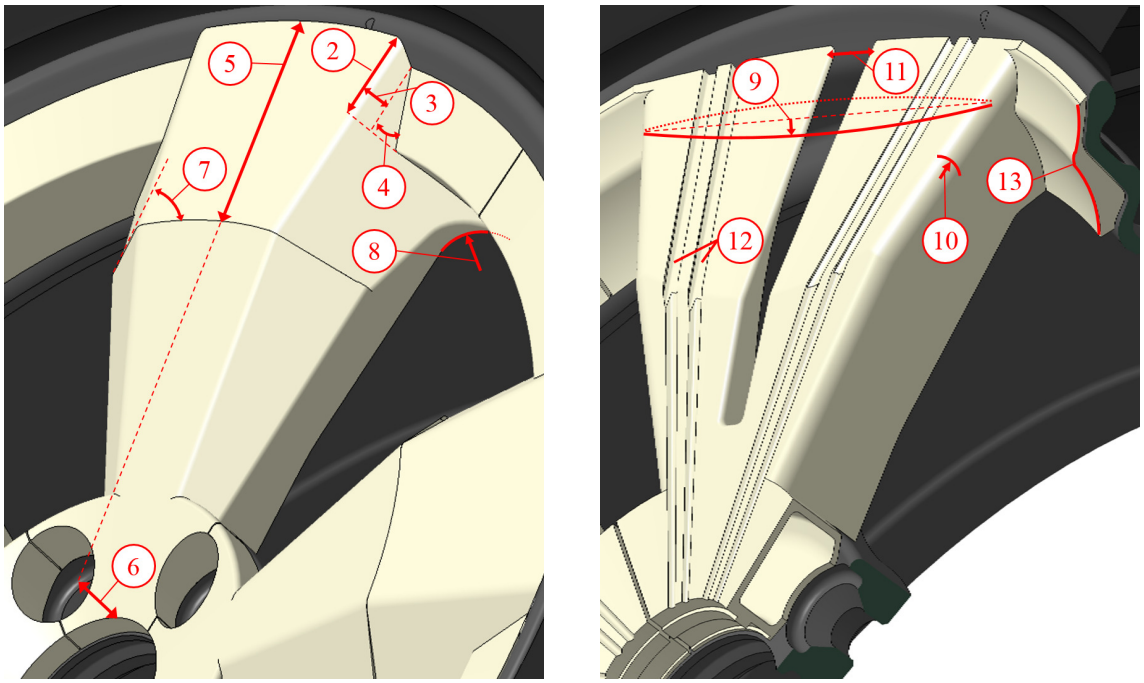

(a) Wheel parameters 2-8. **(b)** Wheel parameters 9-13.

Figure 3.9: A representation of all the wheel parameters.

3.2.4 Evaluation procedure

The first part of the evaluation procedure was to verify that the modular wheel concept, described in Section 3.2.2, could accurately represent production wheels. This evaluation was done by first comparing the aerodynamic drag coefficient, C_D, when mounting cover plates on the base wheels and on the donor wheels, to obtain the influence of the two different tire batches, see Fig. 3.10a. Thereafter, the

(a) Mounted cover plate. **(b)** Donor wheel. **(c)** Concept (S19).

Figure 3.10: Evaluation of the modular wheel system.

concept was evaluated by comparing the donor wheel to a set of plastic inserts with identical outer geometry, see Fig. 3.10b and 3.10c, while taking the tire influences into account.

Three separate experimental investigations were performed. The first investigated the coverage area (No. 1) at 40 %, 65 % and 90 % coverage. The second investigation analysed the effect of the rim track design (No. 13). The *technical*, *convex* and *concave* rim track profiles were investigated. Finally, the third separate study investigated an asymmetric rim cover and its dependence on the direction of rotation.

To be able to evaluate all the parameters listed in Table 3.2 and to develop the generic guidelines for aerodynamic wheel development, statistical methods were utilised. The evaluation procedure can be seen in Fig. 3.11. The screening tests used a statistical method to evaluate the importance of 11 wheel parameters, while the detailed parameter investigation (DPI) used another method which could give a more in-depth analysis of 7 wheel parameters. The results from the screening was used to decide which parameters to further investigate in the DPI. The screening results were also used to improve the final regression model.

All parameters were defined so that they geometrically varied from a minimum value (−) to a maximum value (+). The coverage area was, for example, set to 60 % covered at its minimum and 80 % covered as its maximum during the DPI. All parameters needed to be able to geometrically exist with every other parameter

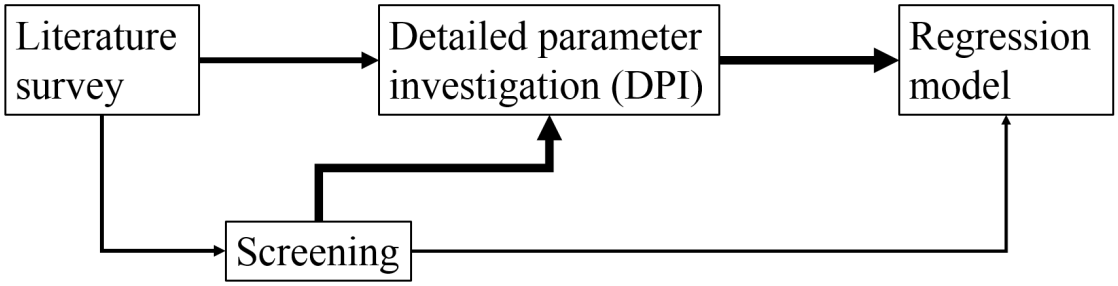

Figure 3.11: Flow chart of the statistical evaluation process.

on their maximum and minimum levels, for both the screening and the DPI tests. Within this restriction, the geometrical range between the minimum and maximum levels was set to be as large as possible in order to yield a distinct response in terms of C_D value. All test runs were randomised, and the data was analysed using the statistical tools in Minitab and MATLAB.

3.2.4.1 Screening tests

The 11 parameters evaluated during the screening could all affect the aerodynamic drag, based on engineering judgement. Not enough previous research of these parameters could be found, and they were thus chosen for the screening tests. The screening consisted of a Plackett-Burman design test matrix, see Table 3.3. The Plackett-Burman screening method theory is further explained in Section 2.3.3.

The Plackett-Burman test matrix requires 12 configurations when evaluating 10 parameters (the rim track design were evaluated separately due to geometrical constraints). Two centre points (CP), one at the integer value of 5 spokes and one at 10 spokes, were included to investigate the linearity of the parameter effects. Finally, configuration S19 used in the modular wheel concept evaluation can be seen in Table 3.3. All of the wheel configurations can be seen in Fig. 3.12.

Table 3.3: The screening test matrix setup with the parameter maximum (+), minimum (−) and centre values (0). The rest does not apply to this system.

		Parameter									
Config.		Rim cover depth	Rim cover angle	Position of break	Depth of centre	Spoke edge radius	Spoke end radius	Number of spokes	Spoke window width	Concavity of spoke	Diamond cut
Plackett-Burman	S01	+	−	+	−	−	−	+	+	+	−
	S02	+	+	−	+	−	−	−	+	+	+
	S03	−	+	+	−	+	−	−	−	+	+
	S04	+	−	+	+	−	+	−	−	−	+
	S05	+	+	−	+	+	−	+	−	−	−
	S06	+	+	+	−	+	+	−	+	−	−
	S07	−	+	+	+	−	+	+	−	+	−
	S08	−	−	+	+	+	−	+	+	−	+
	S09	−	−	−	+	+	+	−	+	+	−
	S10	+	−	−	−	+	+	+	−	+	+
	S11	−	+	−	−	−	+	+	+	−	+
	S12	−	−	−	−	−	−	−	−	−	−
CP	S13	0	0	0	0	0	0	−	0	0	0
	S14	0	0	0	0	0	0	+	0	0	0
Rim track design	S15			0	0	0	0	−	0	0	0
	S16			0	0	0	0	−	0	0	0
	S17			0	0	0	0	−	0	0	0
	S18			0	0	0	0	−	0	0	0
	S19										

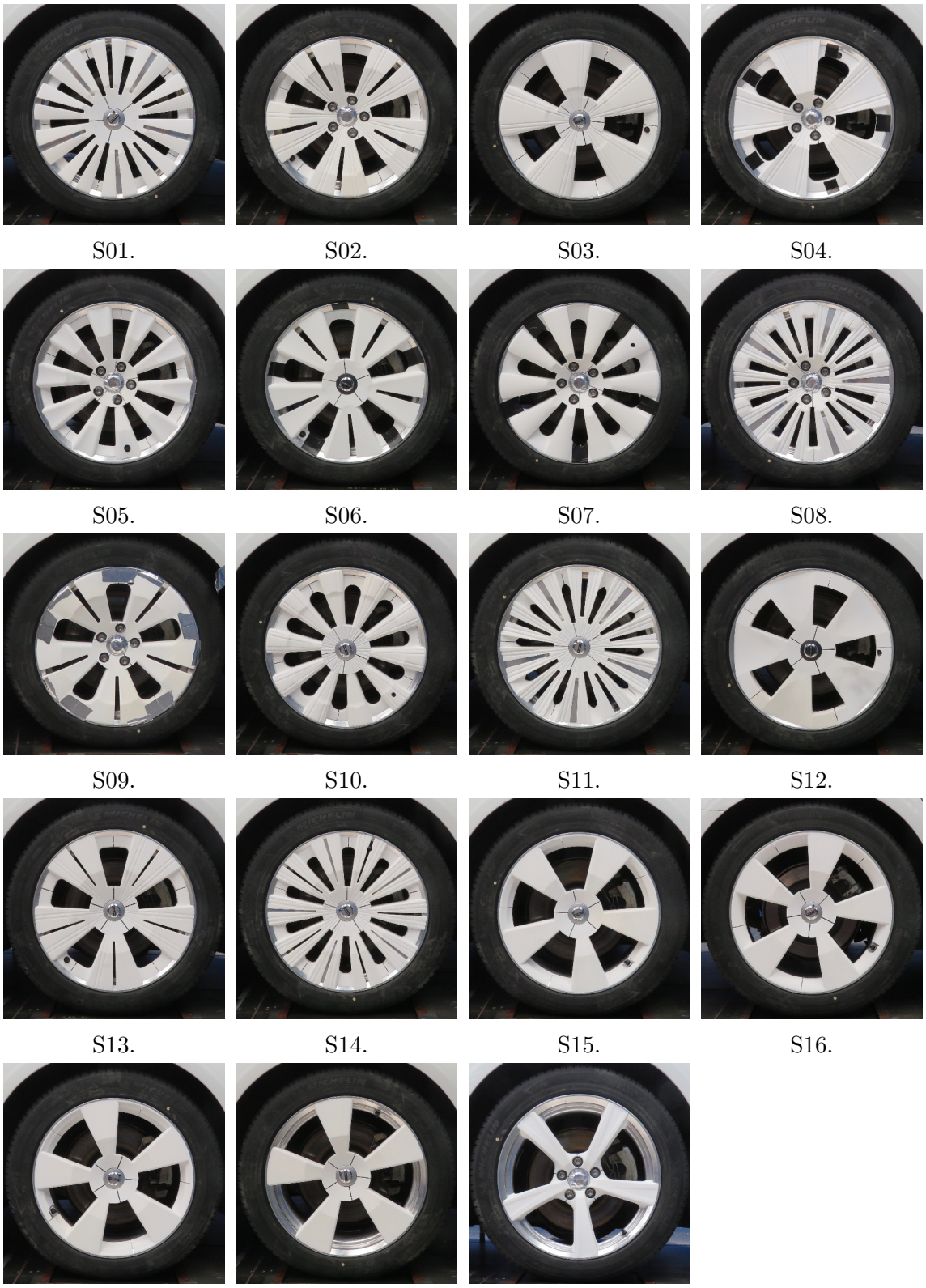

Figure 3.12: The screening wheel configurations.

3.2.4.2 Detailed parameter investigation

Parameters No. 3, 4, 6 and 11 were found to be important in the screening process. The literature survey provided the coverage area (No. 1) and the rim cover distance (No. 2), while the drop angle (No. 7) was selected based on discussions with the design department at VCC. These seven features were included in the detailed parameter investigation (DPI).

However, the geometrical restrictions prevented the project to include all seven parameters into one fractional factorial design (FFD) matrix (see Section 2.3.2 for more information about FFD matrix setups). Therefore, the seven parameters were divided into three different FFD test matrices, see Table 3.4. As seen in the table, each FFD included five parameters meaning that each FFD would require 16 wheel configurations (according to Table 2.1). This gave the resolution of IV, meaning that third order effects and higher were neglected. Many of the parameters were included in multiple FFD designs, see Table 3.4. This meant that many of the wheel configurations generated by the FFD matrices were duplicates and thus only 32 unique wheel configuration were needed instead of 48. The 32 wheel configurations can be seen in Table 3.5 along with three centre points, one for each FFD.

The drawback of this method was that the second order interaction effects (synergism) between the parameters not present in the same FFD were lost. These interaction effects were:

1. Coverage area & Drop angle
2. Spoke window width & Drop angle
3. Spoke window width & Rim cover distance

It was assumed that these effects could be neglected since they were all geometrically independent. The DPI was performed during the second wind tunnel session. At this session, the separate study of the coverage area along with the study of the asymmetric rim cover were also performed. Those configurations can be seen at the end of Table 3.5, along with D41 (identical to D02, except for the rim cover distance). All the tests were performed on test object 1 and 2. All wheel configurations can be seen in Fig. 3.15. Flow field measurements were performed on configurations D36, D38, D09, D15, D02, D41 and a 100 % covered wheel, as a reference.

Table 3.4: The three fractional factorial designs and their included parameters.

Name	FFD 1	FFD 2	FFD 3
Coverage area	x	x	
Rim cover distance	x		x
Rim cover depth	x	x	x
Rim cover angle	x	x	x
Depth of centre	x	x	x
Spoke window width		x	
Drop angle			x

Table 3.5: The detailed parameter investigation (DPI) test matrix with the parameter maximum (+), minimum (−) and centre values (0).

	Config.	Parameter						
		Coverage area	Rim cover dept	Rim cover angle	Rim cover distance	Depth of centre	Spoke window	Drop angle
Fractional factorial design	D01	−	−	−	−	+	−	+
	D02	+	−	−	−	−	−	+
	D03	−	+	−	−	−	−	+
	D04	+	+	−	−	+	−	+
	D05	−	−	+	−	−	−	+
	D06	+	−	+	−	+	−	+
	D07	−	+	+	−	+	−	+
	D08	+	+	+	−	−	−	+
	D09	−	−	−	+	−	−	+
	D10	+	−	−	+	+	−	+
	D11	−	+	−	+	+	−	+
	D12	+	+	−	+	−	−	+
	D13	−	−	+	+	+	−	+
	D14	+	−	+	+	−	−	+
	D15	−	+	+	+	−	−	+
	D16	+	+	+	+	+	−	+
	D17	−	−	−	−	−	+	+
	D18	+	−	−	−	+	+	+
	D19	−	+	−	−	+	+	+
	D20	+	+	−	−	−	+	+
	D21	−	−	+	−	+	+	+
	D22	+	−	+	−	−	+	+
	D23	−	+	+	−	−	+	+
	D24	+	+	+	−	+	+	+
	D25	+	−	−	−	+	−	−
	D26	+	−	−	−	−	−	−
	D27	+	−	+	−	−	−	−
	D28	+	+	+	−	+	−	−
	D29	+	−	−	+	−	−	−
	D30	+	+	−	+	+	−	−
	D31	+	−	+	+	+	−	−
	D32	+	+	+	+	−	−	−
CP	D33	0	0	0	0	0	−	+
	D34	0	0	0	−	0	0	+
	D35	+	0	0	0	0	−	0
Coverage extremes	D36	40 %	0	0	15 mm	0	0	0
	D37	65 %	0	0	15 mm	0	0	0
	D38	90 %	0	0	15 mm	0	0	0
Asym.	D39	−	0	0	+	0	0	0
	D40	−	0	0	+	0	0	0
	D41	+	−	−	+	−	−	+

D01. D02. D03. D04.

D05. D06. D07. D08.

D09. D10. D11. D12.

D13. D14. D15. D16.

D17. D18. D19. D20.


D21.


D22.


D23.


D24.


D25.


D26.


D27.


D28.


D29.


D30.


D31.


D32.


D33.


D34.


D35.


D36.


D37.


D38.


D39.


D40.

D41.

Figure 3.15: The wheel configurations from the detailed parameter investigation.

3.3 Numerical procedure

The numerical simulations were performed utilising computational fluid dynamics (CFD) through the commercial software STAR-CCM+ (v12.04) by CD-adapco. Geometry cleaning and pre-processing were done in ANSA supplied by BETA CAE Systems while volume meshing, domain setup and post processing were done in STAR-CCM+. Simulation scripts created by Siemens, named VSIM, were used to set up the domain and to ramp up the simulation. The cell count of the volume mesh was 280 million cells. Six layers of prismatic cells with a first cell height of 0.015 mm was set on all surfaces besides the rotating wheels where eight prismatic cells with first cell height of 0.01 mm was used, corresponding to $y^+ < 1$. This, to ensure that the full boundary layer was resolved, see Fig. 2.1. The minimal target cell size of the domain was 0.16 mm to capture the flow where strong gradients and separation could occur.

The numerical simulations were set up to model test object 1 with wheel configurations D36 and D38 at open and closed cooling flow.

3.3.1 Solver setup

The fluid domain used in the simulations can be seen in Fig. 3.16. The size of the inlet was adapted so that the blockage area of the vehicle was less than 1 %. This was considered sufficient since the blockage area of the vehicle used in the wind tunnel experiments covered about 9 % of the cross section. The vehicle was positioned at one third the distance from the inlet, see Fig. 3.16.

To model the unsteady flow around the vehicle, the transient SST k-ω IDDES turbulence model was used, see Section 2.2.1. A 2$^{\text{nd}}$-order temporal discretization was used with a time step of $5 \cdot 10^{-4}$ s. This resulted in a Courant number, C, above 1. However, it has been found that modelling wheel rotation does not require a Courant number below 1, since a similar simulation setup investigated time steps of $1 \cdot 10^{-4}$ s ($C > 1$) and $1 \cdot 10^{-5}$ s ($C < 1$), with negligible differences [28].

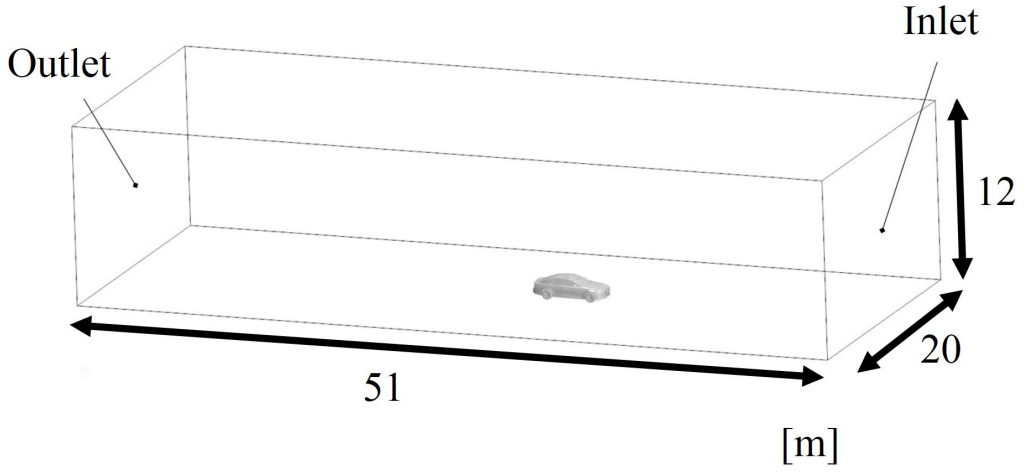

Figure 3.16: The size of the fluid domain with test object 1 placed inside.

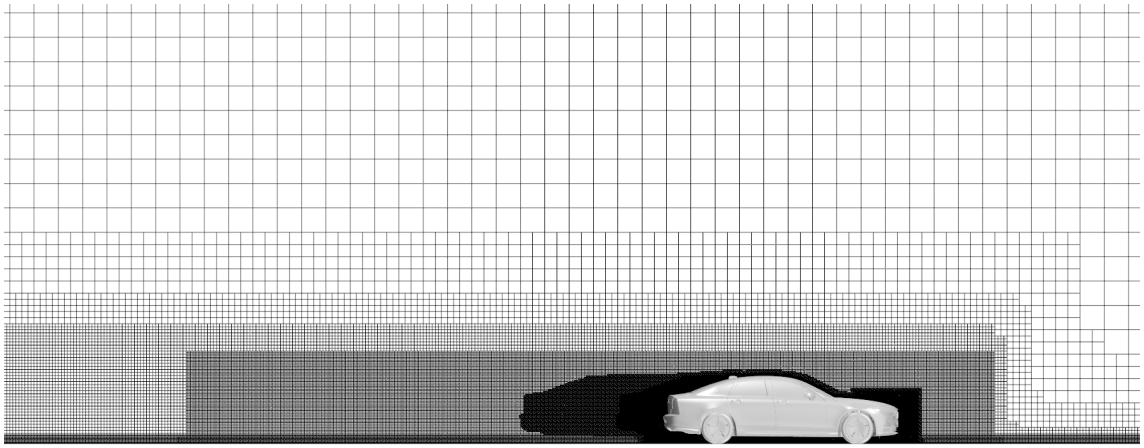

Figure 3.17: Plane section of the volume mesh, presenting the mesh refinement.

The solver ran for a total of 6 s (physical time) whereas the sliding rotations of the wheels were activated after the first 3 s. The sought drag coefficient, C_D, was averaged during the last 2 s when the solution was stable. It has been proven that averaging for a longer time does not significantly improve the accuracy of the results [28].

The trimmed mesh around the vehicle can be seen in a plane section view in Fig. 3.17. Several refinement boxes were placed around the vehicle and ground and three wake refinements were set on the vehicle geometry in a downstream direction to fully resolve the wake structures.

3.3.2 Boundary conditions

The inlet and outlet of the domain were defined as a velocity inlet and a pressure outlet, respectively, while the rest of the outer domain surfaces, excluding the floor, were set as symmetry planes. The floor was defined with a moving wall (MW) condition, having the same tangential velocity as the inlet flow of 140 km/h. Furthermore, the inlet turbulent intensity and turbulent viscosity ratio were set to 0.001 and 200, respectively, to facilitate convergence. The direction of the inlet flow was normal to the inlet (no yaw). The vehicle itself was given a no-slip wall boundary condition, except for the wheels, the radiator, the A/C condenser, the charge air cooler (CAC) and the fan. The exceptions are described below.

3.3.2.1 Porous media

To properly model the pressure drop caused by the underhood components; the radiator, the A/C condenser and the CAC, a porous media modelling was used. In STAR-CCM+, a porous media is modelled by adding a source term f_p into the momentum transport equation (Eq. 2.5 in Section 2.1.1.1) to estimate the momentum sink [34]. This source term accounts for the added flow resistance and contain a viscous and an inertial resistance term determined by experimental data of the underhood components.

3.3.2.2 Modelling fan

The fan is used to suck air flow through the other underhood components. In the numerical setup, this motion is modelled by a multiple reference frame (MRF) setup, see Section 2.2.2.3. The fan motion was only modelled when simulating open cooling flow.

3.3.2.3 Modelling wheels and tires

When modelling the rotation of the wheels, a sliding mesh region was setup at the wheels, see Fig. 3.18. The green region represents the sliding mesh which rotated each time step. Hence, this domain must be rotationally symmetric and this is why the tire was not included into the sliding mesh domain. As described in Section 2.1.2.2, the axle load will deform the tire at the ground contact patch making it asymmetrical. A moving wall boundary condition was applied to the tire, which is valid since it can accurately model rotations on surfaces non-normal to the rotation. The sliding domain was meshed with a trimmed mesher with the same settings as the outer domain. The cells at the interface have a fixed cell size of 1 mm to create a smooth flow transition between the two domains.

The tire will not only deform due to the axle load, it will also expand radially due to the rotation and similarly contract axially, as explained in Section 2.1.2.2. Hence, using un-deformed tire geometries for the simulation setup would yield incorrect results. Therefore, a cooperation with a tire manufacturer was established to provide the project with deformed tire geometries. The tire requirements can be seen in Table 3.6. The same camber angle, velocity and tire pressure were set for the front and rear tires. The axle load, corresponding to Curb + 2, was higher at the front compared to the rear axle. The deformed tires could only be provided with the

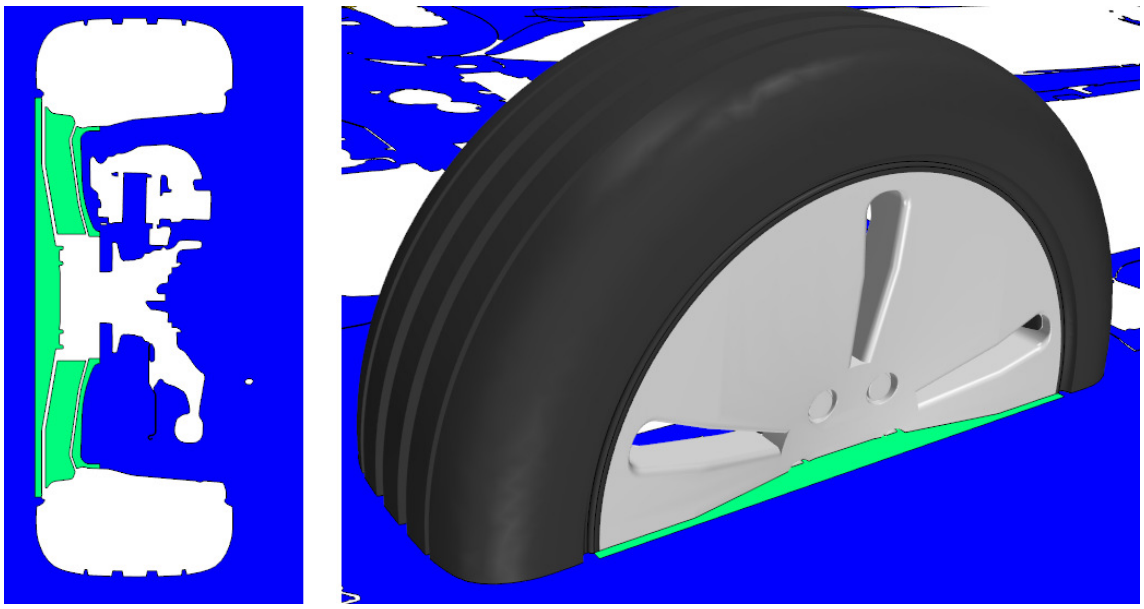

Figure 3.18: The sliding mesh setup, with the sliding mesh domain (green) and the outer domain (blue). Left) a cross section view of the wheel. Right) a perspective view of the front left wheel.

Table 3.6: Requirements for the deformed tires.

Tire	Axle load (per wheel) [N]	Camber angle [deg]	Velocity [km/h]	Tire pressure [bar]
Front	5275	1.0	140	2.5
Rear	3875	1.0	140	2.5

rotationally symmetric rain grooves and not any lateral tire patterns. Luckily, it has been proven that the rain grooves are the most important tire pattern in terms of simulation accuracy [28]. The tire geometry can be seen in Fig. 3.19. The contact patch and the tire bulge on the sides are clearly visible.

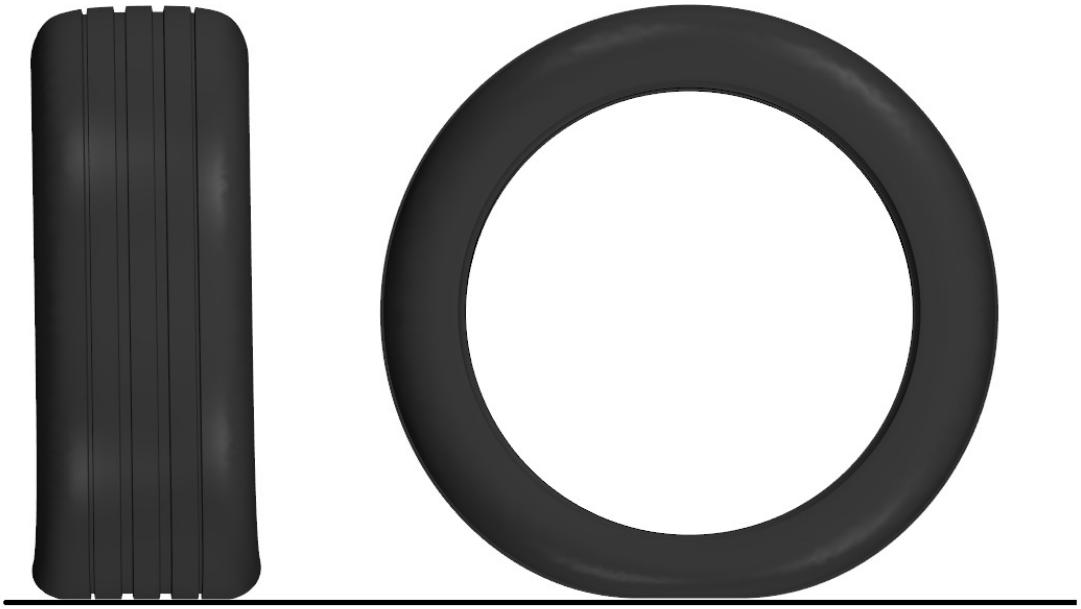

Figure 3.19: The deformed tire geometry received from the tire manufacturer. The geometry is expanded radially due to rotation and deformed at the contact patch due to the axle load of the vehicle.

4 Results and discussion

This chapter presents and analyses the results found in both the experimental and numerical investigations. The experimental investigations will be presented first. At the end, the results from the numerical part will be presented and compared to the wind tunnel results to validate the numerical simulations. Once validated, the numerical results will be used to further analyse aspects of wheel aerodynamics not investigated in the experimental study.

4.1 Experimental analysis

The experimental analysis, performed during two wind tunnel sessions, focused on utilising statistical methods to study the different wheel parameters' effects on the aerodynamic drag. However, many separate studies were also performed during the wind tunnel sessions. This section will start to present the findings in the separate studies and continue with the statistical wheel parameter investigations. Finally, an aerodynamic analysis using the flow field, wheel house pressure and base pressure measurements will present explanations of why certain wheel parameters highly affect the aerodynamic performance.

4.1.1 Verifying the modular wheel concept

The results of the concept verification, described in Section 3.2.4, can be seen in Table 4.1. By first comparing the base wheel (BW) and the donor wheel (DW) when mounting cover plates on the wheels, the tire differences due to different production batches could be isolated. The tire batch differences were of -2 and -1 drag counts (ΔC_D = -0.002 & -0.001) for open and closed cooling flow, respectively. If the modular wheel concept was perfect, the same difference would be seen between the donor wheel and S19 (which both have identical geometries), again due to the tire differences. However, as seen in Table 4.1, the differences were not the same resulting in a $\Delta\Delta C_D$ of 2 counts for closed cooling and 1 count for open cooling flow. Thus, the modular wheel concept gave slightly different absolute values of aerodynamic drag compared to a real production wheel. However, the differences were small, so the concept was considered to represent real wheels adequately.

Table 4.1: The difference between the base wheel (BW) and the donor wheel (DW) when using cover plates along with the difference found between the donor wheel and the modular wheel concept (S19) resulting in a difference isolated to the concept, for both open and closed cooling flow.

	Cover plates		
	BW - DW	**S19 - DW**	
Cooling flow	$\boldsymbol{\Delta C_D}$	$\boldsymbol{\Delta C_D}$	$\boldsymbol{\Delta\Delta C_D}$
Open	-0.002	-0.001	0.001
Closed	-0.001	0.001	0.002

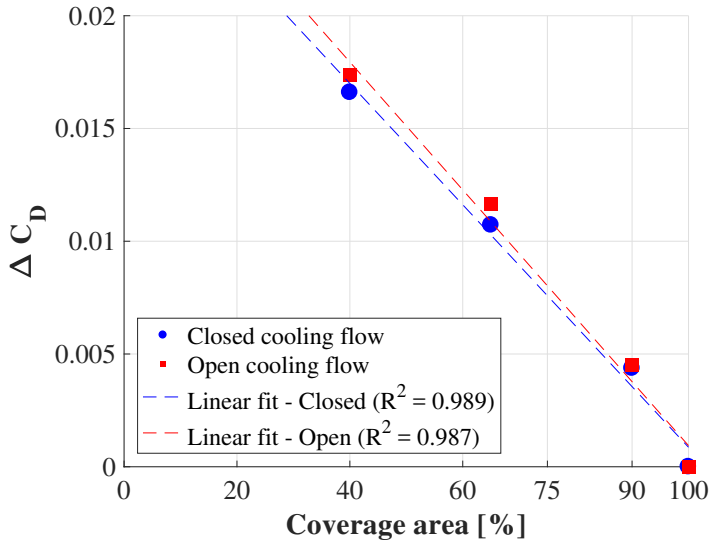

Figure 4.1: The isolated effect of the coverage area on the aerodynamic drag, for both open and closed cooling flow. A linear fit is shown for the two cooling configurations.

4.1.2 Separate evaluation of coverage area

Since the coverage area (No. 1) was one of the most important wheel parameters, a separate isolated evaluation of this parameter was done. A 40 % (D36), 65 % (D37) and a 90 % (D38) covered wheel were compared to the cover plate, see Fig. 4.1. It is evident that the coverage area has a linear effect on the aerodynamic drag.

Table 4.2: The effect of different rim track designs on the aerodynamic drag, for both open and closed cooling flow. S15 uses the *technical* rim track of the base wheel and was set as reference. See Fig. 4.2 for a cross section view of the designs tested.

	S15	**S16**	**S17**	**S18**
ΔC_D (Open)	Ref.	-0.001	-0.001	-0.002
ΔC_D (Closed)	Ref.	-0.002	-0.002	-0.002

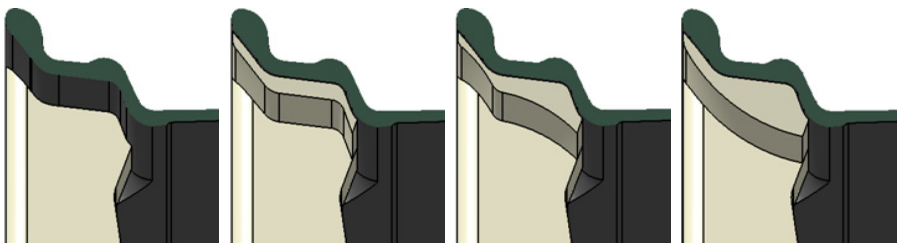

(a) S15 (Technical). **(b)** S16 (Technical). **(c)** S17 (Concave). **(d)** S18 (Convex).

Figure 4.2: Cross section view of the rim track geometries tested during the screening test session.

4.1.3 Evaluation of the rim track design

The rim track design (No. 13) was investigated separately during the screening test session. The four rim track designs tested can be seen in Fig. 4.2 and the results can be found in Table 4.2. Configuration S15, used the *technical* rim track profile of the base wheel (in grey) and was set as reference. The same profile was used in the S16 plastic insert (in white). A slight decrease in drag was seen for S16, even though the same rim track design was used. This was expected since S16 builds inwards and decreases the opening diameter of the wheel by 0.5 inches. However, when comparing S16, S17 and S18, no significant change could be seen between the three rim track designs. This indicated that the rim track design does not change the aerodynamic performance of the wheel. All four configurations had the same coverage area.

4.1.4 Evaluation of asymmetric wheel design

The effect of asymmetric wheel design was also evaluated separately. This study investigated the effect of a triangularly shaped rim cover and if the direction of rotation of that asymmetric geometry would matter. Table 4.3 presents the results and the corresponding geometries can be seen in Fig. 4.3. The configurations D40a and D40b, in Fig. 4.3c and 4.3d, have mirrored wheel geometries on the opposite sides, to ensure the correct indicated direction of rotation on both sides of the vehicle. The asymmetric wheel configurations were designed with the same total coverage area as the D09 reference configuration. In addition, they were also designed with equal coverage area corresponding to the rim cover. Thus, from Table 4.3, it was evident that a wheel can have an asymmetric rim cover without affecting its aerodynamic performance.

Table 4.3: The effect of asymmetric wheel design on the aerodynamic drag. See Fig. 4.3, where the evaluated configurations are shown.

	D09	**D39**	**D40a**	**D40b**
ΔC_D (Open)	Ref.	0.000	0.000	0.000
ΔC_D (Closed)	Ref.	0.000	0.000	-0.001

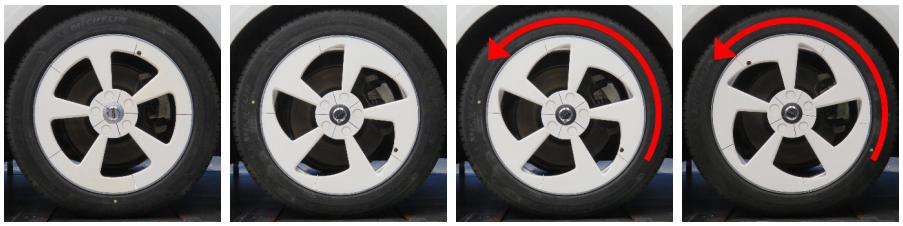

(a) D09. **(b)** D39. **(c)** D40a. **(d)** D40b.

Figure 4.3: The different configurations tested during the asymmetric wheel evaluation. (a) and (b) have the same geometries for the right and left side of the vehicle, while (c) and (d) have mirrored geometries on the opposite sides to ensure the correct indicated direction of rotation.

4.1.5 Experimental wheel parameter investigation

The experimental wheel parameter investigation consisted of a screening, where the least important parameters could be distinguished and excluded, and a detailed parameter investigation (DPI) where the most important parameters were investigated in depth, to create an accurate regression model.

4.1.5.1 Screening

The test matrix was developed using the Plackett-Burman method, described in Section 3.2.4.1, resulted in a ranking of significance depending on the coefficient of drag, C_D. The significance of the 10 parameters included in the screening can be seen in Fig. 4.4. A high standardized effect indicates that the parameter has a high influence on the aerodynamic drag. The red dashed vertical line displays the significance limit (based on a p-value of 0.05), see Section 2.3.3 for the theory of the Pareto chart. The bottom three parameters (No. 5, 12 and 9) in the figure were thus insignificant and could be assumed to have no impact on the C_D value. Parameters No. 4, 6, 3 and 11 had the highest standardized effects and were selected for closer evaluation in the detailed parameter investigation. The rest, parameters No. 10, 8 and 14, could not be analysed further due to the limitation on the number of tests. Fig. 4.4 shows the results for closed cooling flow, but similar results were found for the open cooling flow.

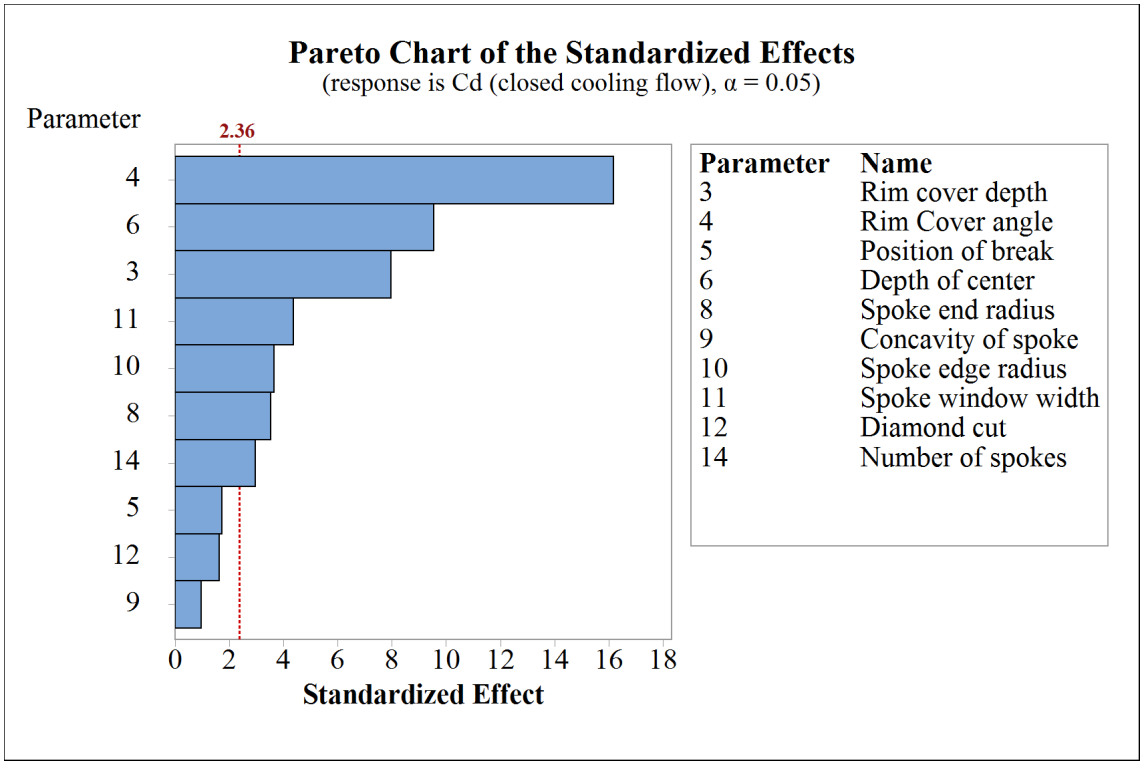

Figure 4.4: Pareto chart showing the significance of the 10 parameters investigated during the screening. The vertical red dashed line represents the significance level corresponding to a p-value of 0.05.

4.1.5.2 Detail parameter investigation

The four most important parameters found in the screening along with parameters known to be important from the literature survey were analysed in the detailed parameter investigation (DPI). The DPI was constructed from three fractional factorial designs, resulting in 35 wheel configurations, see Section 3.2.4.2.

When analysing the results from these tests, statistical software tools were utilised to find the parameters' first- and second-order effects with the aerodynamic drag as the response. Parameter effects with an insignificant impact on the aerodynamic drag could be neglected, similar to the screening exclusion of insignificant parameters. Once only the significant first- and second order effects remained, a linear regression model could be created based on these effects. The regression model predicted the C_D value by using constants, D_i, and the parameter levels, x_i, see Eq. 4.1.

$$C_D = D_0 + x_1 D_1 + x_2 D_2 + ... \tag{4.1}$$

The regression model was based on the significant effects found in the DPI, but the model used the data from the screening tests to improve the model. This was possible since the screening wheel configurations could be defined in terms of the parameters used in the DPI. The developed regression model could accurately predict the wheel configurations used in this project, see Fig. 4.5. The figure displays the difference in drag, ΔC_D, compared to a centre point configuration on the horizontal axis and, by the regression model, predicted drag difference on the vertical axis. Hence, a diagonal line can be drawn where the measured and predicted values are the same. An accurate regression model would thus predict values close to that line. The regression model developed in this project can therefore be considered accurate since the model has a R^2 fit of 0.939 and the largest residual was only two drag counts from its measured value. Two standard deviations of the residuals were 1.82

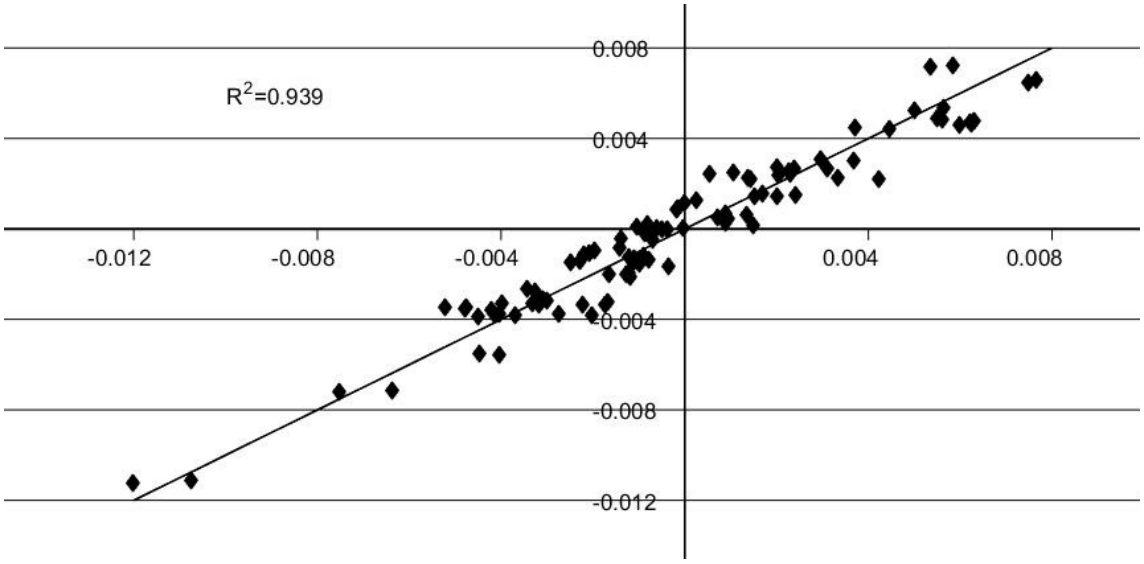

Figure 4.5: Measured vs. predicted ΔC_D for all configurations (including open and closed cooling flow) based on the developed regression model, with the centre point D33 as reference.

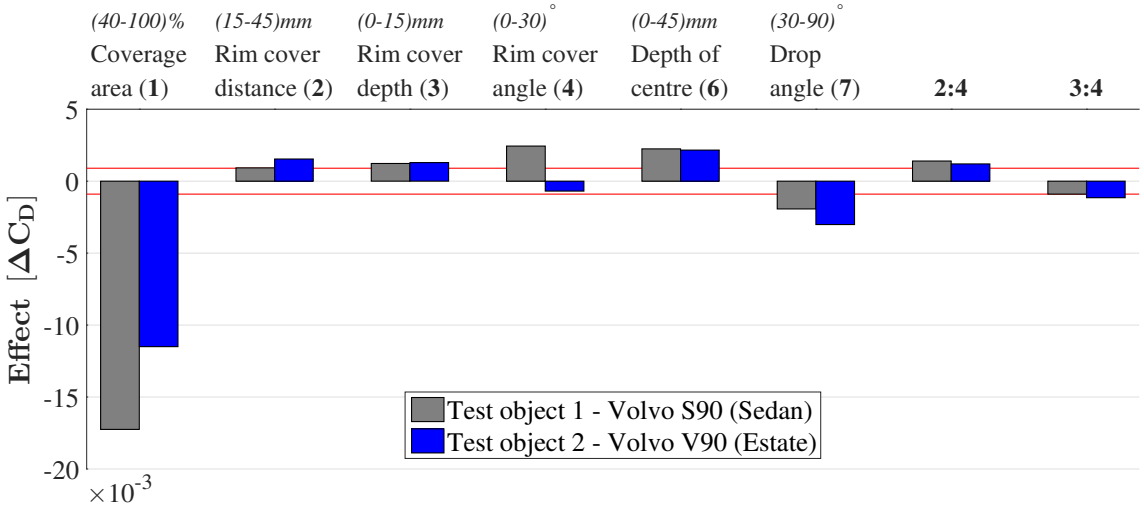

Figure 4.6: The magnitude of the significant parameter effects, for a sedan and estate type vehicle. **2:4** & **3:4** represent the second-order effect between the numbered parameters. The red horizontal lines indicate the significance limit.

drag counts, meaning that 95 % of the predicted wheel configurations will be within ±1.82 drag counts of the measured value. This was only slightly worse than the uncertainty of the wind tunnel, see Table. 3.1. However, the regression model was only tested on wheel configurations within this thesis work (the same configurations as the model was based on). Hence, it is expected that the predictions will differ more on other wheels, with different dimensions and tires.

Based on the regression model, it was possible to find every parameter's effect for the aerodynamic drag, see Fig. 4.6. The centre point configurations were not needed to describe the results, indicating that the parameters' effects were linear. The regression model was based on test object 1 (Volvo S90), represented in grey. The labelling also explains what geometrical changes that causes the displayed effects. It was evident that the coverage area (No. 1) had the highest effect on the drag, but it was not the only important parameter. The rim cover distance (No. 2) was found to have a low effect, but was used in the regression model since the parameter was a part of a synergy with the rim cover angle (No .4). The rim cover depth (No. 3) and the rim cover angle (No. 4) both caused a geometrical step between the rim cover and the top surface of the spoke. The effects of these parameters indicate that this increases the aerodynamic drag. Likewise, the depth of centre (No. 6) also increased the drag, proving that a flat wheel has a lower aerodynamic drag. Similarly, the effect of the drop angle (No. 7) suggests that the spoke coverage surface should be on the top surface of the wheel.

4.1.5.3 Comparison between sedan and estate type vehicles

The same DPI test setup, used for test object 1 (sedan), was performed on test object 2 (estate). Hence, it was possible to compare the wheel parameter effects of the two different vehicle types, see Fig. 4.6. The figure shows that the same trends can be seen for both vehicles, except that the rim cover angle (No. 4) seemed to be insignificant on the estate vehicle. The largest difference in magnitude of the

Table 4.4: The average difference in drag, $\Delta C_{D,\text{ open-closed}}$, between open and closed cooling flow. The average drag for open cooling flow was set as reference.

	Open cooling flow	Closed cooling flow	$\Delta C_{D,\text{ open-closed}}$
Average C_d of centre points	Ref.	-0.017	0.017

parameter effect was found for the coverage area (No. 1). This suggested that the coverage area was less important on an estate vehicle compared to a sedan.

4.1.5.4 Investigation of cooling flow impact on the aerodynamic drag

To investigate the effect of changing from open to closed cooling flow, all experimental tests were measured at both conditions. Similar first- and second-order effects were found to be significant independent of cooling flow. Therefore, an average difference in drag, $\Delta C_{D,\text{ open-closed}}$, between the open and closed cooling flow for the centre points D33 - D35 was defined, see Table 4.4.

It was investigated how this fixed difference could predict the C_D value of the closed cooling setup based on the open cooling flow drag for the same configurations, see Fig. 4.7. The figure shows that this model was accurate with a R^2 value of 0.984 and the largest residual was only one drag count from its measured value with two standard deviations of 0.96 drag counts, meaning that this had the same uncertainty level as the wind tunnel itself.

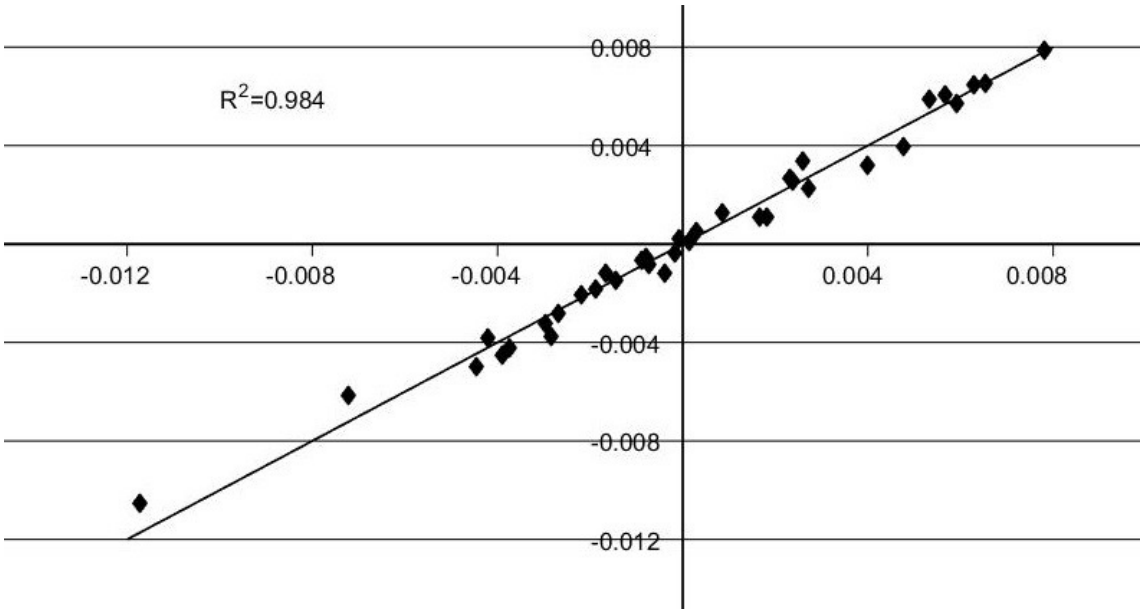

Figure 4.7: Measured vs. predicted ΔC_D of the closed cooling flow results, based on the fixed adjustment from the open cooling flow of the same configuration, with the centre point D33 as reference.

4.1.6 Aerodynamic analysis

It was important to understand why certain wheel configurations caused more or less aerodynamic drag, and also to understand why certain wheel parameters affected the drag more than others. Since a bluff body, like a vehicle, is dominated by pressure drag (see Section 2.1.2) there will often be a distinct difference in base pressure, between wheel configurations with high and low drag. Hence, this analysis will begin analysing the difference in base pressure and wheel house pressure between a typical low performing aerodynamic wheel and a high performing wheel. Thereafter, the base pressure in combination with the wheel wake measurements will explain differences depending on the individual wheel parameters.

4.1.6.1 General analysis of wheel house and base pressure

The wheel configuration with the lowest drag was the one with cover plates mounted on the wheels. This was expected. Likewise, the thin base wheel was the configuration with the highest drag. Looking at the base pressure in Fig. 4.8, it is evident that the covered wheel has a much higher base pressure when compared to the base wheel in Fig. 4.9. The region of higher pressure at the centre of the base is significantly larger for the high performing covered wheel. In addition, the low pressure at the bottom edges extends further in- and upwards in Fig. 4.9, for the base wheel. The low pressure region at the upper corner is more similar between the two wheels. The circles in the figures represent the sensor sampling positions.

Looking at the wheel house pressure, seen from below, it is evident that the pressure inside the wheel house drops when closing off the cooling flow. The reason could be

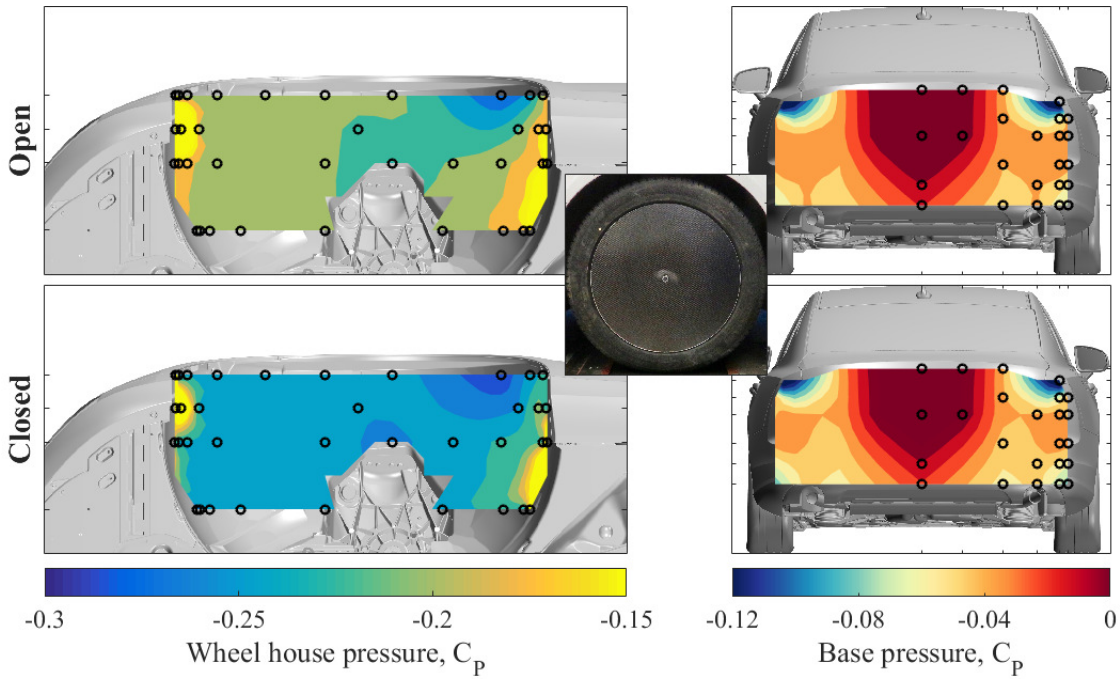

Figure 4.8: Cover plate. The wheel house and base pressure for open and closed cooling flow.

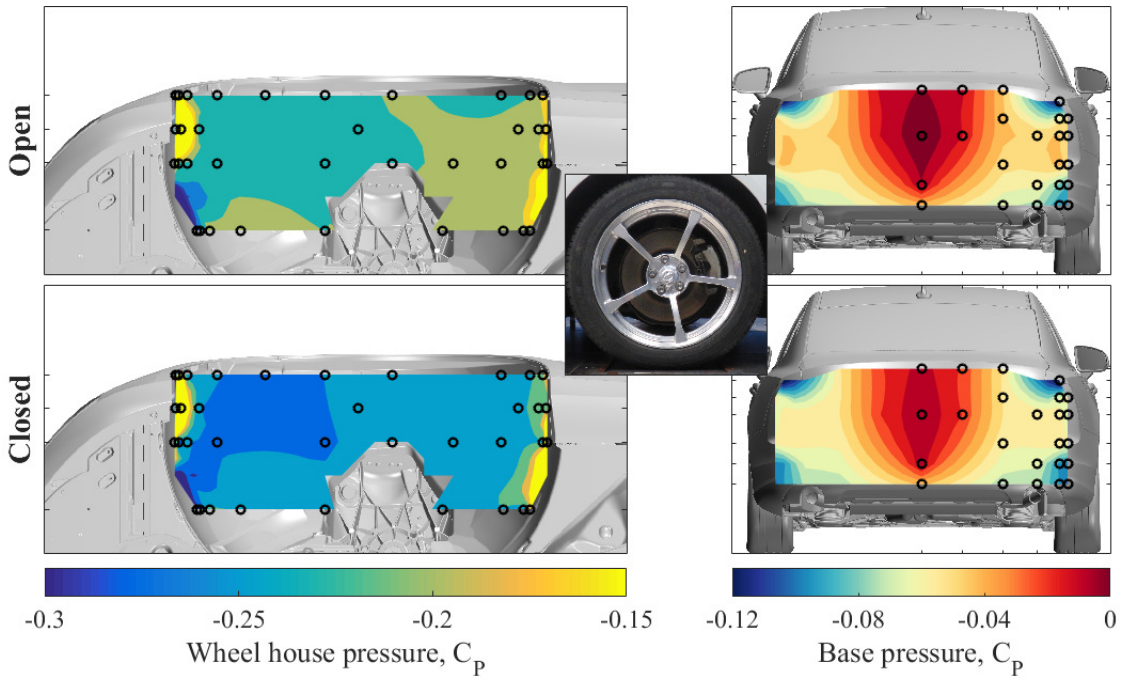

Figure 4.9: Base wheel. The wheel house and base pressure for open and closed cooling flow.

that flow from the engine bay into the wheel house gets blocked. Furthermore, it was found that using the cover plates caused a low pressure region near the wheel arch edge downstream of the front axle, see Fig. 4.8. This low pressure region was only found when having 100 % coverage area. At the lower rear part of the wheel house, a stagnation could describe the increase in pressure. Surprisingly, a similar trend can be seen at the front of the wheel house. During one of the test sessions, smoke visualisation was used to follow the flow into the front wheel house. It was found that the flow hits the tire and loops up into the front of the wheel house, which could explain that pressure rise. The wheel house and base pressure figures for all DPI configurations can be found in Appendix C.

4.1.6.2 Individual wheel parameter analysis

Some of the wheel parameters were analysed in depth using flow field measurements, as described in Section 3.1.2.3. The flow field measurements will be presented in terms of total pressure coefficient, $C_{P,tot}$, local drag and vorticity (Eq. 2.13, 2.21 and 2.22).

Once again, it is interesting to understand the effect of the fully covered wheel with the lowest drag. In Fig. 4.10, the base pressure is shown at the vehicle base, to the left. To the right, *Plane 1* is placed at the correct distance from the vehicle while the three planes further downstream are placed to the right. The X distance was measured from the front axle, meaning that *Plane 2* was 500 mm downstream of the front axle and the *Planes 4* and *3* was 500 mm upstream and downstream of the rear axle, respectively. The setup of the measured planes is shown in Section 3.1.2.3. The red arrows have the same scaling in all figures and represent the in-plane

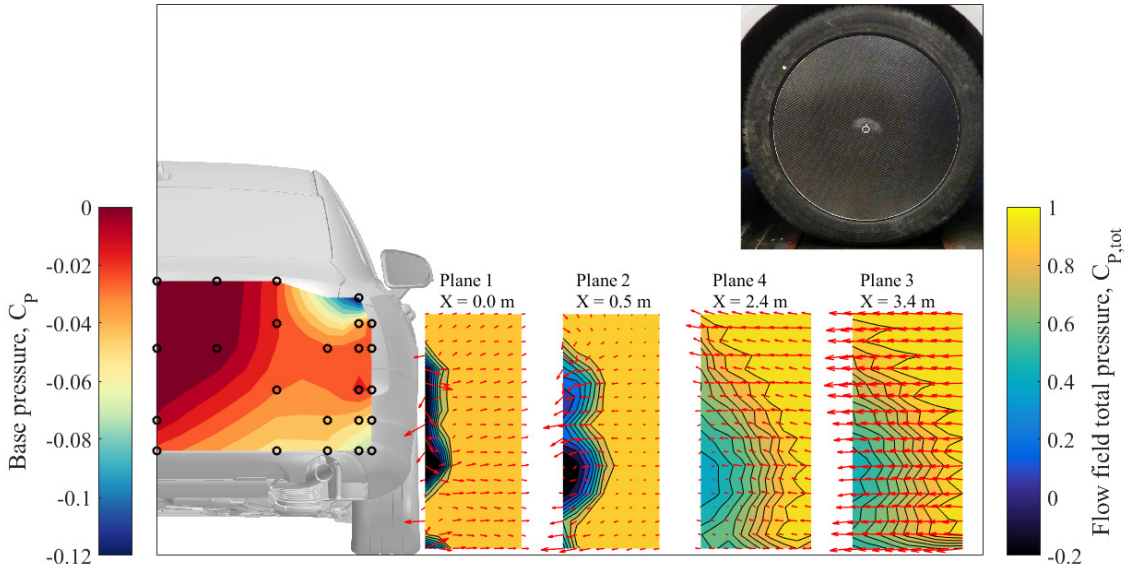

Figure 4.10: Cover plate. The flow field total pressure coefficient, $C_{P,tot}$, at the four planes along with the base pressure.

velocity vector. The colourbar for $C_{P,tot}$ used violet and black colours for values of zero or below. Hence, those colours indicate separated flow. Looking at *Plane 1* in Fig. 4.10, three regions of low total pressure can be seen. One at the ground in the region of the jetting vortex, see Section 2.1.2.2, with an expected velocity vector out from the wheel. The second region of low total pressure was located closer to the height of the wheel centre and the third uppermost region was found at the height of the wheel arch or the top of the tire. These structures were also found in *Plane 2*. Further downstream in *Plane 4* and *3*, the flow diffused into one large region

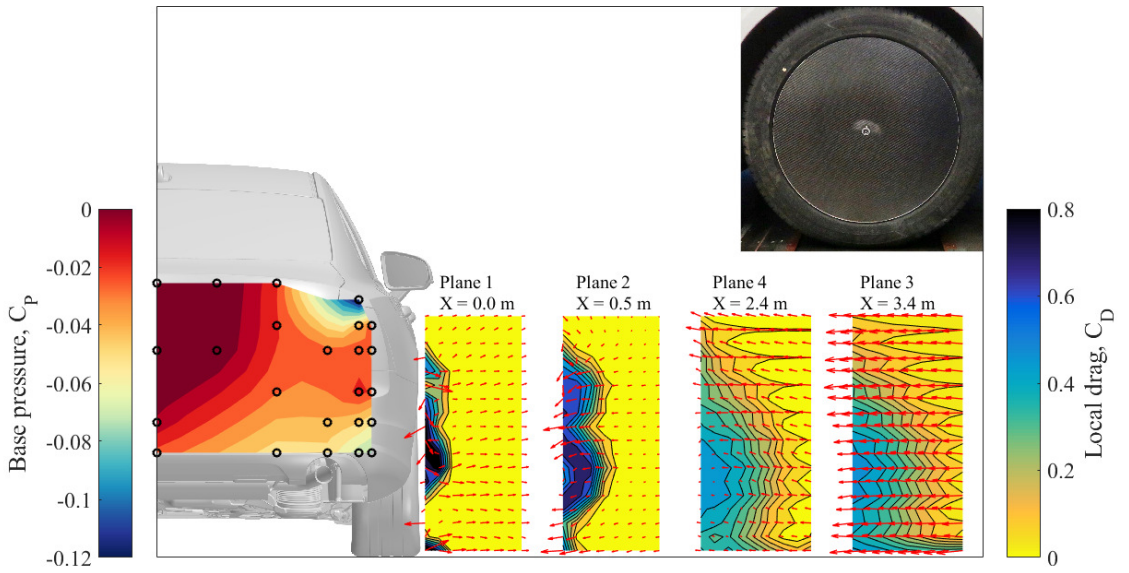

Figure 4.11: Cover plate. The local drag at the four planes along with the base pressure.

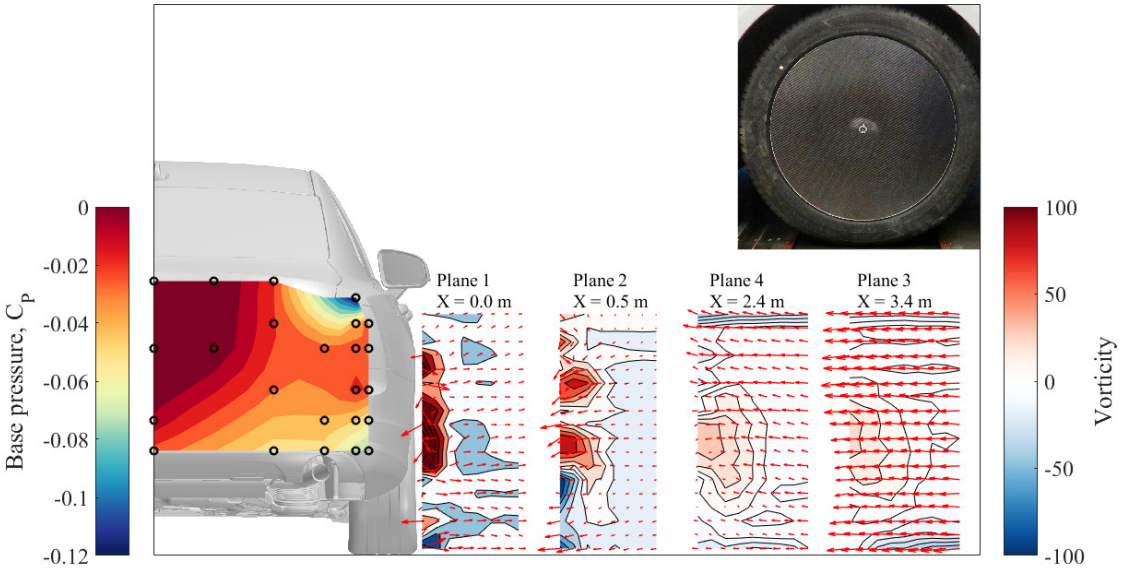

Figure 4.12: Cover plate. The vorticity at the four planes along with the base pressure.

of higher total pressure. The velocity vectors indicate that the flow near the rear wheel was angled inwards to flow behind the base. The structures found in the total pressure plots were often similar to the local drag plots, see Fig. 4.11. However, small differences can be spotted indicating that the drag was not only caused by the total pressure but also due to redirected flow.

The experimental velocity data could be used to calculate the vorticity, using Eq. 2.14. Many of the vortex structures described in Fig. 2.4 (Section 2.1.2.2) could be seen in the vorticity plots. For the covered wheel, the clockwise jetting vortex can clearly be seen at ground contact patch, see Fig 4.12. The strong centre and top vortices in *Plane 1* were still present downstream in *Plane 2* and even slightly in *Planes 4* and *3*. The vorticity, in combination with the total pressure, local drag and base pressure can give a detailed description of the flow around the wheels.

The coverage area

The coverage area was the parameter with the highest effect on the aerodynamic drag, see Fig. 4.6. Therefore, it was important to understand how the flow around the wheel changed due to this parameter. Firstly, it was evident that the base pressure was higher for D38 compared to D36 corresponding to the lower drag value, see Fig. 4.13. To explain the difference in base pressure, the wheel wake planes were used. In *Plane 1*, the jetting effect seemed to cause a greater outward flow near the ground for the open wheel (D36), see Fig. 4.13a. Also, the upper low total pressure region was more isolated from the region at the ground for D38, while the regions became combined for D36. This effect was even more evident downstream in *Plane 2*. A more open wheel allowed for flow through the wheel, as indicated by the velocity vectors in *Plane 1*. The more covered D38 wheel limited that flow. The fully covered wheel (Fig. 4.10) had three low total pressure regions near the front wheel. The structures of D38 were more similar to the covered wheel than those of

D36, as expected. This was especially obvious at the rear wheel, in *Planes 4* and *3*, where D36 had a triangular low total pressure region when both D38 and the fully covered wheel had round regions more similar to the structures upstream.

The local drag could not add any information when comparing the effect of the coverage area. The vorticity could however show great differences, see Fig. 4.14. As for the fully covered wheel, the jetting vortex induced some negative vorticity at the ground for both D36 and D38. However, another stronger clockwise vortex can be seen just on top of the jetting vortex for the open wheel, see Fig. 4.14a. In *Plane 2*, that vortex was still present along with the centre and the top vortices. The top

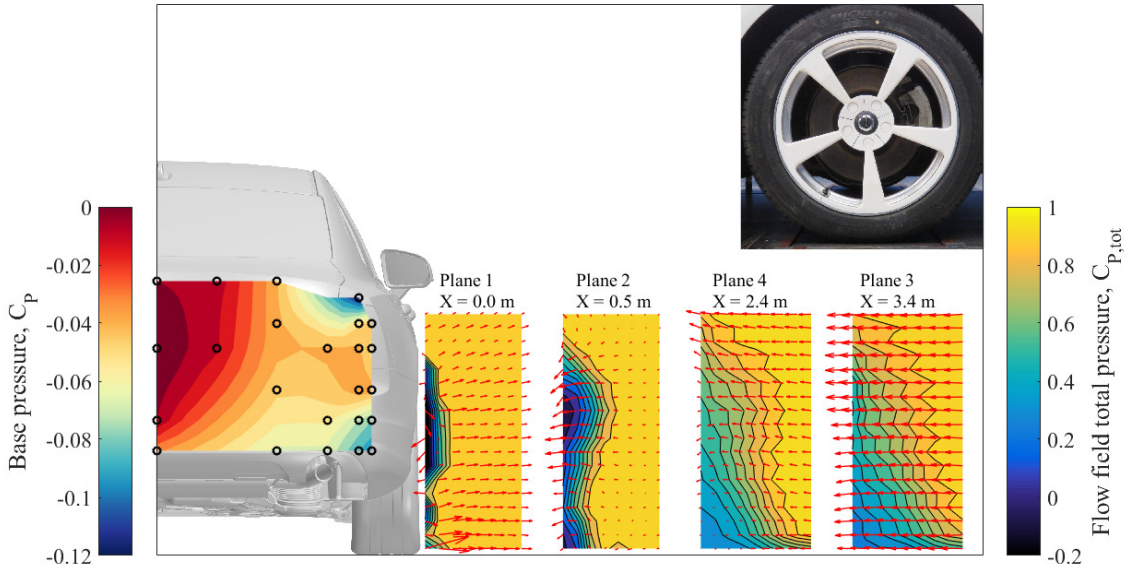

(a) D36.

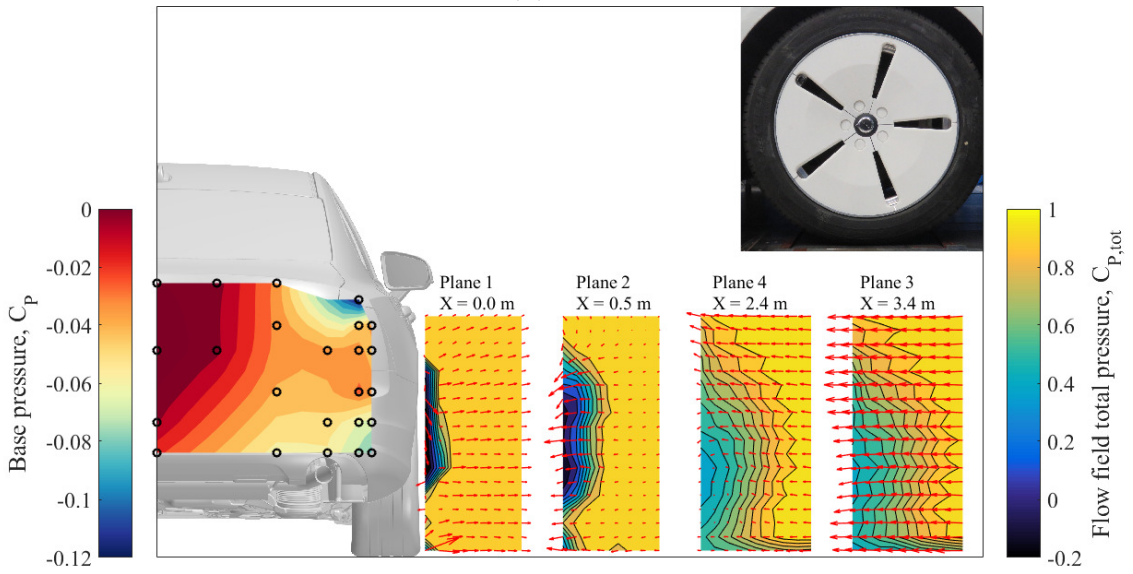

(b) D38.

Figure 4.13: Coverage area. The flow field total pressure coefficient, $C_{P,tot}$, at the four planes along with the base pressure.

vortex originated from the wheel arch and could thus be seen in all measurements, regardless of wheel configuration. The fully covered wheel had a negative vorticity at the ground in *Plane 2*, the 40 % covered D36 had a strong positive vorticity and for the 90 % covered D38 the vorticity had been cancelled out at the ground, see Fig. 4.12 and 4.14. The stronger centre and ground vorticity of the open wheel could explain the disrupted triangular wake regions at the rear. Also, vortex forming takes energy from the mean flow, causing a lower total pressure at the rear, decreasing the base pressure and thus increasing the drag. Finally, the rear wheel did not add any significant vorticity since *Plane 3* had lower vorticity than *Plane 4*.

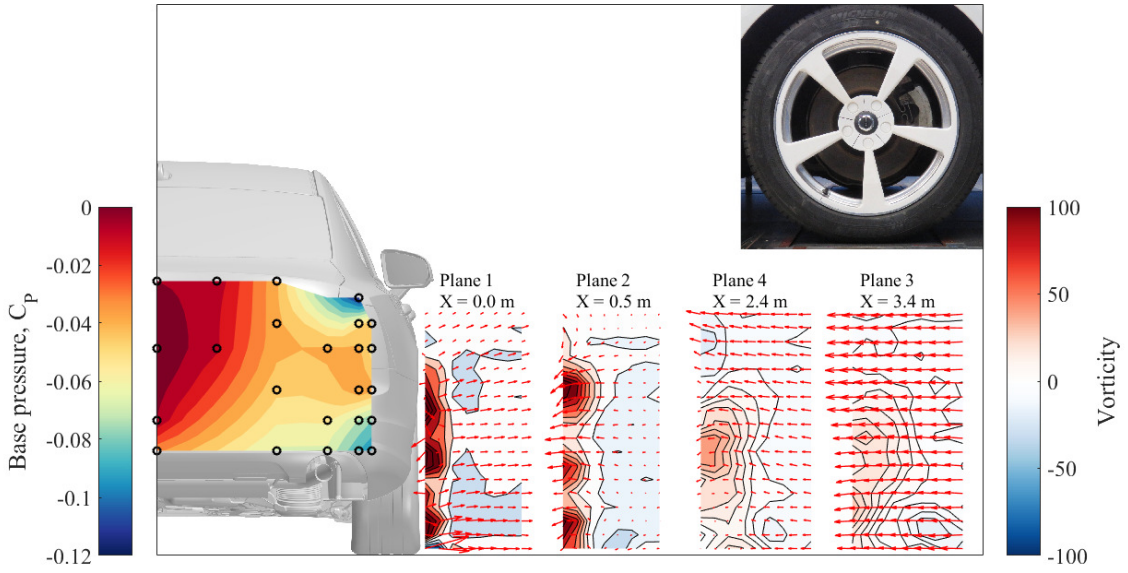

(a) D36.

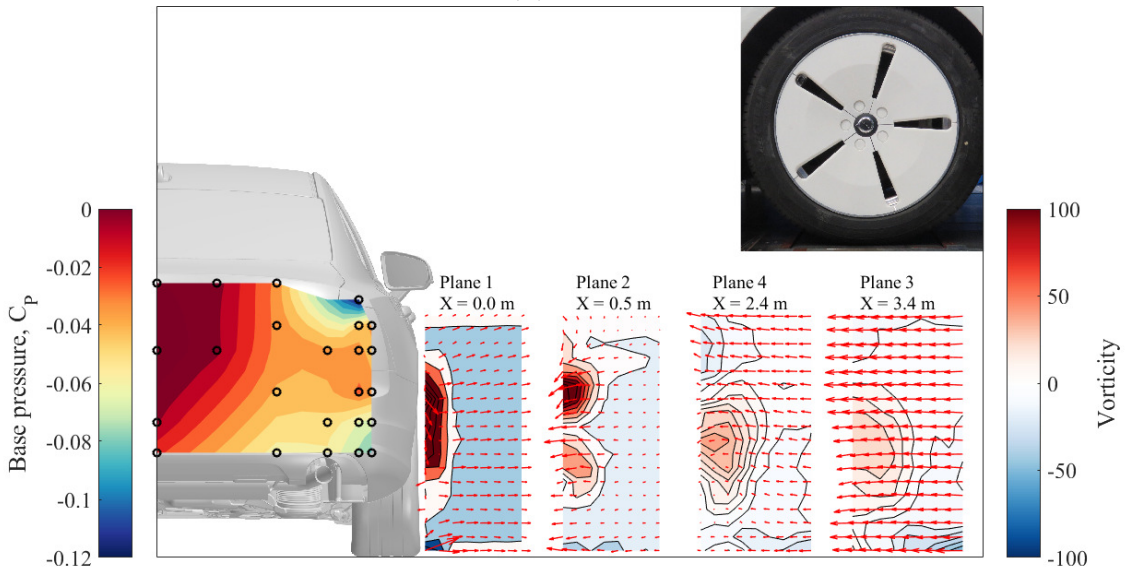

(b) D38.

Figure 4.14: Coverage area. The vorticity at the four planes along with the base pressure.

Rim cover step

The rim cover was found to be an important area of the wheel. Both the effect of angling the surface (rim cover angle) and having the surface at a depth (rim cover depth) was significant in terms of the aerodynamic drag. Geometrically, these parameters caused a step between the rim cover and the top surface of the spokes when they were set to their maximum level. Therefore, a wheel configuration with rim cover depth and rim cover angle set to the minimum levels (no step) was compared to a wheel where the parameters were set to their maximum levels (large step). The wheel D09 and D15 both had the rim cover distance set to the maximum level which

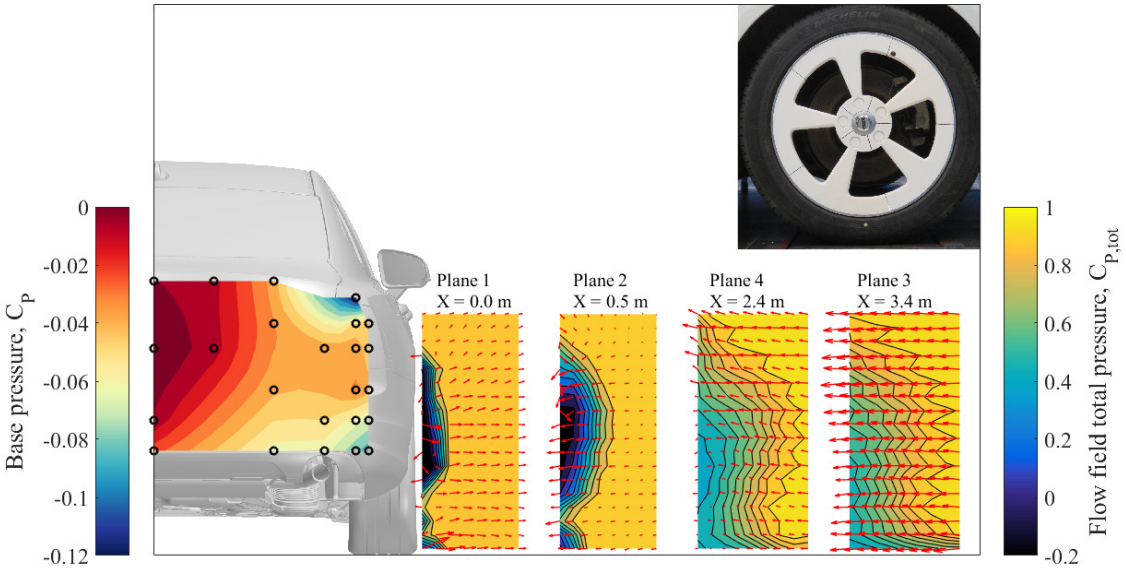

(a) D09.

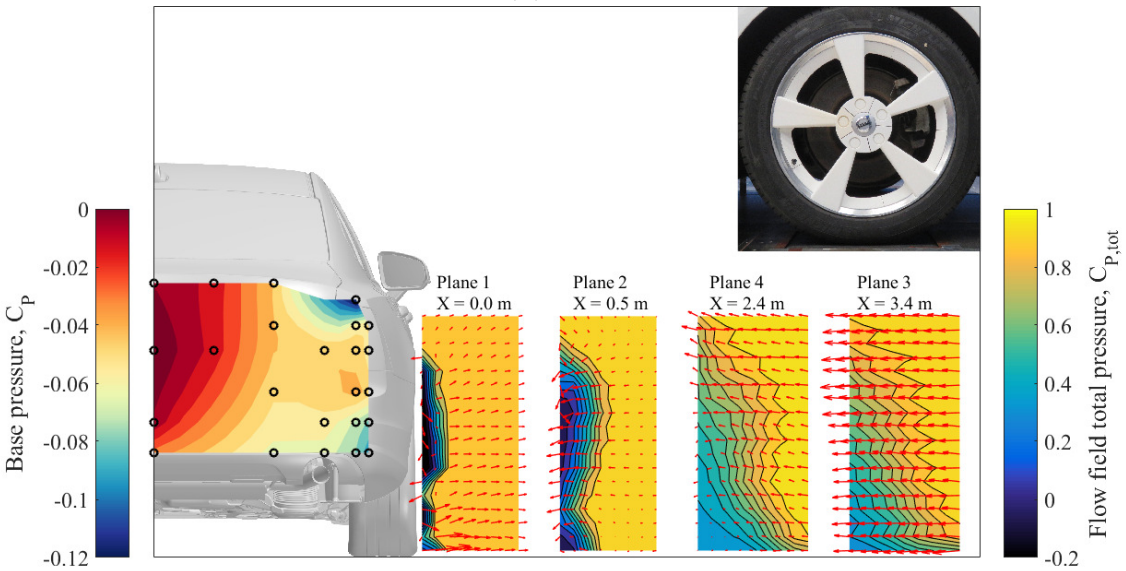

(b) D15.

Figure 4.15: Rim cover step. The flow field total pressure coefficient, $C_{P,tot}$, at the four planes along with the base pressure.

enhanced the rim cover step's effect on the flow field, see Fig. 4.15. At the base, the region of higher pressure at the centre was found to be slightly larger for the wheel without the rim cover step (D09) and the low pressure region at the bottom edges of the base extended further inwards for the wheel with the step (D15). At *Plane 2* in Fig. 4.15 it was evident that the step in D15 combined the upper and lower regions of low pressure in more extent than D09. This phenomenon could be derived upstream from *Plane 1*, where an extra low total pressure region between the jetting vortex and the upper regions could be found for D15, see Fig. 4.15b. Furthermore, the step seemed to increase the velocity out of the lower part of the

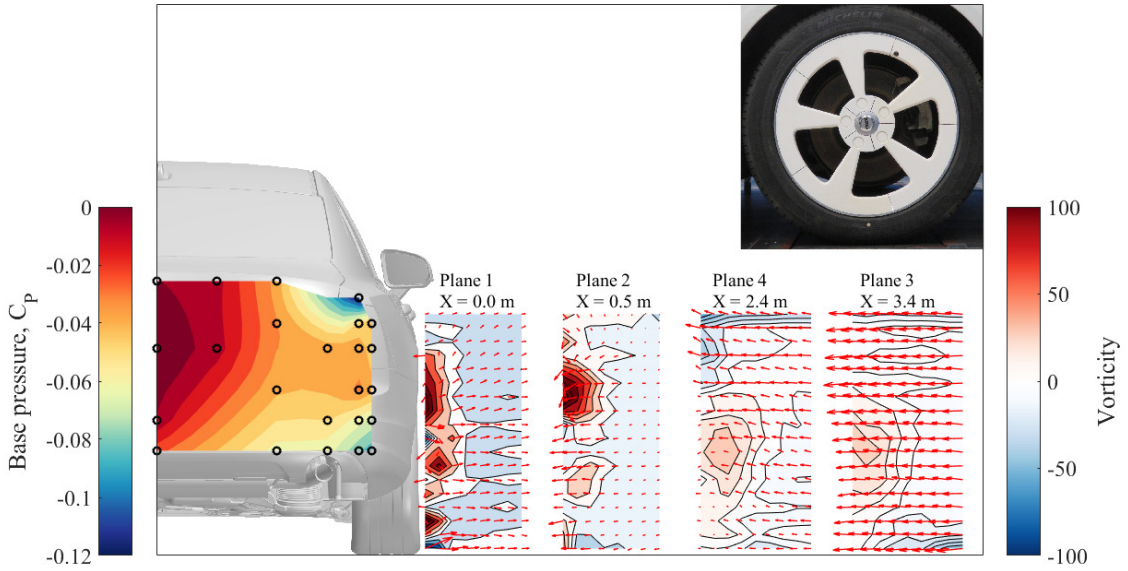

(a) D09.

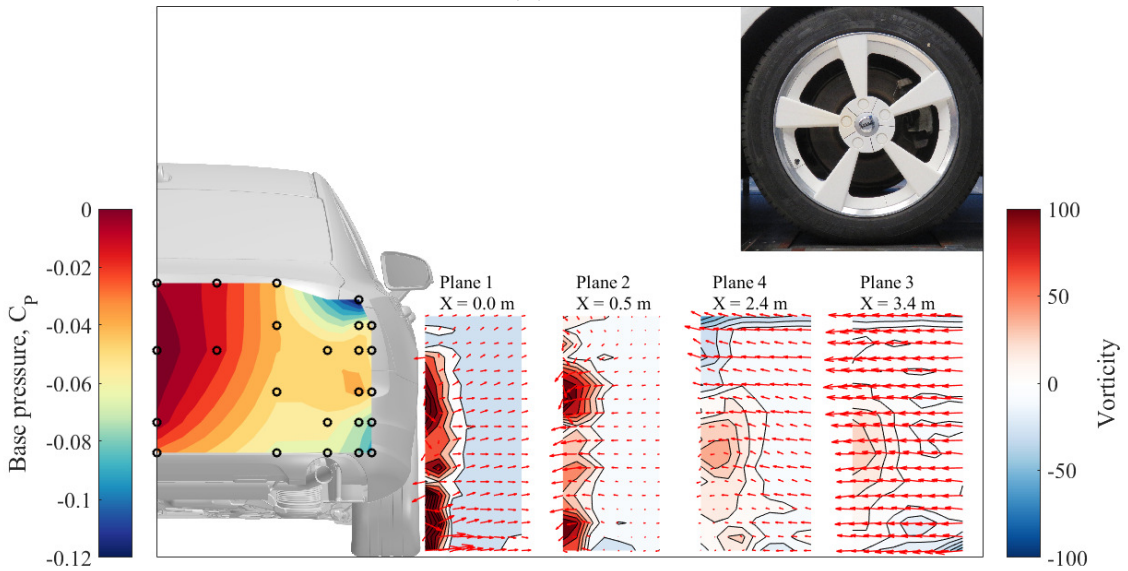

(b) D15.

Figure 4.16: Rim cover step. The vorticity at the four planes along with the base pressure.

wheel. This flow could feed the lower vortices resulting in increased vorticity in that region. Looking at the vorticity in Fig. 4.16, the theory seemed valid. The lower region near the wheel had a higher vorticity when the wheel had a rim cover step, see *Plane 1* in 4.16b. 500 mm downstream, at *Plane 2*, D15 still had a strong vortex near the ground whereas D09 had no vorticity. The fact that D09 had a negative and a positive vorticity at the ground in *Plane 1* could explain the lack of vorticity downstream in *Plane 2*. The top vortex was once again present for both wheel configurations in *Plane 2*, further proving that this feature originates from the wheel arch. When looking at the local drag, see Fig. 4.17, it could be seen (in

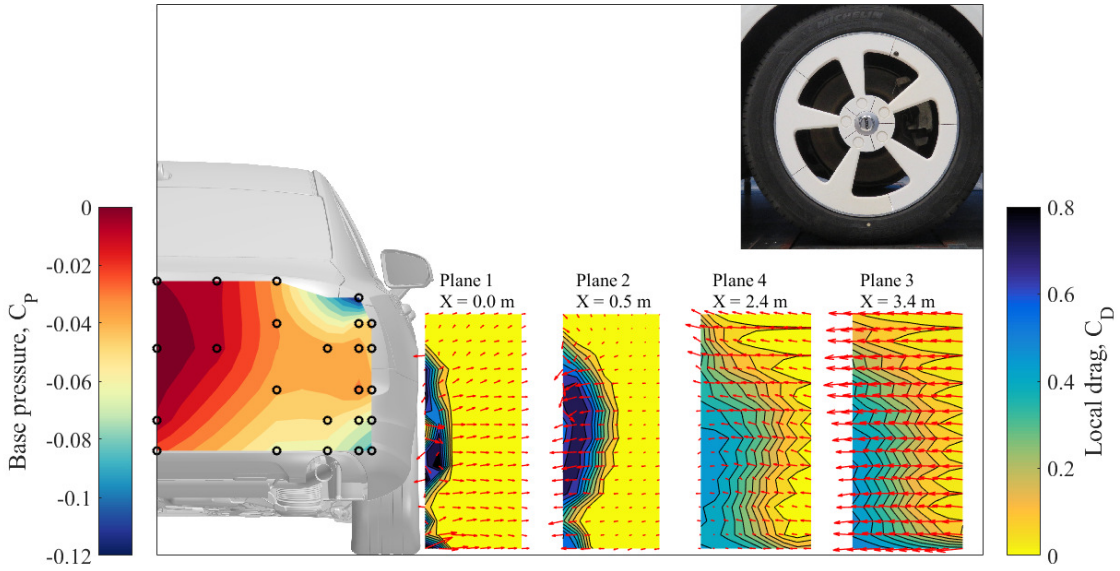

(a) D09.

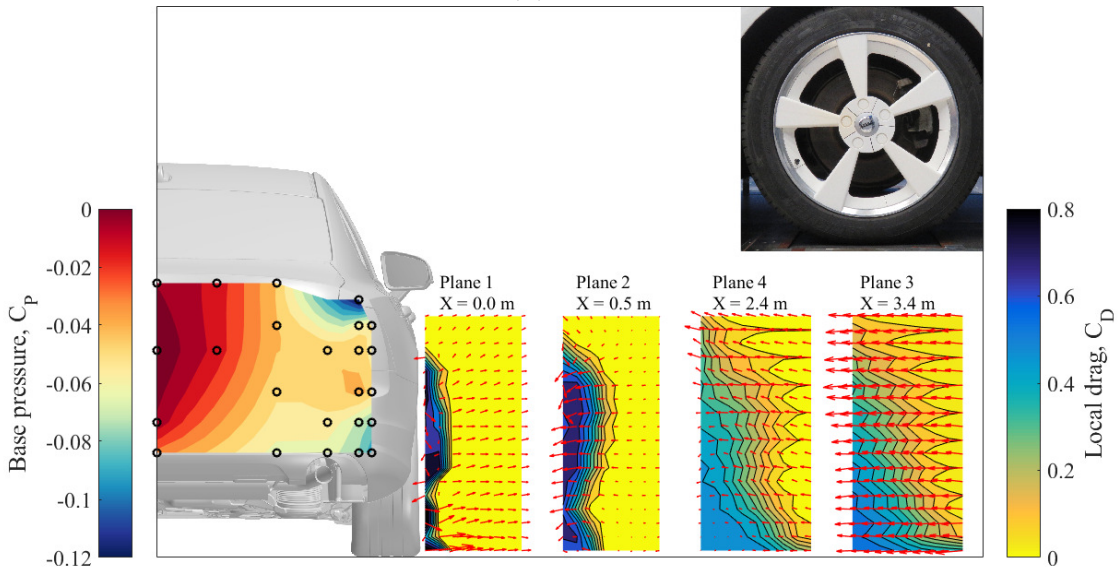

(b) D15.

Figure 4.17: Rim cover step. The local drag at the four planes along with the base pressure.

Plane 1) that having no step (D09) decreased the local drag in a small region at the top of the wheel. This effect was not visible in the total pressure. The wheel's relative velocity to the freestream is zero at the ground and double at the top of the tire. Hence, the relative velocity at the rim cover at the top of the wheel was high and could explain why this region was important. The corresponding region in Fig. 4.16a had a negative vorticity but with lower magnitude than the positive vorticity region in 4.16b, explaining the lower local drag for the wheel without the step (D09). At the rear wheel planes, it was evident that D09 has a more round region like the fully covered wheel, while D15 has the same triangular high local drag region as D36. The strong near ground vortex, found for both D15 and D36 (when an outflow through the lower part of the wheel occurred), could give one explanation to the increase in aerodynamic drag. The strong vortices disrupt the wheel wake structures making them more triangular. The forming of vortices takes energy from the mean flow, which decrease the total pressure of the flow resulting in decreased base pressure and increased drag. Furthermore, high vorticity increases the dissipation rate and more energy will be lost to heat.

Rim cover distance

Another interesting parameter was the rim cover distance. This parameter was suggested to have a high impact on the aerodynamic drag, by a previous study [33]. This thesis project did not evaluate the main effect of rim cover distance to be high, but the feature was found important in synergism with other parameters of the rim cover, see Fig. 4.6. As seen in Fig. 4.18, the differences were minimal between the two wheel configurations. It could be that the coverage area was set to the maximum level which limited the effects of the rim cover distance. Slightly larger differences could be seen in the vorticity plots, see Fig. 4.19, where the clockwise jetting vortex

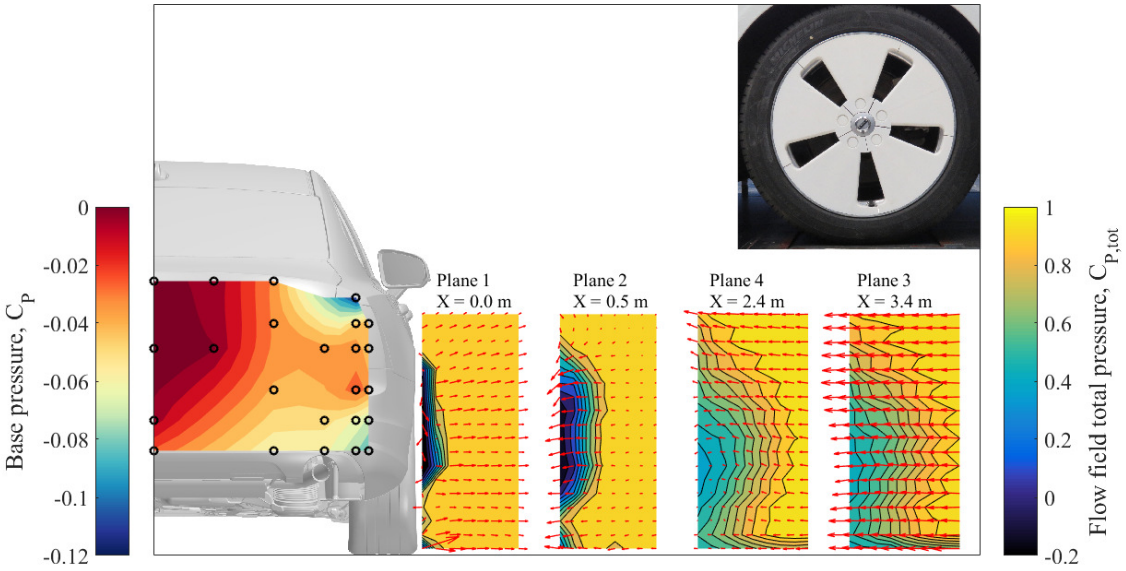

(a) D02.

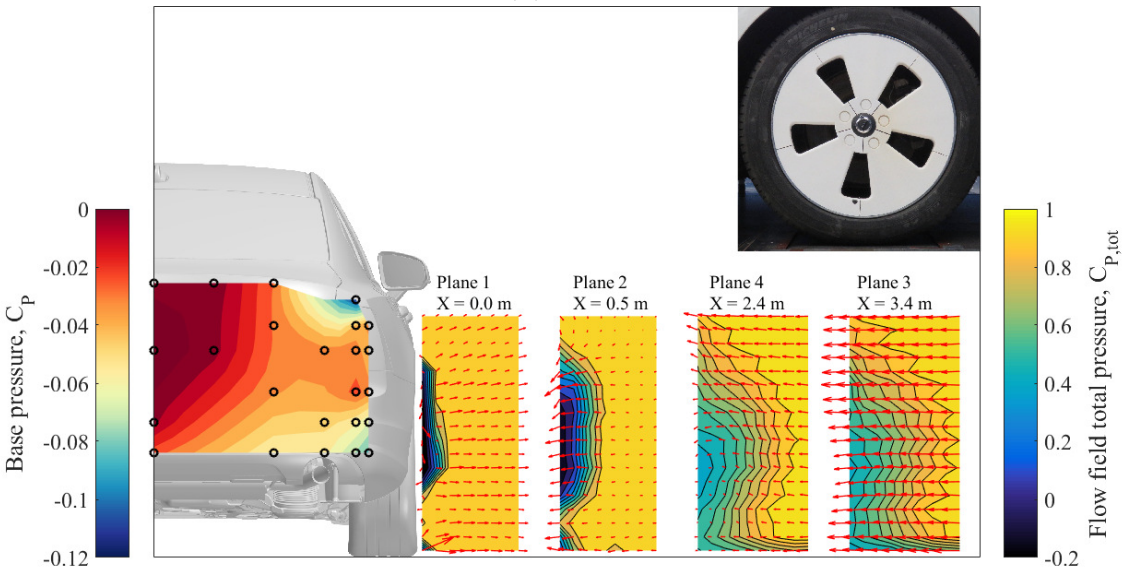

(b) D41.

Figure 4.18: Rim cover distance. The flow field total pressure coefficient, $C_{P,tot}$, at the four planes along with the base pressure.

was stronger for the wheel with a higher rim cover distance (D41). That agreed well with the findings for the rim cover step, where no step also increased the negative vorticity at the ground in *Plane 1*. Otherwise, no more conclusions were made from this analysis. The local drag did not add any information.

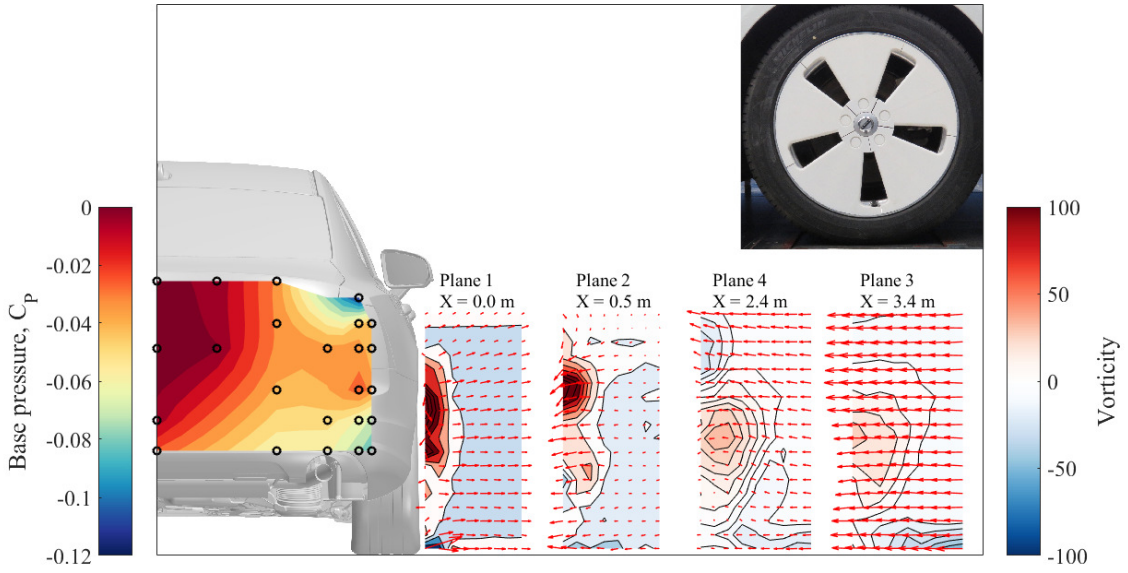

(a) D02.

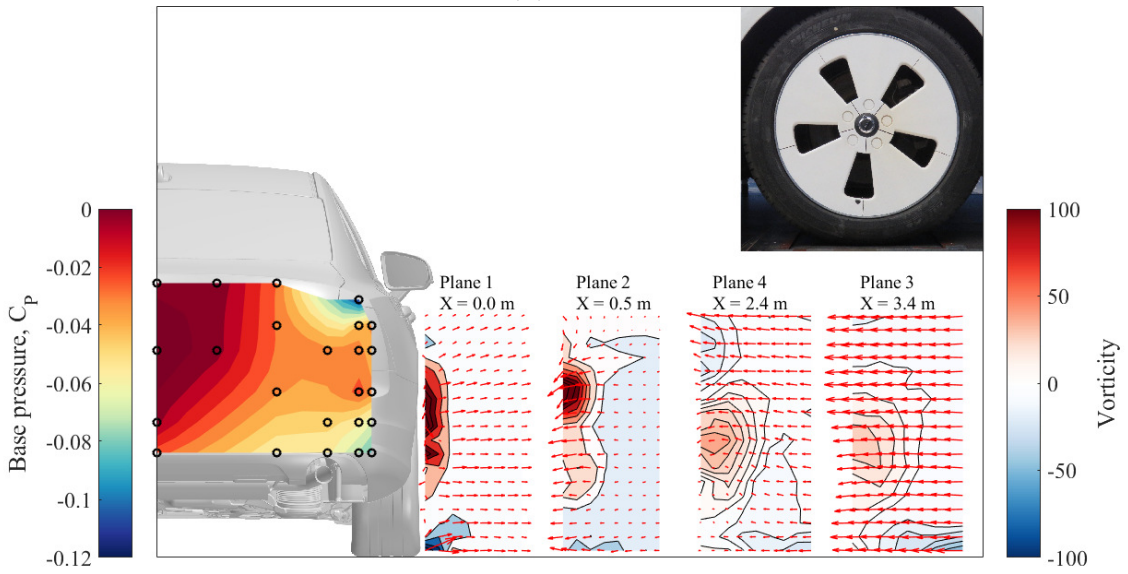

(b) D41.

Figure 4.19: Rim cover distance. The vorticity at the four planes along with the base pressure.

4.2 Numerical analysis

The numerical analysis was done to evaluate how well the CFD method could analyse wheel aerodynamics and if so, to give more insight into the flow features around the wheels. This was first done by validating the model in terms of the aerodynamic drag coefficient, C_D, and also by comparing the total pressure coefficient, $C_{P,tot}$, in the four wake planes with the same sampling grid as the flow field experiments. Once again, the coverage area (D36 and D38) was analysed in the numerical investigation since it was found to be the most important parameter.

4.2.1 Verifying the numerical solution

An important evaluation of the numerical solution was to analyse how well it could predict the measured aerodynamic drag. Therefore, the average C_D value for the CFD results was compared to the experimental measurements, see Table 4.5. No significant difference in the numerical solution's ability to predict the aerodynamic drag was found between open and closed cooling flow. It was evident that the CFD solution was fairly close to the experimental results, but far from as accurate as the wind tunnel itself. The 90 % covered wheel (D38) had a larger error compared to the 40 % covered wheel (D36). However, when analysing the trends of the coverage area, by comparing the difference between D36 and D38, it was evident that the CFD solution became more accurate.

To further validate the numerical solution, the wake planes for closed cooling flow were compared to the experimental data. The more open wheel (D36) was first evaluated, see Fig. 4.20. At *Plane 1*, the three low total pressure zones seen in the wind tunnel experiments were found in the CFD solution as well. Even though the small low total pressure zone above the jetting vortex region was slightly smaller in the CFD solution. Also, the region of low total pressure seemed to extend further up towards the wheel arch, in the experimental data, see Fig. 4.20b. Further downstream, in *Plane 2*, one would expect a larger upper low total pressure zone for the numerical solution, otherwise the shape of the low total pressure zone was similar to the experimental data. At both *Planes 4* and *3*, the numerical solution seemed to predict the total pressure correctly.

However, when looking at the rear for the more covered wheel (D38) it was evident that the same triangular shape could be seen in the CFD solution, see *Plane 4* and *3* in Fig. 4.21. The experimental data showed a more round region of lower total pressure, more similar to the structures upstream. However, the CFD solution presented structures closer to the experimental data upstream at the front wheel. At *Plane 1*, the gap between the low total pressure zone corresponding to the jetting vortex and the upper zones was clearly visible. Likewise, the low total pressure structure at *Plane 2* for the numerical solution resembles the experimental data well, even though the total pressure zone seemed to be too high near the vehicle.

To further validate the CFD solution, the vorticity of the experimental and numerical data were compared. Fig. 4.22 and 4.23 present the vorticity for configuration D38 and D36. The vorticity based on numerical data of the 90 % covered wheel (D38) can be seen in Fig. 4.22a. In *Plane 1*, the CFD solution captures the same upper vortex,

Table 4.5: The CFD's ability to predict the aerodynamic drag, C_D, for open and closed cooling flow. The experimental measurements (Exp.) was set as reference.

	D36		D38		D36 - D38	
	Exp.	**CFD**	**Exp.**	**CFD**	**Exp.**	**CFD**
$\boldsymbol{\Delta C_D}$ (Open)	Ref.	-0.004	Ref.	-0.006	Ref.	0.002
$\boldsymbol{\Delta C_D}$ (Closed)	Ref.	-0.004	Ref.	-0.007	Ref.	0.003

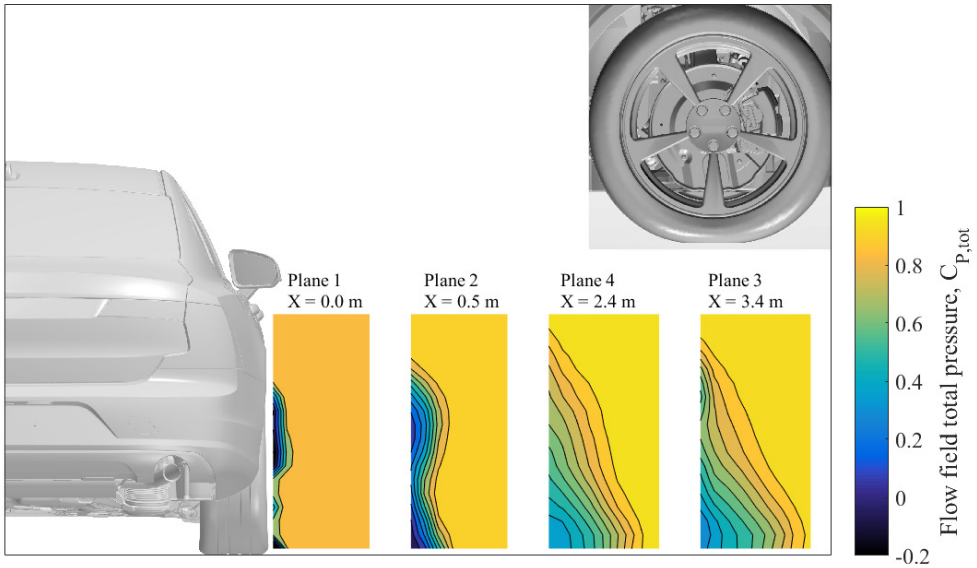

(a) CFD solution.

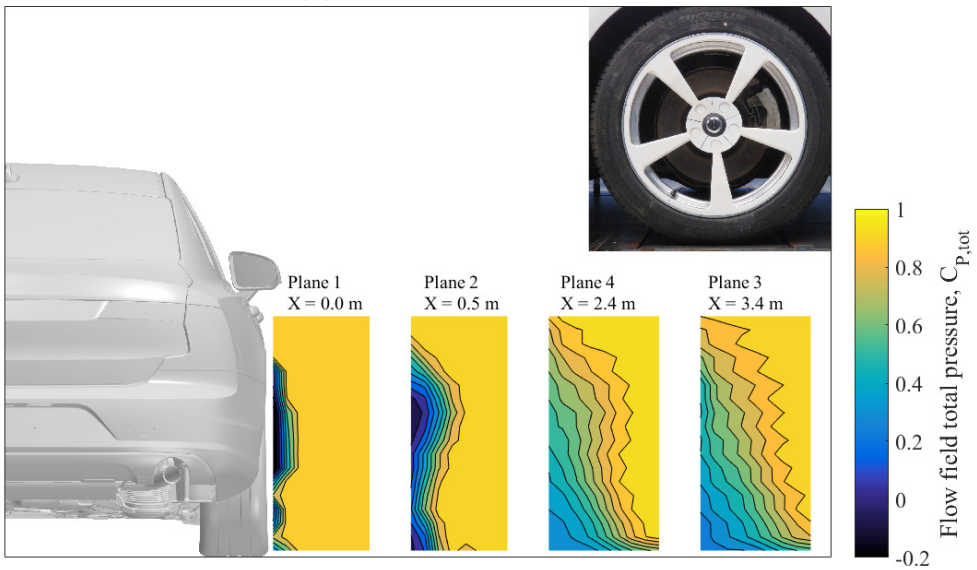

(b) Wind tunnel experiments.

Figure 4.20: The 40 % covered wheel (D36), comparing the numerical CFD solution to the experimental data in terms of total pressure coefficient, $C_{P,tot}$.

stretching from the top of the wheel house to the wheel centre. In addition, it also captures the clockwise jetting vortex at the ground. Further downstream in *Plane 2*, the CFD underpredicts the magnitude of the upper vortex and shows vorticity at the ground, which could not be seen in the experimental data, see Fig. 4.22b. This could be a result of inaccurate modelling of the rotating wheels. The tire geometries used in the CFD does only include longitudinal grooves and not any lateral, which could explain the inaccuracy of the vorticity field. When comparing *Planes 4* and *3*, the CFD solution once again overpredicts the near ground vorticity and seemes to predict the mid-plane vortex structures closer to ground when comparing to the

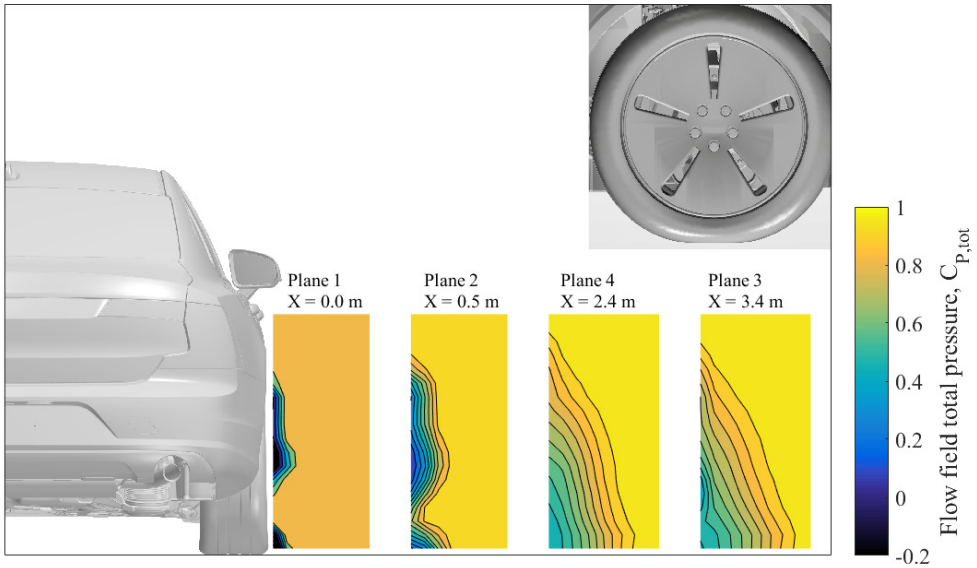

(a) CFD solution.

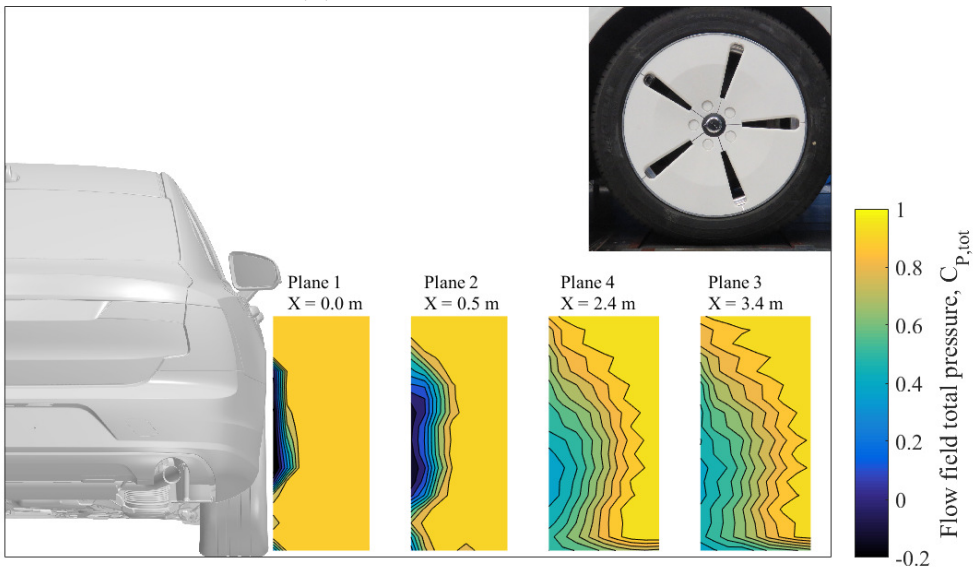

(b) Wind tunnel experiments.

Figure 4.21: The 90 % covered wheel (D38), comparing the numerical CFD solution to the experimental data in terms of total pressure coefficient, $C_{P,tot}$.

experimental data. Hence, the CFD solution could more accurately predict the vorticity at the front wheel than at the rear.

The vorticity based on the numerical data of the 40 % covered wheel (D36) can be seen in Fig. 4.23a. It is evident that the vorticity predicted by the CFD solution captures the same trends as the experimental data in *Planes 1* and *2*. At the front axle, in *Plane 1*, a positive vortex at the wheel centre and one near the ground along with a small negative vorticity at the ground can be seen for both the numerical and experimental data. The three distinguished vortices further downstream in *Plane 2*

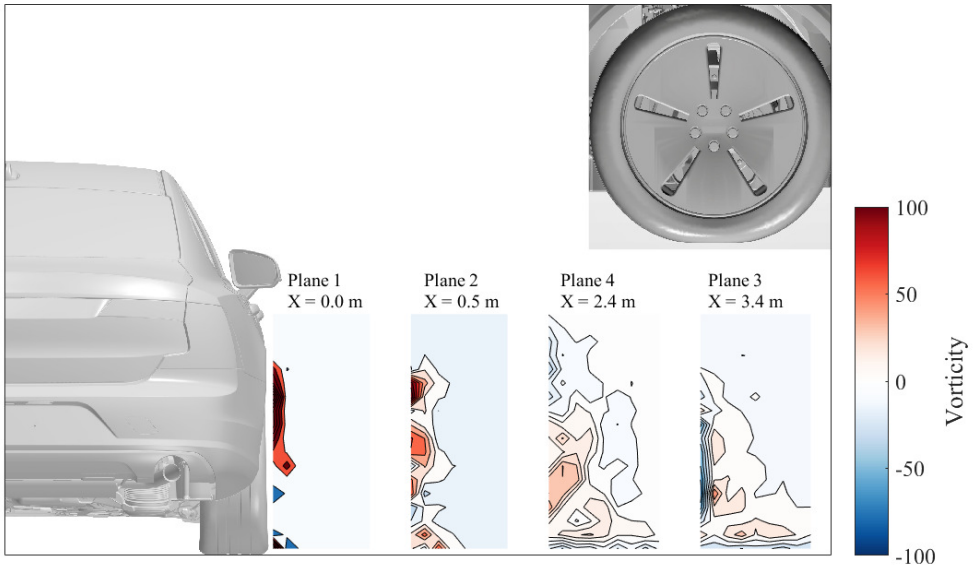

(a) CFD solution.

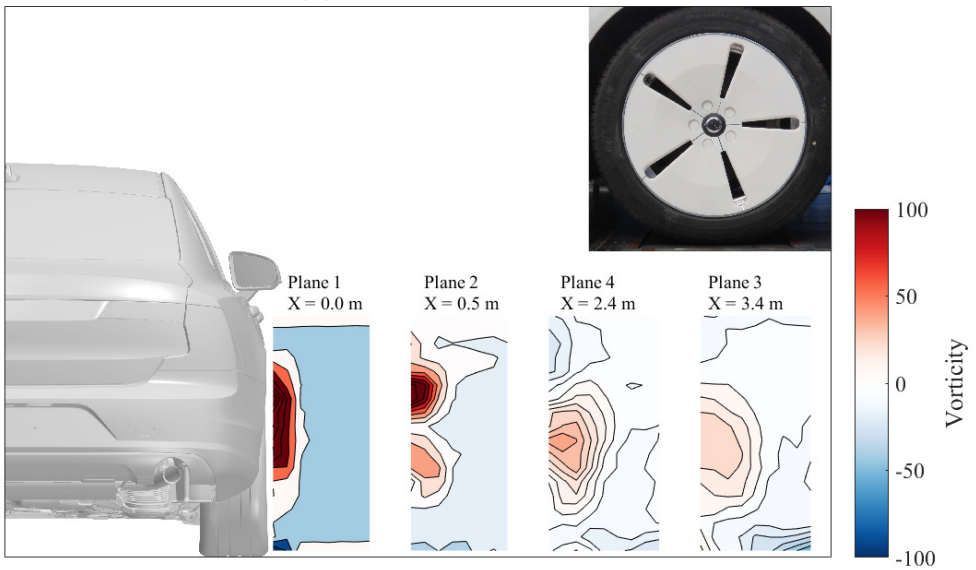

(b) Wind tunnel experiments.

Figure 4.22: The 90 % covered wheel (D38), comparing the numerical CFD solution to the experimental data in terms of vorticity.

of the experimental data (Fig. 4.23b) can also be seen in the CFD solution. At the rear wheel, in *Plane 4* and *3*, the vorticity from the CFD solution does not resemble the experimental vortex structures and seemed to be placed too near the ground, as for the 90 % covered wheel.

In summary, the C_D trends could be predicted well using the CFD method, but could not predict the absolute aerodynamic drag values with the same accuracy. The CFD solution could predict the flow field fairly well at the front wheel, but not consistently well further downstream. Therefore, the CFD solution was considered valid at the front wheel, but no further analysis at the rear could be done.

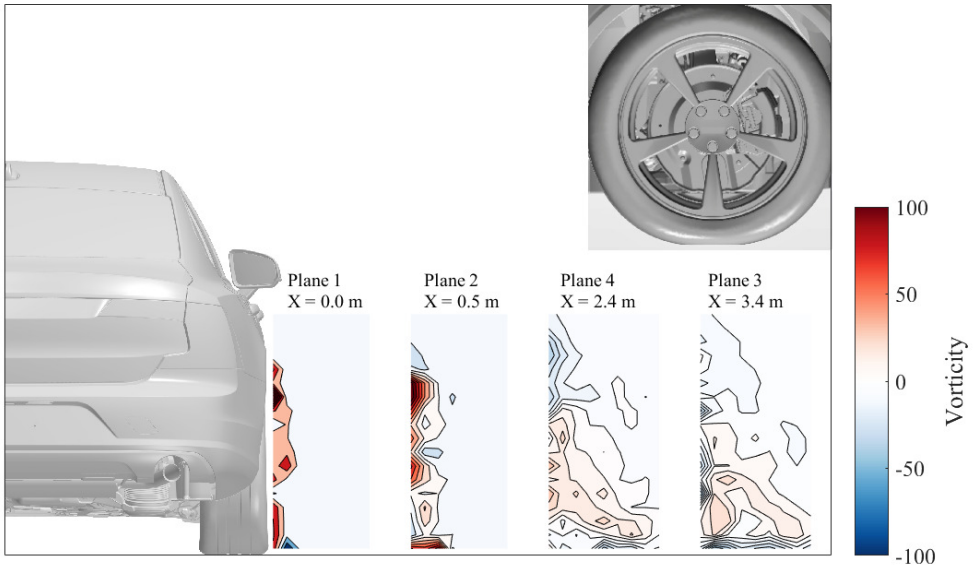

(a) CFD solution.

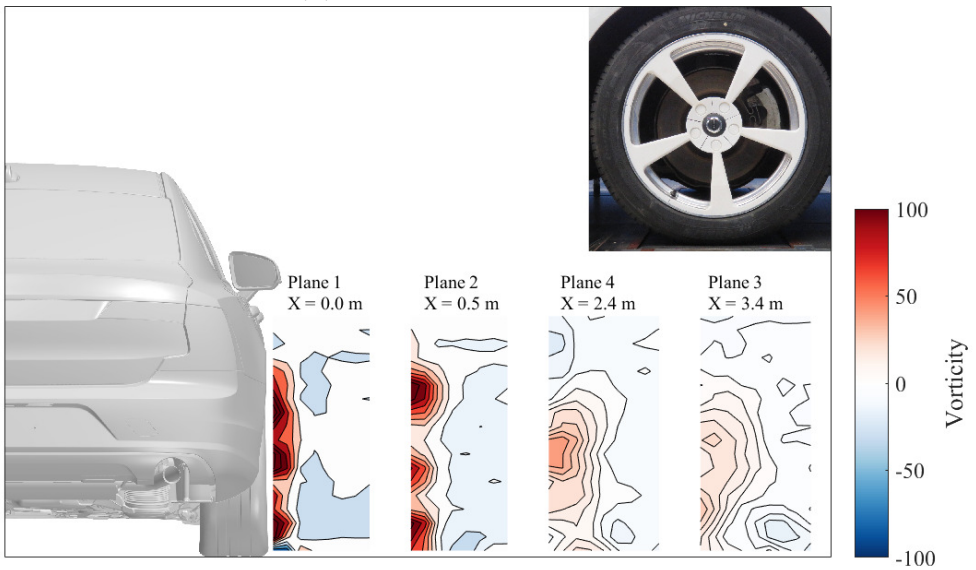

(b) Wind tunnel experiments.

Figure 4.23: The 40 % covered wheel (D36), comparing the numerical CFD solution to the experimental data in terms of vorticity.

4.2.2 Additional numerical analysis

It was interesting to analyse the total pressure of the four planes for open cooling flow, since the experimental flow field measurements were only performed with closed cooling flow. Furthermore, the CFD solution could be used to analyse the in and out flow of the wheel and wheel house and the corresponding vortex structures.

The numerical total pressure data for open cooling flow can be seen in Fig. 4.24. It was evident that open cooling flow decreased the total pressure near the vehicle in *Planes 1* and *2*, indicating more separated flow around the front wheel for both

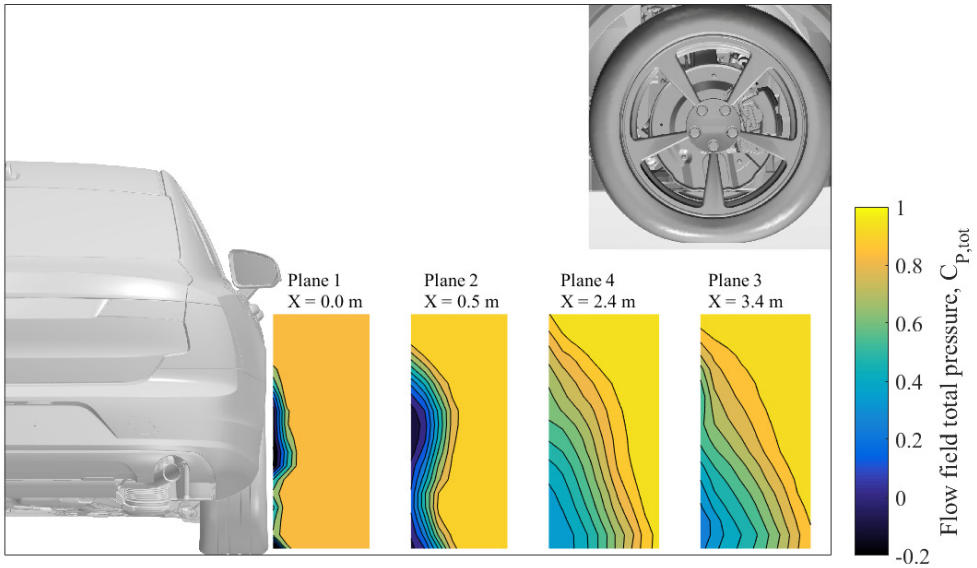

(a) D36.

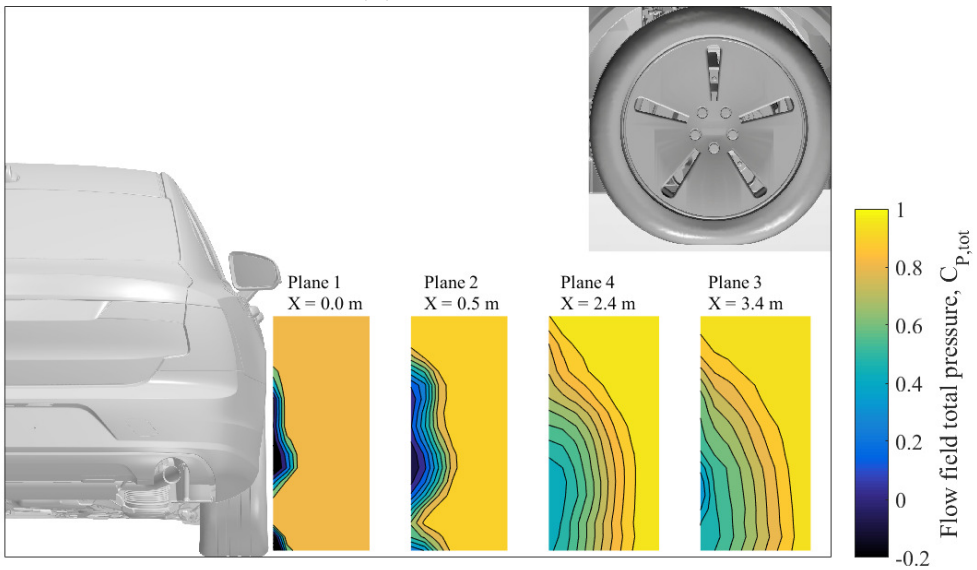

(b) D38.

Figure 4.24: Numerical CFD solution of the open (D36) and the more covered (D38) wheel configurations for open cooling flow.

wheel configurations, compared to the closed cooling setting in Fig. 4.20a and 4.21a. Otherwise, the low $C_{P,tot}$ region shapes were similar.

To fully understand the flow around the wheels, it was useful to visualise the flow in and out of the wheels and wheel housings, see Fig. 4.25. Upstream of the front wheel, the flow was clearly moving in the positive Y direction, due to the shape of the front bumper. More interesting to note was the flow out of the lower part of the open wheel, where no outflow could be seen in the same area for the more closed wheel. This agreed well with the experimental data indications found in Fig. 4.13a and 4.15b and the theory that this flow will feed the near ground vortex, resulting in higher drag. This flow, from the wheel house and out through the wheel, was thus blocked by the more covered wheel. Therefore, it was interesting to note that the more covered wheel had a much higher outflow at the wheel arch downstream of the front axle. That was the same area where a low pressure zone was found inside the wheel house when fully covering the wheels but not otherwise. Finally, it was observed that the open wheel had a higher inflow behind the wheel, near the ground.

Similarly, the vertical velocity components can be compared between the two wheels, see Fig. 4.26. The flow that hit the lower part of the tire seemed to be redirected upwards. The same trend could be seen at the upper part of the tire as well, but not with the same magnitude. The most visible difference in vertical velocity

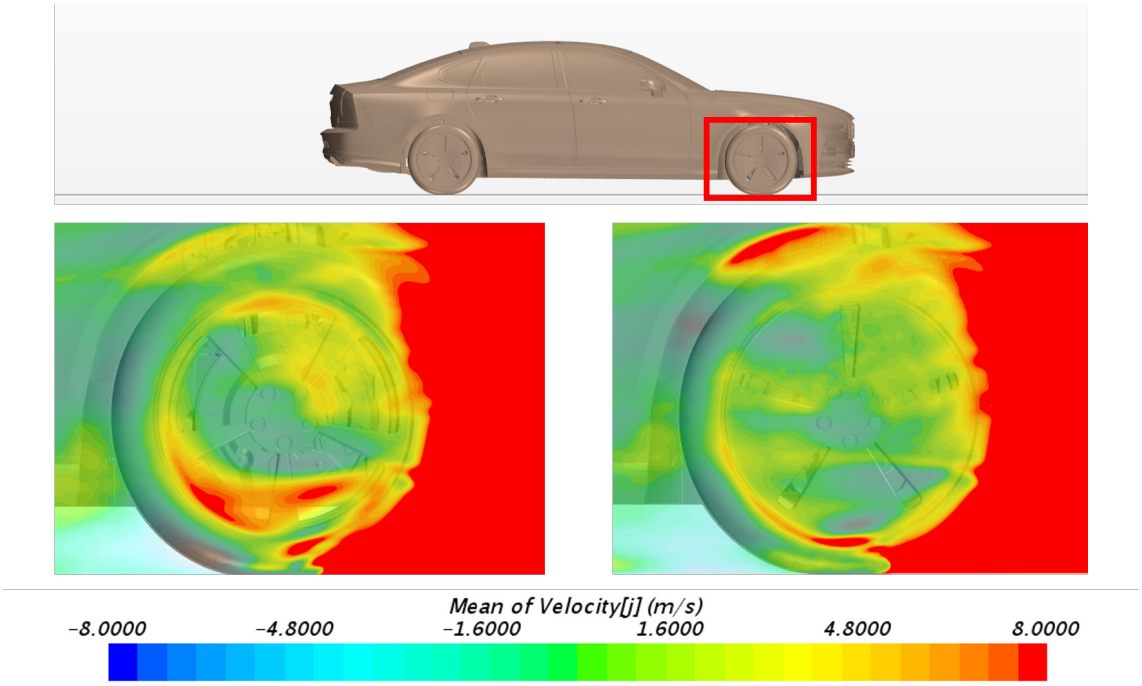

Figure 4.25: The numerical mean Y velocity. Red indicates flow out of the wheel and blue flow in to the wheel, with some transparency to visualise the corresponding wheel location. The 40 % covered D36 (left) compared to the 90 % covered D38 (right) for closed cooling flow. The plane on which the Y velocity is plotted has a distance of 10 mm from the vehicle.

between the two configurations could be seen at the part of the wheel furthest to the rear, where the open wheel generated higher upward flow. This redirected flow will increase the local drag in that region.

To further compare the flow differences between the two wheels, the vorticity in the X direction for each wheel was plotted on a plane along the vehicle, see Fig. 4.27. Both wheels have two vortex structures at the top of the wheel house. The upper vortex is originating from the outer part of the wheel house surface and is thus similar for both wheels. The lower of the two vortices did however differ between the open (D36) and the more closed (D38) wheels. This vortex seemed to originate from the same position as the outflow seen in Fig. 4.25, and could thus explain why this vortex was found to be stronger and longer lasting for the more closed wheel (D38), which had a higher outflow. For the fully covered wheel, this was also the region where a low pressure was found inside the wheel house near the wheel arch edge, see Fig. 4.8.

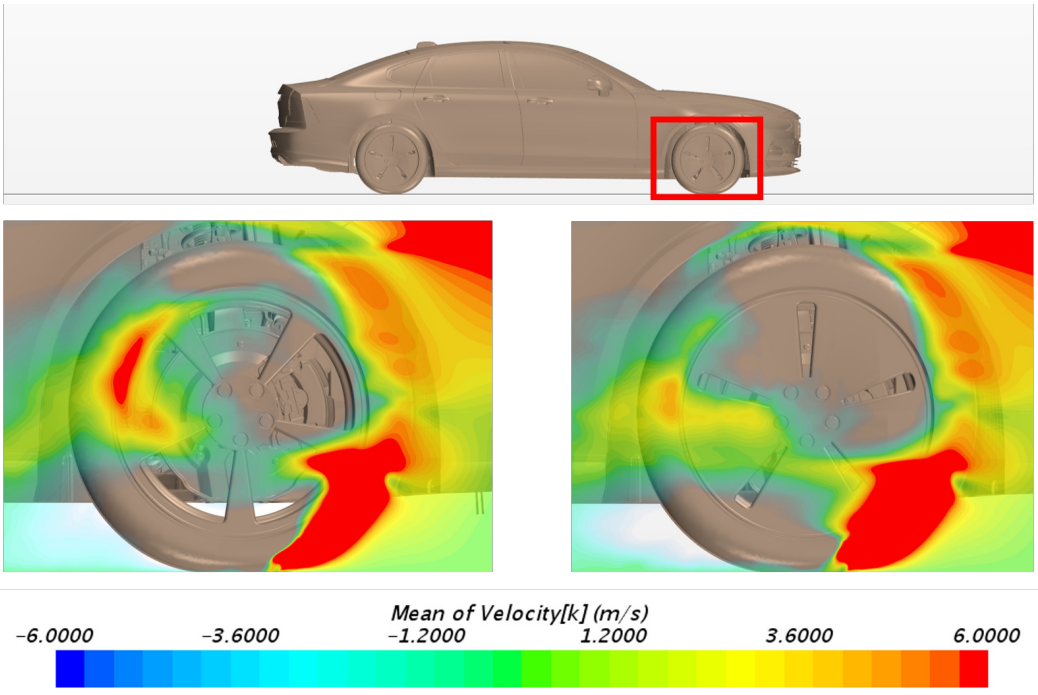

Figure 4.26: The numerical mean Z velocity. Red indicates upwards flow and blue downwards, with some transparency to visualise the corresponding wheel location. The 40 % covered D36 (left) compared to the 90 % covered D38 (right) for closed cooling flow. The plane on which the Z velocity is plotted has a distance of 10 mm from the vehicle.

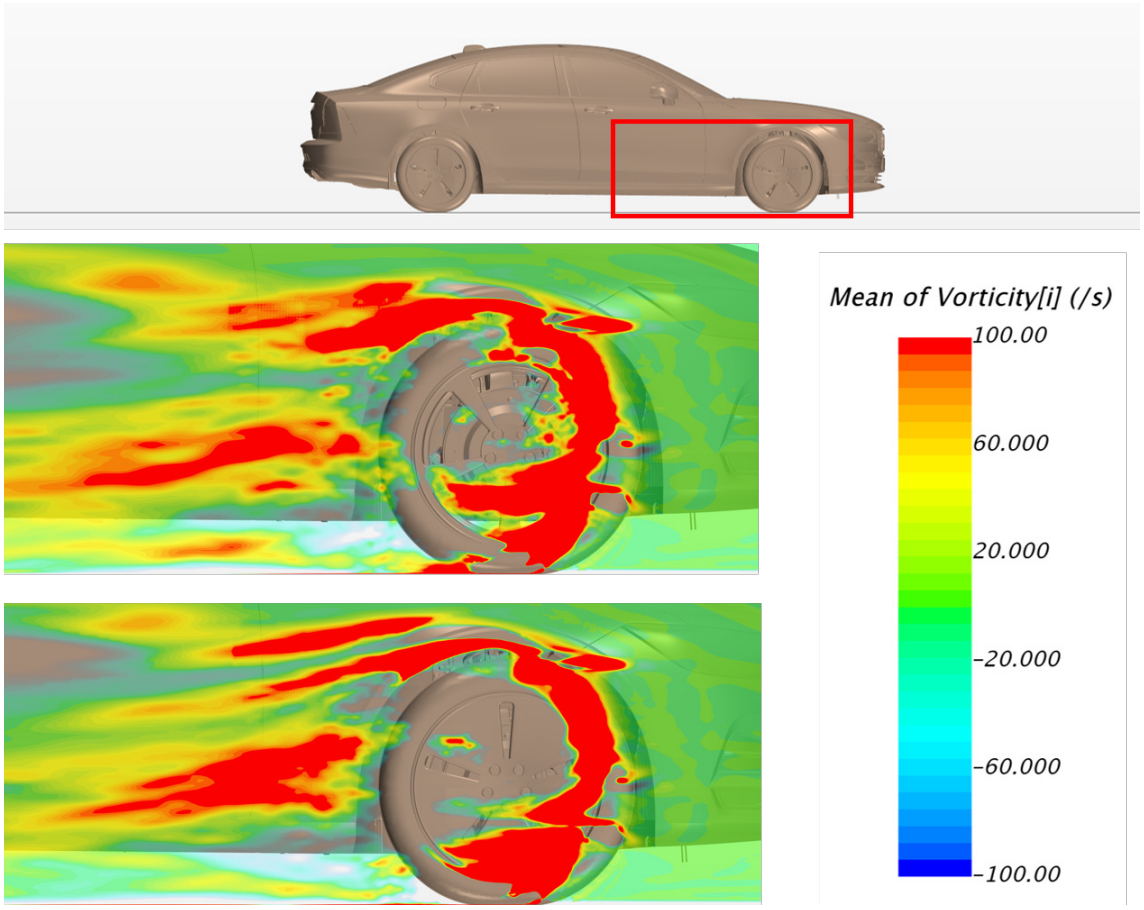

Figure 4.27: The numerical mean vorticity in X direction. Positive vorticity is visualised in solid red and negative in transparent blue. The 40% covered D36 (upper) compared to the 90 % covered D38 (lower) for closed cooling flow. The plane on which the vorticity is plotted has a distance of 10 mm from the vehicle.

5 Conclusions

This thesis further developed a modular wheel concept which could be used to cost- and time-efficiently investigate many wheel configurations in the wind tunnel. The concept was used, in combination with statistical design of experiment (DOE) methods, to evaluate the aerodynamic drag effect of 14 wheel parameters. Furthermore, the thesis also used flow field and surface pressure measurements to aerodynamically explain how the parameters affected the flow around the wheels. The thesis also utilised CFD simulations, where a sliding mesh setup at the wheels was adopted to accurately simulate wheel rotation.

The work showed that it is possible to evaluate wheel geometries in terms of aerodynamic drag, using the modular wheel concept. This allowed for the wheel configurations to be changed rapidly during the wind tunnel sessions without altering other tire or wheel properties. The work also proved that it is possible to use statistical methods to evaluate the individual wheel parameters main and synergy effects on the drag.

From the separate studies, it was concluded that the most important wheel parameter, the coverage area, has a linear effect on the aerodynamic drag. Furthermore, it was found that neither the rim track design nor the asymmetric rim cover had a significant impact on the aerodynamic drag. The rim track design was evaluated with the same projected coverage area for all three profiles, to only evaluate the shape of the rim track. Therefore, two standard wheels with different rim track design could still perform differently, if for example one of the rim tracks has a larger coverage. The asymmetric rim cover was found to be insignificant. However, this thesis cannot conclude that all types of asymmetric wheels also have an insignificant effect of the aerodynamic drag.

Using the statistical tools, it was found that the same aerodynamic trends could be seen regardless of an open or closed cooling flow. This led to a combined regression model using an offset value when switching between open and closed cooling flow. The six critical wheel parameters used in the regression model are listed below, with their parameter numbers and geometrical levels to decrease the aerodynamic drag:

- No. 1: Coverage area (High)
- No. 2: Rim cover distance (High)
- No. 3: Rim cover depth (Low)
- No. 4: Rim cover angle (Low)
- No. 6: Depth of centre (Low)
- No. 7: Drop angle (High)

In conclusion, the regression model advocates a covered wheel with the cover surfaces placed far out radially and flush to the tire wall (bead), making a wheel flat.

Similarly, this work proved that the same trends were found when changing vehicle type, from a sedan to an estate car. However, it was also found that the importance of the coverage area differed between the models. The coverage area parameter was less important for the estate vehicle compared to the sedan.

Surface pressure measurements on the base of the vehicle could show a correlation between the aerodynamic performance of the wheels and the pressure distribution. It also provided knowledge about the global flow differences depending on the wheels. A wheel with a low aerodynamic drag had a higher base pressure, in general, whereas a wheel with high drag had low base pressure, especially at the bottom edges of the base. The wheel house pressure measurements were useful for understanding the flow at the wheel. It was found that closing the cooling flow decreased the overall pressure inside the front wheel house. The most significant change in wheel house pressure was found when using the cover plate to fully cover the wheels. Then, a low pressure zone was found at the outer edge of the front wheel arch, downstream of the front axle. This could only be seen when using the cover plates.

Great differences in the flow field could be seen for the most important wheel parameters, the coverage area and the rim cover. The wake plane measurements could capture these different structures, in terms of $C_{P,tot}$, and the vorticity plots could describe the vortex structures around the front wheel. It was concluded that a high coverage area parted the near-ground and the upper regions of low total pressure at the front wheel. The more open wheel had air flowing in to the upper and centre part of the wheel, something that the more covered wheel restricted. It was also concluded that having a rim cover without a step to the top surface of the spoke limited flow out from the lower part of the wheel. Having no rim cover or a lowered rim cover allowed flow through the lower part of the wheel, feeding energy to the jetting vortex. When this occurred, high near-ground vorticity could be found at the front wheel which resulted in lower energy flow at the rear, decreasing the base pressure. Overall, it was found that wheels which weakened the near-ground vortex performed better, having a lower aerodynamic drag.

The numerical CFD investigation proved that a sliding mesh setup of the rotating wheels could predict trends in aerodynamic drag between wheel configurations well. The absolute drag values were not as accurate. The sliding mesh solution showed similar flow structures near the front wheel, both in terms of total pressure and vorticity, thus it was concluded that the CFD method could be used to analyse the flow around the front wheel. The flow further downstream was found to be more difficult to predict. The additional numerical analysis confirmed that an open wheel has a much higher outflow through the lower part of the wheel, compared to a more closed wheel. The more closed wheel had instead a higher outflow at the wheel arch downstream of the front axle. This was found to increase the strength of the vortex from the wheel arch, also correlating to the low pressure zone found inside the wheel house for the fully covered wheel.

6 Recommendations for future work

The regression model of the wheel parameters was developed on a 18 inch wheel equipped with a set of 245/45 tires. It is recommended to extend the model to include different wheel dimensions as a parameter. Furthermore, investigations about the tire geometries in combination with wheel parameters would make the model even more robust and thus more useful.

Another possible continuation project could be to develop a tool in which a virtual wheel geometry could be loaded and quantify the wheel in terms of the wheel parameters used in this thesis. By doing so, an automatic evaluation of a real wheel could be done by using this tool in combination with the regression model developed in this project.

To further gain knowledge about wheel aerodynamics it is recommended to perform flow field measurement in a plane in front of the front wheel, to determine if there are any vortex structures entering the wheel or if all the vortex structures found in this project was generated by the front wheel, tire or wheel arch. Likewise, it would be interesting to analyse if the rear wheel also has a jetting vortex like the front wheel, by measuring a plane at the centre of the rear wheel. The CFD results showed interesting flow patterns in and out of the front wheel. Therefore, verification by experimental measurements would strengthen those results. This thesis work performed flow field measurements on the two most important parameters of the wheel, the coverage area and the rim cover. Another important parameter was found to be the depth of centre. Hence, it is recommenced to include flow field measurement of that parameter in future work, to further understand why that parameter had a high impact on the aerodynamic drag.

The CFD simulations analysing the coverage area showed similar trends as the experimental data. Therefore, it is recommended to perform simulation of the rim cover step to further evaluate the CFD method's possibilities to analyse wheel aerodynamics.

Finally, since aerodynamics is more complex than just analysing the aerodynamic drag, it is recommended to create a regression model using the same wheel parameters but having the aerodynamic lift as the response.

References

[1] Eurostat. *Passenger transport statistics*. URL: http://ec.europa.eu/eurostat/statistics-explained/index.php/Passenger_transport_statistics (visited on 2017-08-18).

[2] The U.S. Energy Information Administration (EIA). *International Energy Outlook 2016*. URL: https://www.eia.gov/outlooks/ieo/ (visited on 2017-08-18).

[3] OICA, the International Organization of Motor Vehicle Manufacturers. *Production statistics*. URL: http://www.oica.net/category/production-statistics/ (visited on 2017-08-17).

[4] W. H. Hucho. *Aerodynamics of Road Vehicles*. 1987.

[5] E. Mercker et al. 'On the Aerodynamic Interference Due to the Rolling Wheels of Passenger Cars'. In: SAE Technical Paper No. 910311 (1991).

[6] G. Wickern, K. Zwicker and M. Pfadenhauer. 'Rotating Wheels - Their Impact on Wind Tunnel Test Techniques and on Vehicle Drag Results'. In: SAE Technical Paper No. 970133 (1997).

[7] The European Union (EU). *Euro 1 emissions regulation*. URL: http://eur-lex.europa.eu/legal-content/EN/TXT/?uri=CELEX:31991L0441 (visited on 2017-09-08).

[8] Eurostat. *Air pollution statistics*. URL: http://ec.europa.eu/eurostat/statistics-explained/index.php/Air_pollution_statistics#Further_Eurostat_information (visited on 2017-09-20).

[9] The National Aeronautics and Space Administration (NASA). *Global Climate Change - Facts - Causes*. URL: https://climate.nasa.gov/causes/ (visited on 2017-09-20).

[10] The European Commission. *Reducing CO2 emissions from passenger cars*. URL: https://ec.europa.eu/clima/policies/transport/vehicles/cars_en#tab-0-0 (visited on 2017-09-08).

[11] Transport & Environment. 'Mind the Gap'. In: European Federation for Transport and Environment AISBL (2016).

[12] The United Nations Economic Commission for Europe (UNECE). *Worldwide harmonized Light vehicles Test Procedure (WLTP)*. URL: https://wiki.unece.org/pages/viewpage.action?pageId=2523179 (visited on 2017-08-17).

[13] The European Commission. *COMMISSION REGULATION (EU) 2016/427 of 20 April 2016*. URL: http://eur-lex.europa.eu/legal-content/EN/TXT/PDF/?uri=CELEX:32016R0427&from=EN (visited on 2017-11-10).

[14] The United Nations Economic Commission for Europe (UNECE). *DHC-12th session*. URL: http://www.unece.org/trans/main/wp29/wp29wgs/wp29grpe/wltp_dhc12.html (visited on 2017-08-17).

[15] C. Stover and E. W. Weisstein. *Einstein Summation*. URL: `http://mathworld.wolfram.com/EinsteinSummation.html` (visited on 2018-05-20).

[16] F. M. White. *Fluid Mechanics*. 7th ed. 2011.

[17] L. Davidson. 'Fluid mechanics, turbulent flow and turbulence modeling'. 2017.

[18] S. Hoyas and J. Jimenez. *DNS data of fully developed plane turbulent channel flow*. URL: `https://torroja.dmt.upm.es/ftp/channels/data/statistics/` (visited on 2018-04-23).

[19] M. Eng. 'Investigation of aerodynamic correction methods applied to a slotted wall wind tunnel'. Master's thesis. 2009.

[20] E. Mercker. 'On the Correction of Open and Slotted Wall Wind Tunnels. ECARA /EADE Meeting at Volvo, Gothenburg.' In: (2006).

[21] European Aerodynamic Data Exchange (EADE). 'EADE Correlation Test 2010'. In: (2011).

[22] A. Cogotti. 'A strategy for Optimum surveys of Passenger-Car Flow Fields'. In: SAE Technical Paper No. 890374 (1989).

[23] S. Bonitz. 'An investigation into the aerodynamic ventilation drag incurred by wheel rotation on a passenger car, and its influence on the total road load of the car'. Master's thesis. 2011.

[24] A. Wäschle. 'The Influence of Rotating Wheels on Vehicle Aerodynamics – Numerical and Experimental Investigations'. In: SAE Technical Paper No. 2007-01-0107 (2007).

[25] A. Vdovin. 'Numerical and Experimental Investigation on Aerodynamic and Thermal Aspects of Rotating Wheels'. Doctoral thesis. 2015.

[26] F. R. Menter. 'Zonal two-equation k-ω turbulence model for aerodynamic flows'. In: *AIAA Paper 1993-2906* (1993).

[27] M .S Gritskevich et al. 'Development of DDES and IDDES Formulations for the k-ω Shear Stress Transport Model'. In: *Flow, Turbulence Combust* (2012).

[28] T. Hobeika. 'Wheel Modelling and Cooling Flow Effects on Car Aerodynamics'. Doctoral thesis. 2018.

[29] Minitab. *Minitab StatGuide*. Version 17.3.1.

[30] J. Sternéus, T. Walker and T. Bender. 'Upgrade of the Volvo Cars Aerodynamic Wind Tunnel'. In: SAE Technical Paper No. 2007-01-1043 (2007).

[31] P. Elofsson and M. Bannister. 'Drag Reduction Mechanisms Due to Moving Ground and Wheel Rotation in Passenger Cars'. In: SAE Technical Paper No. 2002-01-0531 (2002).

[32] V. Robertsson. 'Development of a New Cost-Efficient Procedure for Evaluation of Wheel Design Aerodynamic Performance'. Master's thesis. 2017.

[33] C. Landström. 'Passenger Car Wheel Aerodynamics'. Doctoral thesis. 2011.

[34] Siemens. *STAR-CCM+ User Guide*. Version 12.04.011.

[35] Additive Manufacturing Research Group - Loughborough University. *Powder bed fusion technique*. URL: http://www.lboro.ac.uk/research/amrg/about/the7categoriesofadditivemanufacturing/powderbedfusion/ (visited on 2018-04-22).

[36] T. Wahlström and J. Sahlström. 'Additive Manufacturing in Production'. Master's thesis. 2016.

[37] BASF Corporation. *Snap-Fit Design Manual*. 2007. URL: http://web.mit.edu/2.75/resources/random/Snap-Fit%20Design%20Manual.pdf (visited on 2018-04-22).

Appendices

Appendix A: Base wheel and plastic inserts

A.1 Design process of the base wheel

The concept of using a slim base wheel to mount plastic inserts on, was developed during a previous thesis work at VCC [32]. The base wheel design developed in that thesis work was used as a starting point for the development of the wheel used in this project, see Fig. A.1a. The most important attribute of the base wheel was to allow for high degree of design freedom of the plastic inserts. This was fulfilled by a slim spoke design. However, three possible improvements were found by analysing the performance of the previous base wheel:

1. Change hub design to be able to mount the cover plates on the base wheel.
2. Perform strength and fatigue analysis to create a robust yet slim wheel design.
3. Mill the backside of the spokes to enhance the surface tolerance and enable more precise mounting of plastic inserts.

The first improvement was easily implemented on the new base wheel, since the hub thickness only needed to be increased by 2.5 mm to preserve the hub groove that was used to mount the cover plates (and the centre caps).

A new, stronger, base wheel design was developed in this project. Both wider and thicker spokes along with a more robust transition from spoke to rim track were implemented, see Fig. A.1b. The strength and fatigue analysis was performed by a wheel supplier. This was an iterative process where the supplier performed the

(a) Previous base wheel.

(b) New base wheel.

(c) Machined backside of the new base wheel.

Figure A.1: Base wheel design development.

Table A.1: Strength and fatigue requirements of the new base wheel.

Load case	Wind tunnel, moving ground (flat road and no lateral forces)
Axle load (per wheel)	5235 N
Driving velocity	140 km/h
Fatigue requirements	$1.5 \cdot 10^6$ cycles (rotations)

analysis and suggested areas of improvements, which were used by the project to re-design the base wheel while keeping the wheel useful for its purpose. This resulted in a new stronger base wheel design still with a high degree of design freedom for the plastic inserts. The strength and fatigue requirements of the base wheel set for the supplier can be seen in Table A.1.

Finally, the new base wheels had to be milled on the backside of the spokes. The base wheels were milled from a regular set of aluminium production wheels, called the donor wheels. This milling process was performed internally at VCC. However, to mill the complete backside of the spokes an additional fixture to mount the wheel upside-down in the milling machine had to be created. Instead of designing and milling this additional fixture, a simpler solution to the problem was found. While mounted regularly in the milling machine, small pockets where the plastic inserts mounted onto the base wheel were milled with a T-slot milling cutter. This method could not mill the complete backside of the spokes, but could still fulfil the task of enabling more precise mounting of plastic inserts. The spoke backside of the new base wheel can be seen in Fig. A.1c.

Between the two wind tunnel sessions, a crack detection test was done, see Fig. A.2. This was done to verify that the base wheel design was strong enough and that the same set of wheels could be used for the second wind tunnel session. First, the wheel was cleaned and a red visualisation paint was sprayed on to the wheel, see Fig.

(a) Applying the red crack visualisation paint. **(b)** Visual inspection.

Figure A.2: The crack detection test between the two wind tunnel sessions.

A.2a. Thereafter, the red paint was wiped off and a developer spray was applied to visualise any red cracks, see Fig. A.2b. As seen in the picture, no distinct crack could be found. The base wheels could thus be used for the second wind tunnel session as well.

A.2 Plastic insert design

The plastic inserts were manufactured using the additive manufacturing technique of selective laser sintering (SLS). The technique uses a bed of plastic powder, in this case polyamide (nylon), placed on a build platform. The laser beam is used to sinter the top layer of the powder bed. Once one layer has been sintered, the platform moves down and a new layer of powder is spread on top of the previous. An advantage of this technique is that the powder bed works as support for the sintered part, which allows for more complex structures to be manufactured [35].

The plastic inserts used a snap-fit design to mount on to the base wheel, see Fig. A.3. The insert was also supported at the wheel hub and at the rim track, to mount firmly. To develop a good design for the plastic parts, a few test prototypes were first manufactured to be tried on the previous base wheel. Design guidelines were used to set parameters such as wall thickness, internal and external radii, assembly distance and snap-fit design [36, 37]. The test parts had varying design to find the optimum fit on the base wheel and also varying snap-fit strength. A rotational test was done by using a biaxial wheel fatigue test rig, see Fig A.4. The base wheel was rotated to a corresponding velocity of 150 km/h, with the plastic inserts mounted on to the wheel. This experiment enabled development of a safe and strong snap-fit design which could be mounted and dismounted without too much effort.

Figure A.3: Snap-fit design.

Figure A.4: Biaxial wheel fatigue test rig.

Appendix B: Front wheel house and base pressure

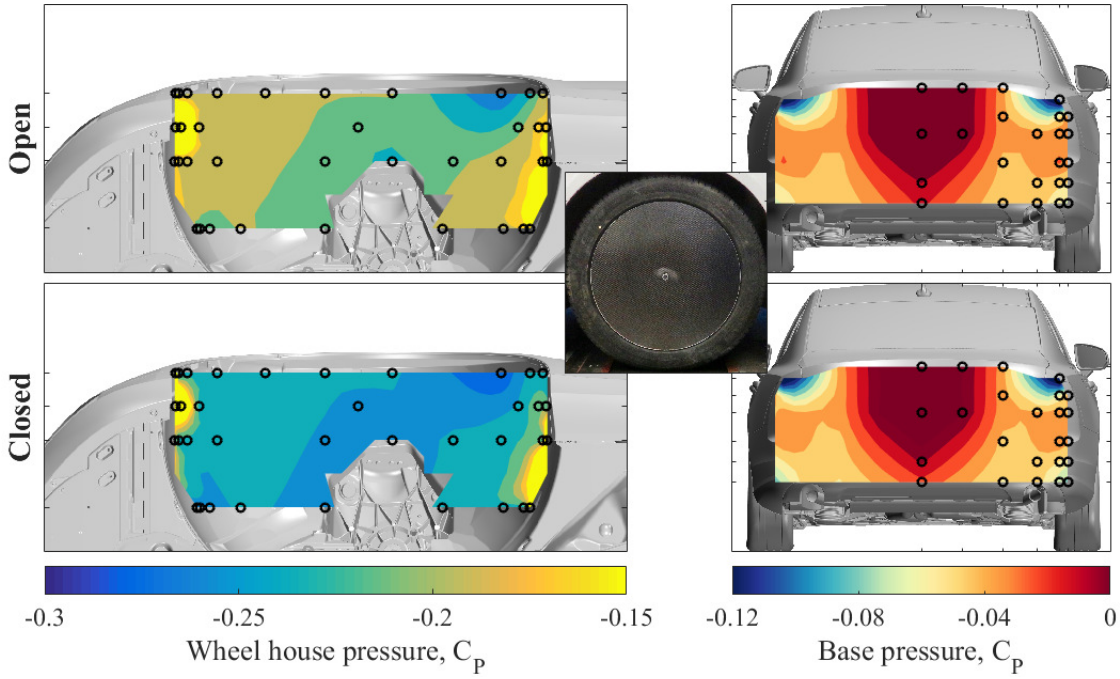

Figure B.1: Donor wheel - Cover plates. The wheel house and base pressure for open and closed cooling flow.

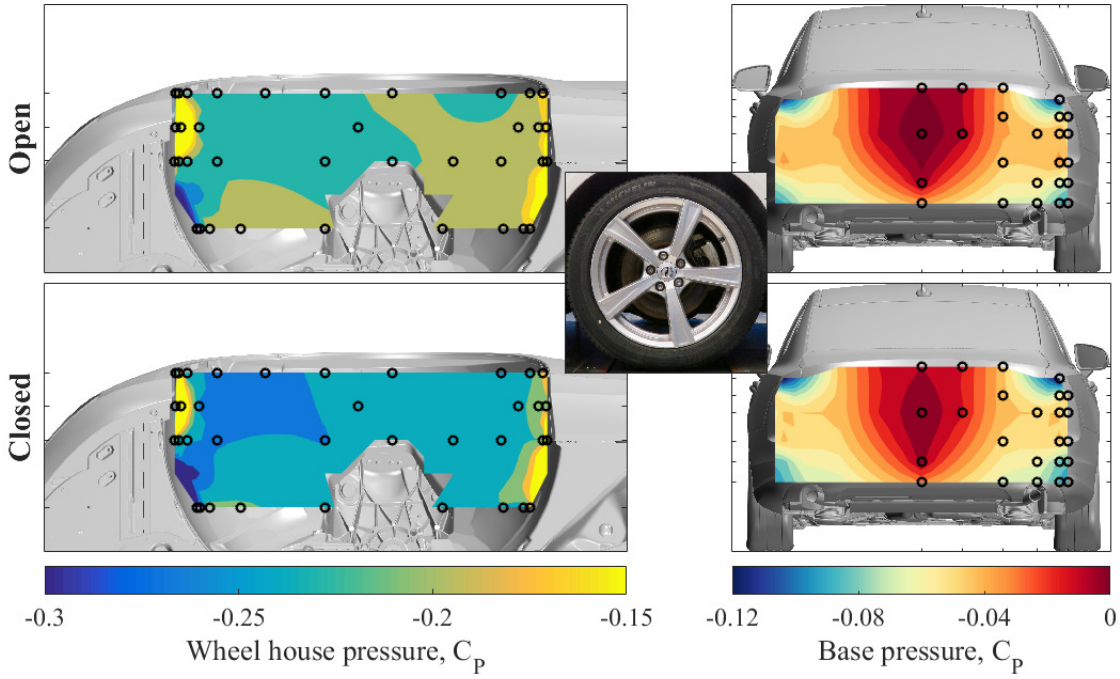

Figure B.2: Donor wheel. The wheel house and base pressure for open and closed cooling flow.

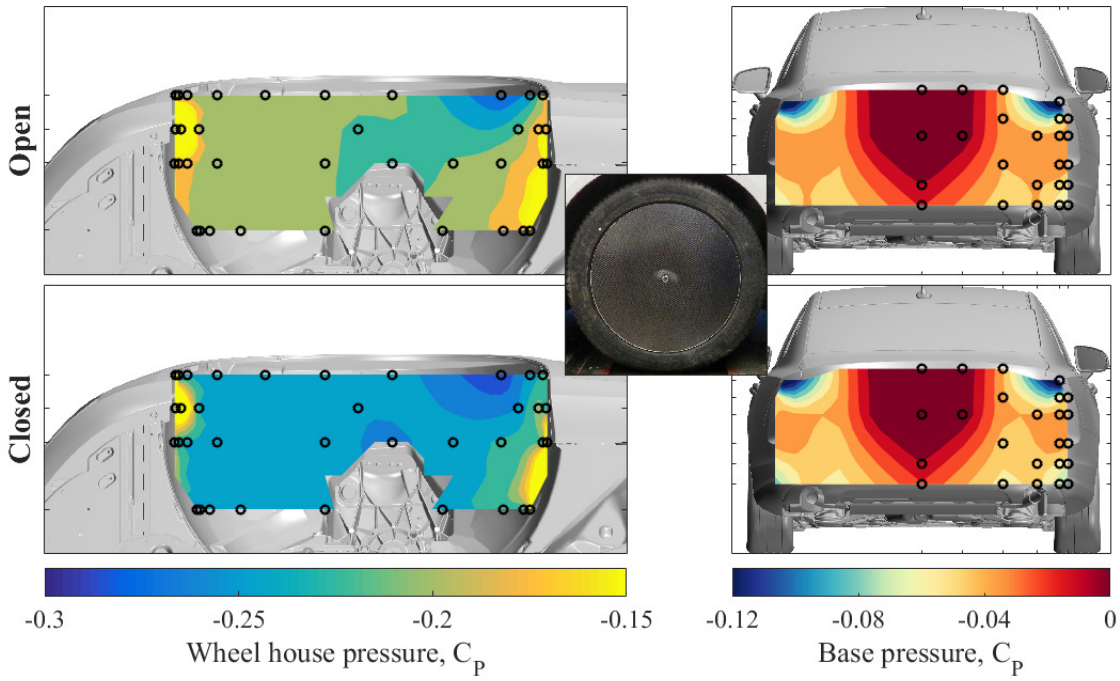

Figure B.3: Base wheel - Cover plates. The wheel house and base pressure for open and closed cooling flow.

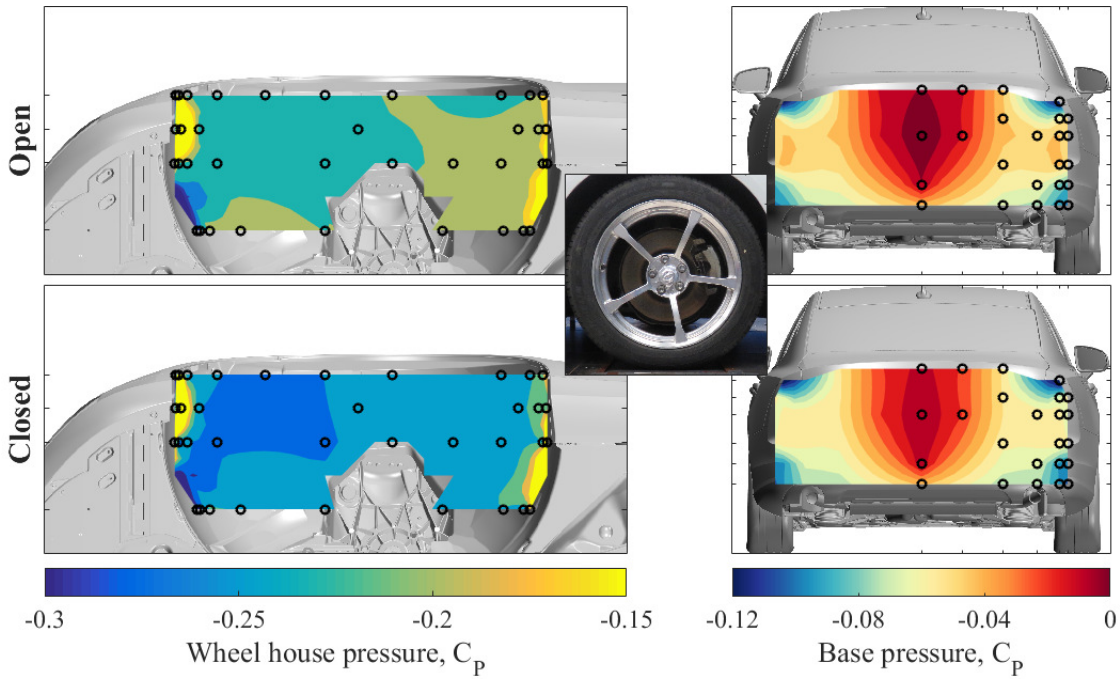

Figure B.4: Base wheel. The wheel house and base pressure for open and closed cooling flow.

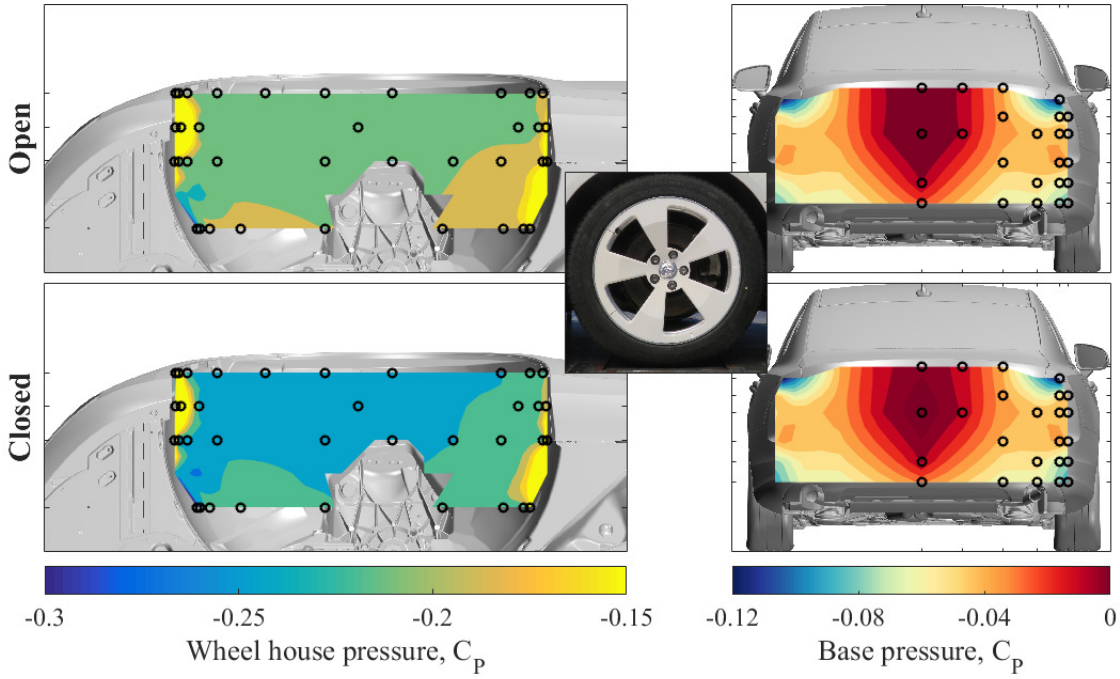

Figure B.5: D01. The wheel house and base pressure for open and closed cooling flow.

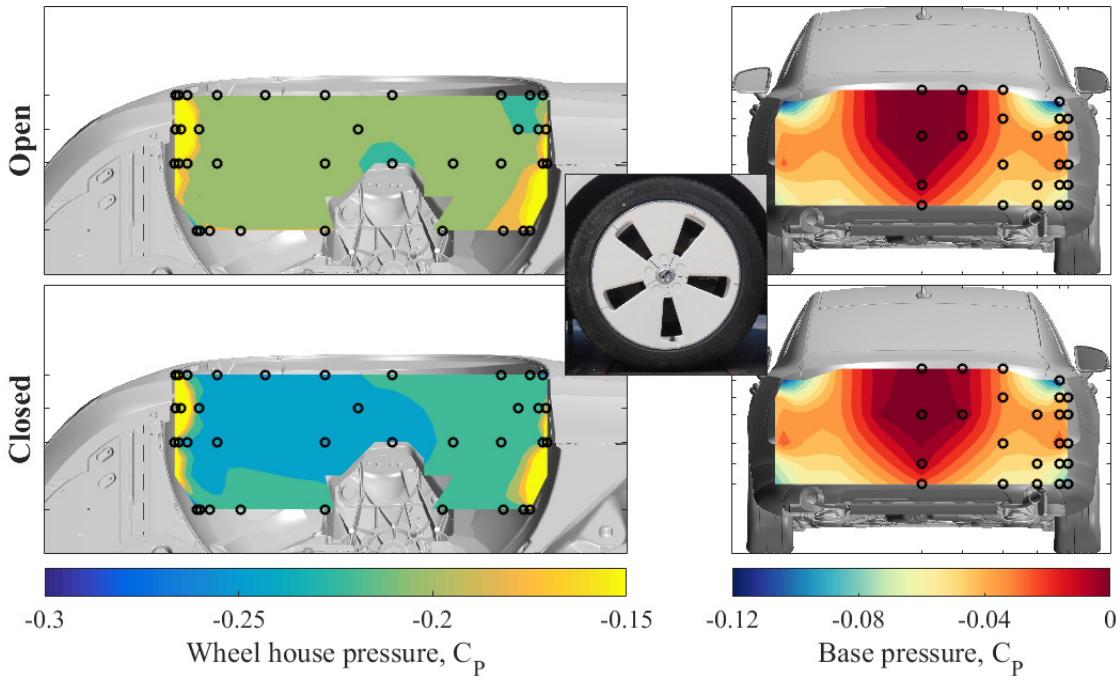

Figure B.6: D02. The wheel house and base pressure for open and closed cooling flow.

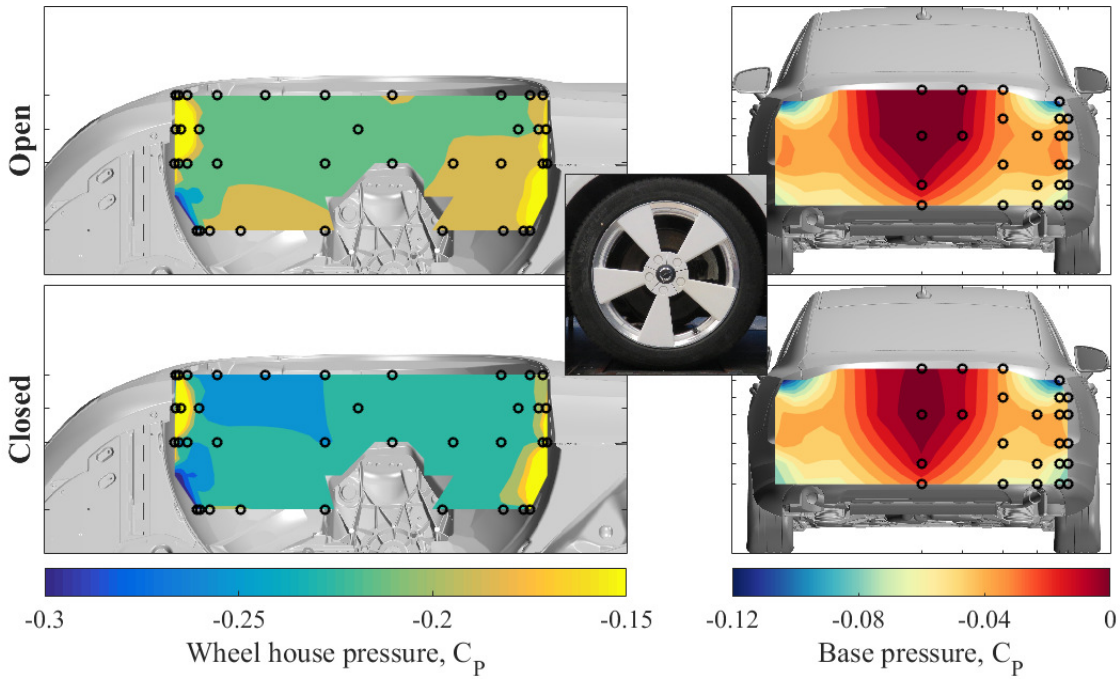

Figure B.7: D03. The wheel house and base pressure for open and closed cooling flow.

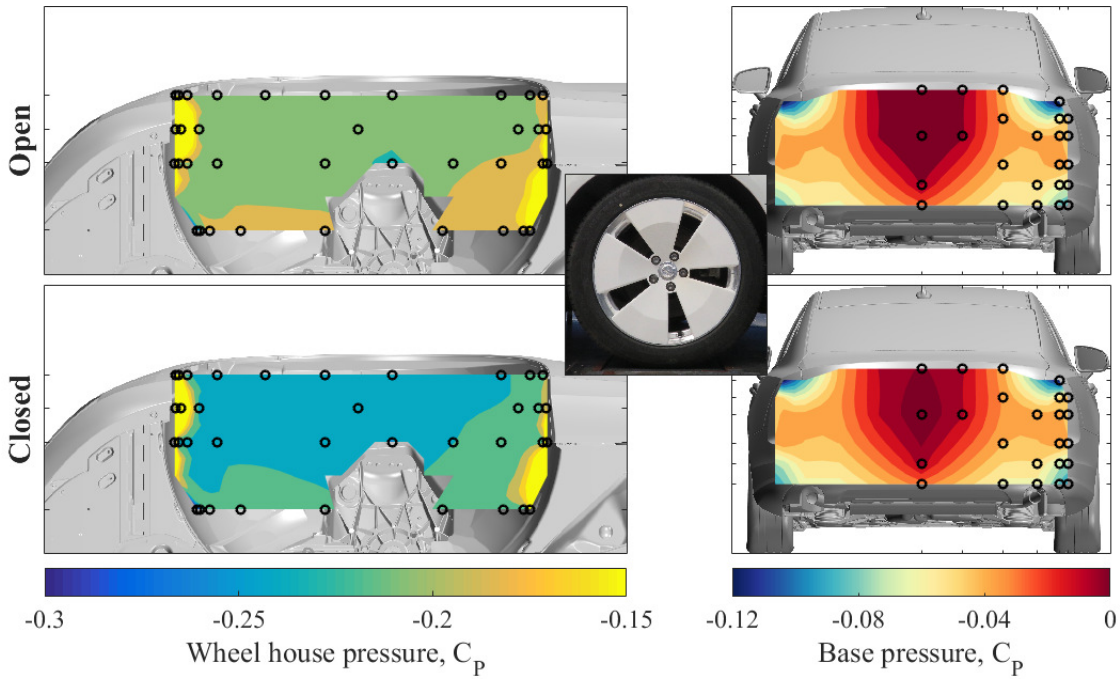

Figure B.8: D04. The wheel house and base pressure for open and closed cooling flow.

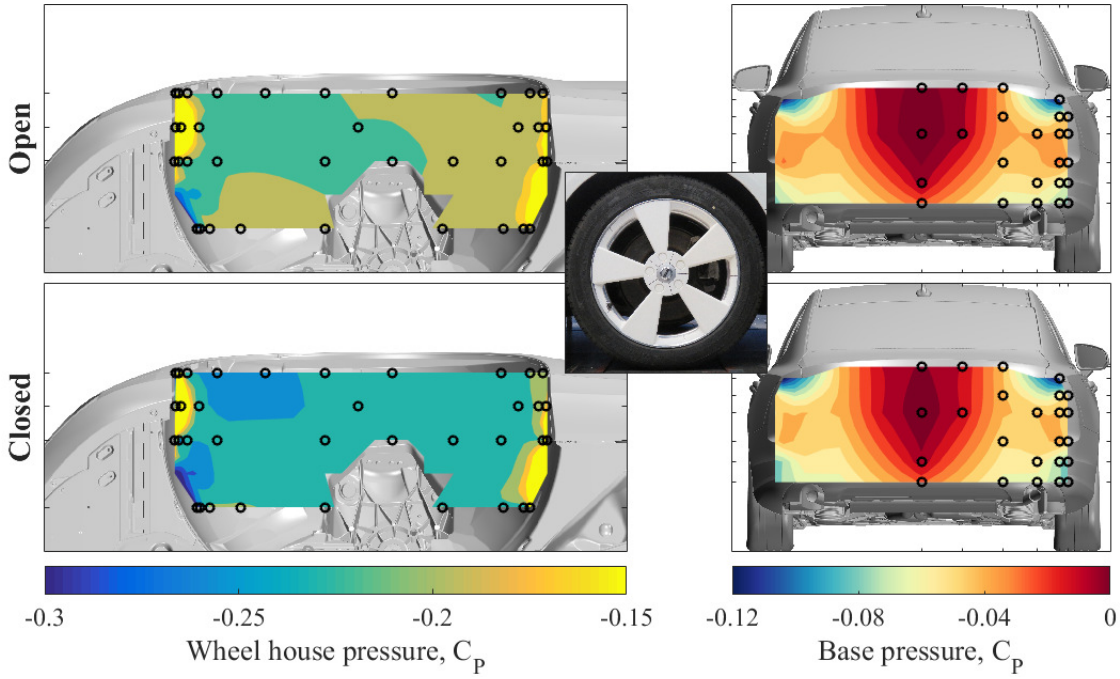

Figure B.9: D05. The wheel house and base pressure for open and closed cooling flow.

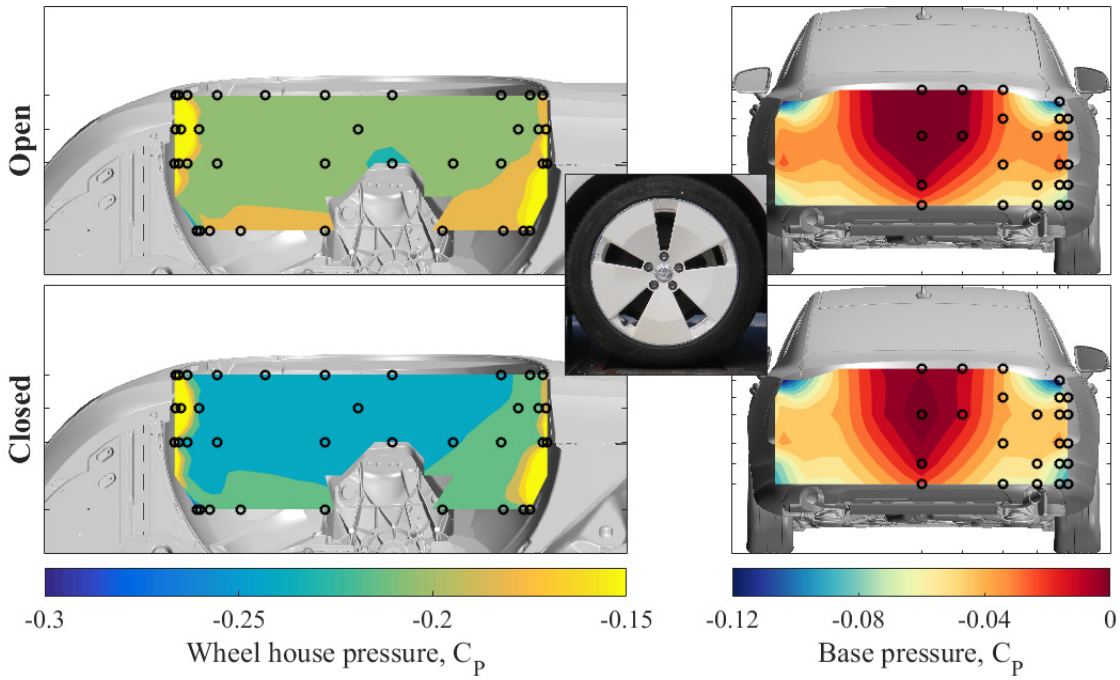

Figure B.10: D06. The wheel house and base pressure for open and closed cooling flow.

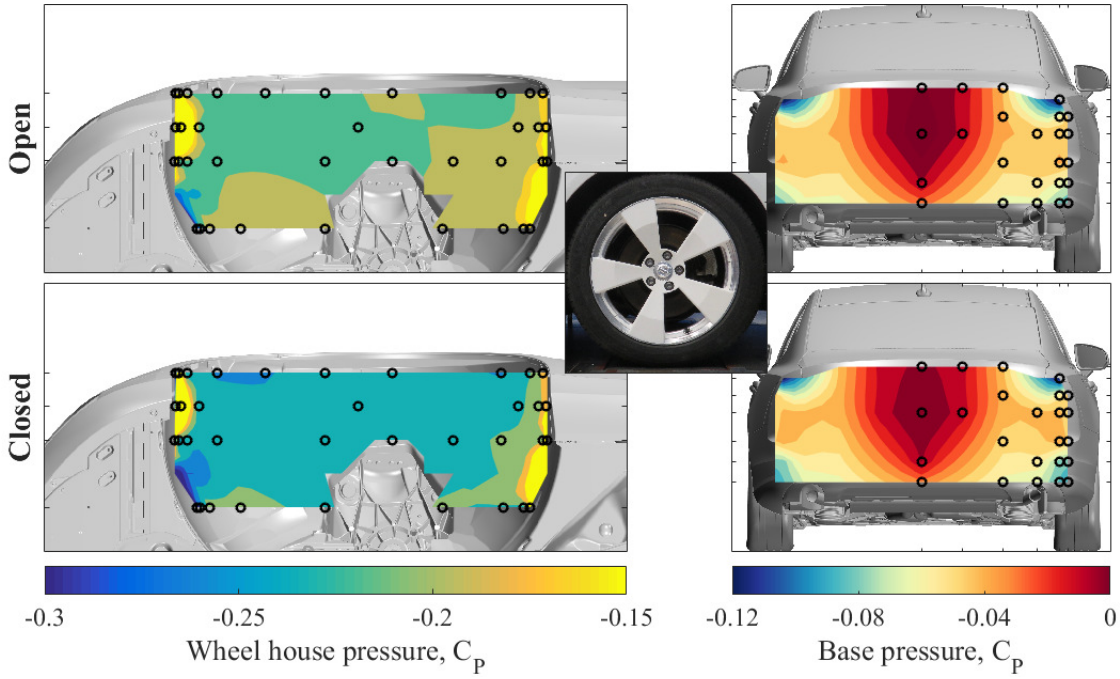

Figure B.11: D07. The wheel house and base pressure for open and closed cooling flow.

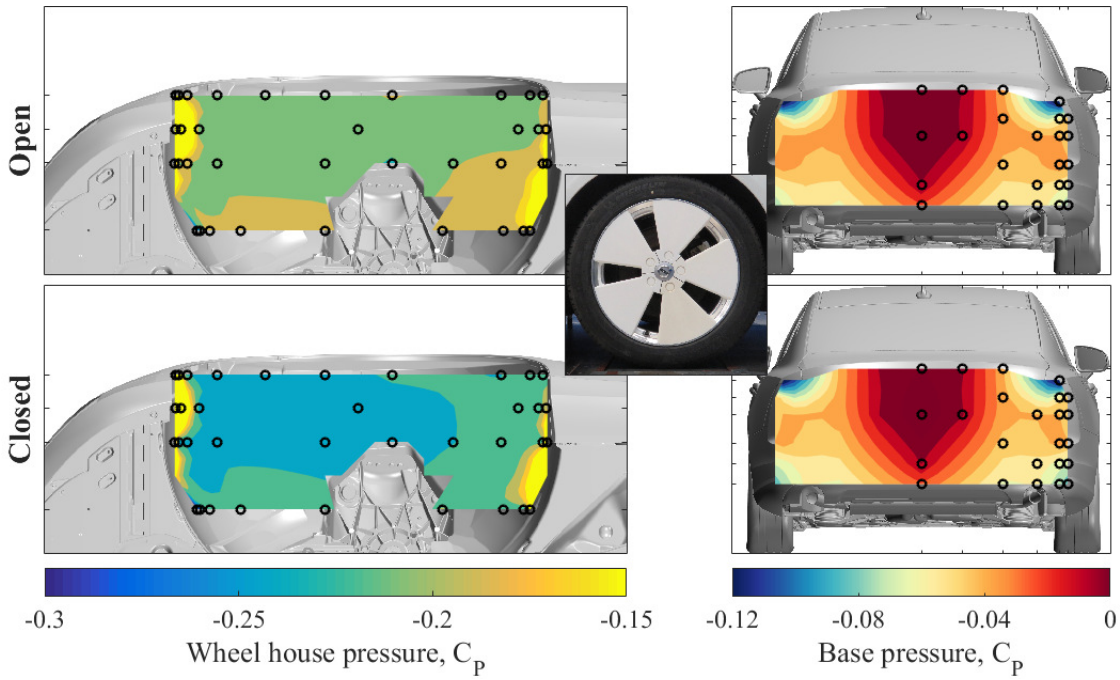

Figure B.12: D08. The wheel house and base pressure for open and closed cooling flow.

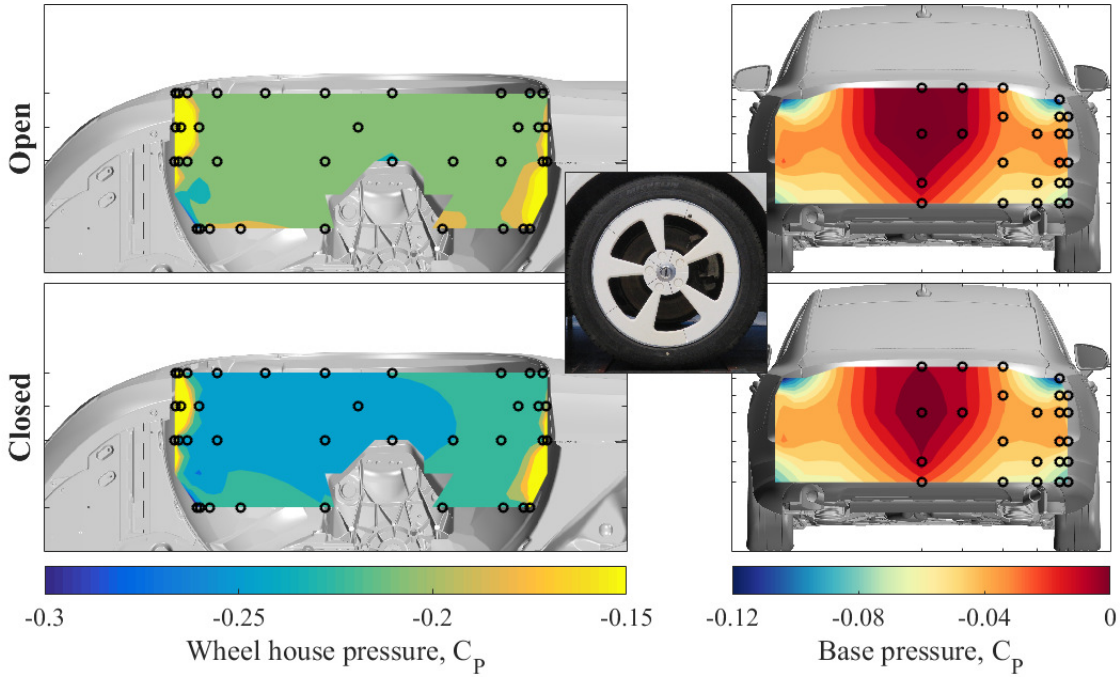

Figure B.13: D09. The wheel house and base pressure for open and closed cooling flow.

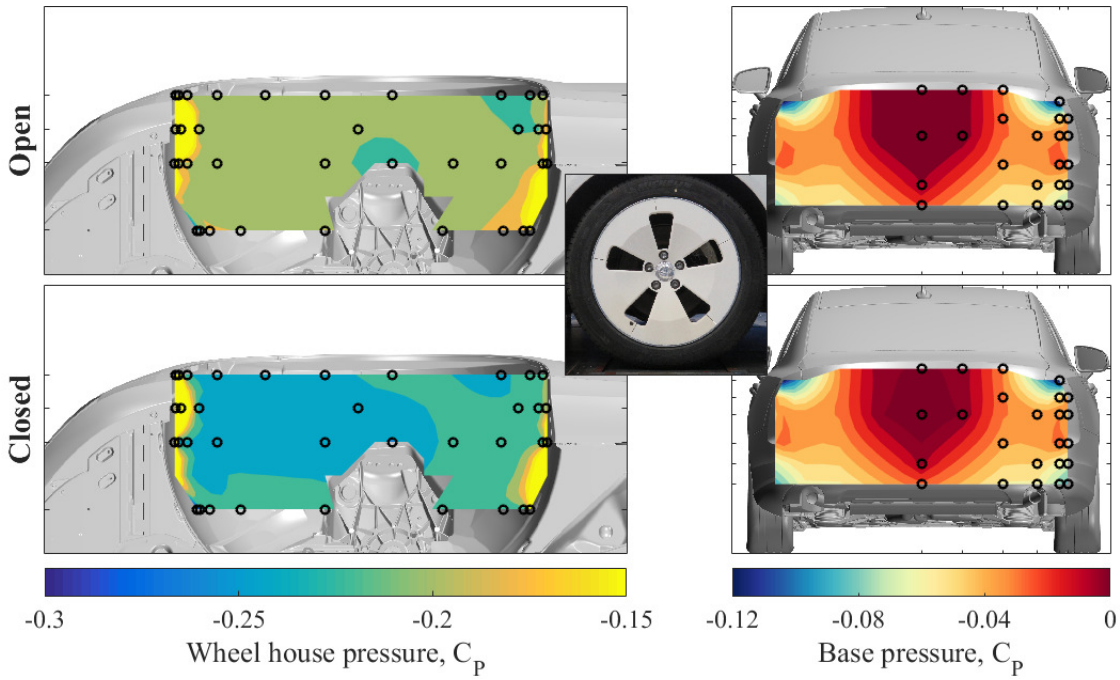

Figure B.14: D10. The wheel house and base pressure for open and closed cooling flow.

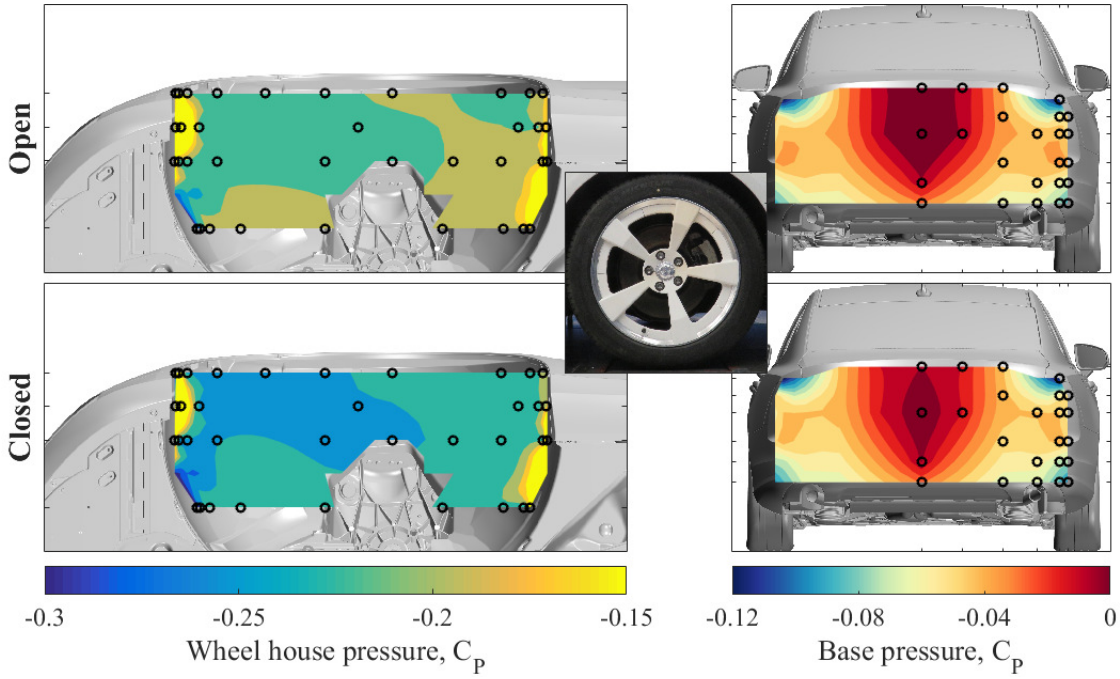

Figure B.15: D11. The wheel house and base pressure for open and closed cooling flow.

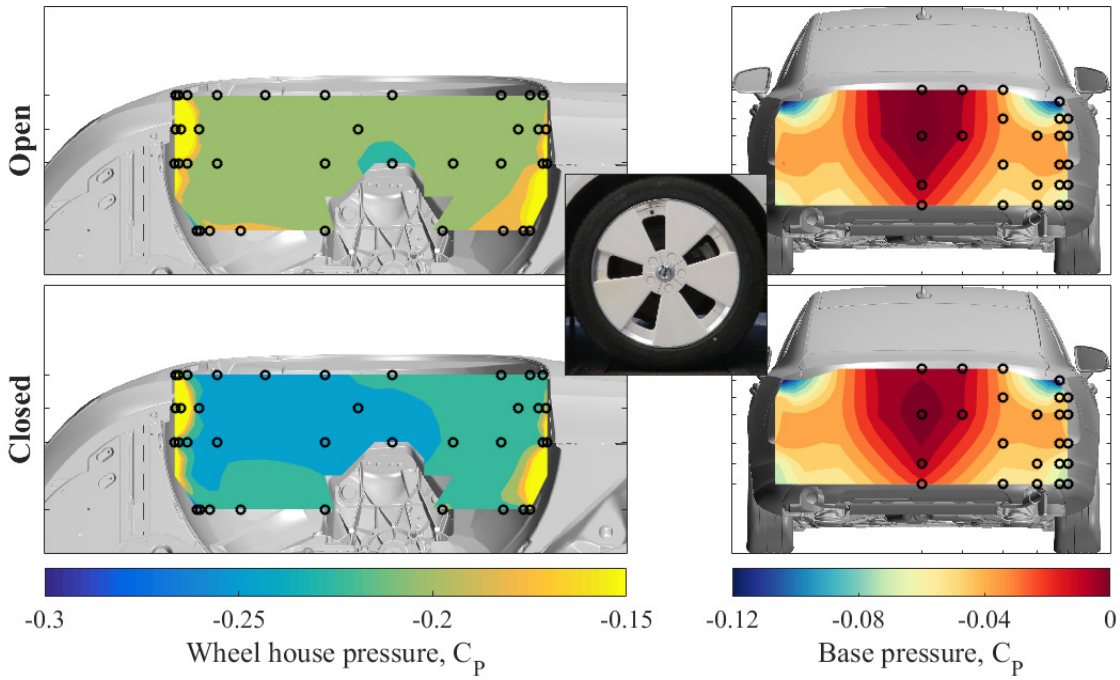

Figure B.16: D12. The wheel house and base pressure for open and closed cooling flow.

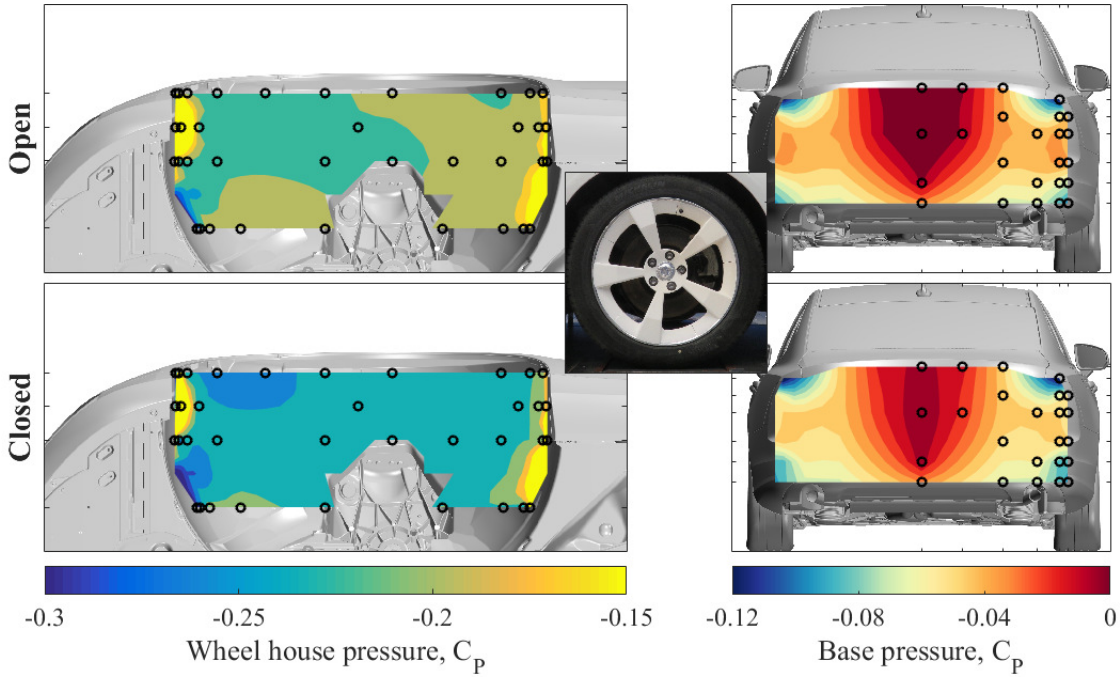

Figure B.17: D13. The wheel house and base pressure for open and closed cooling flow.

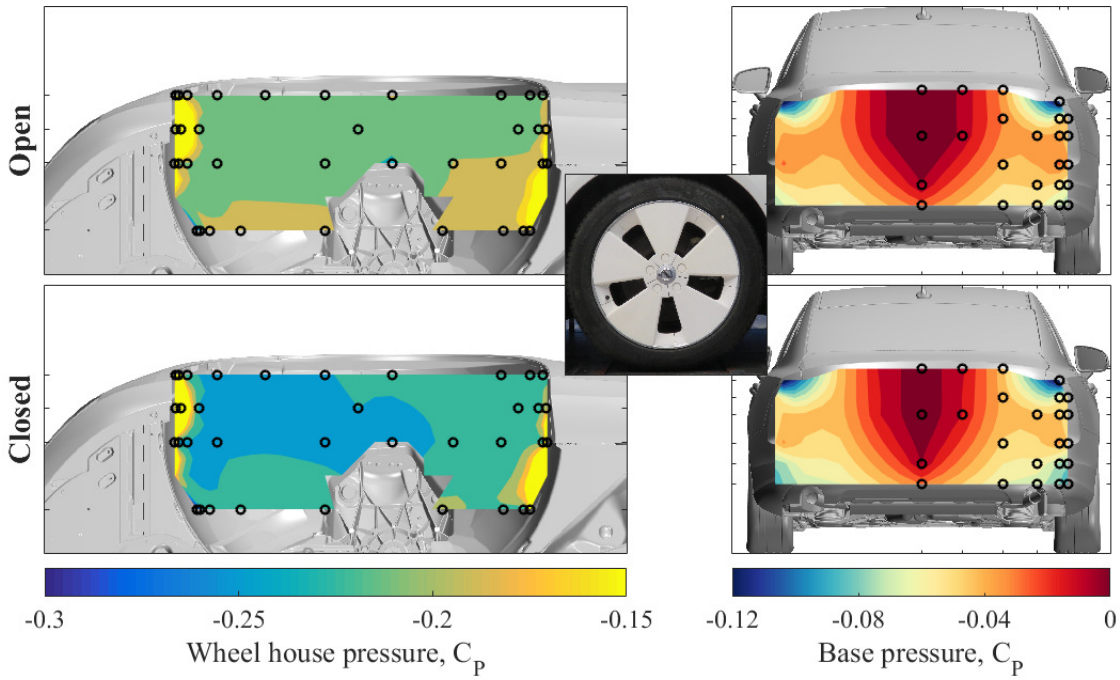

Figure B.18: D14. The wheel house and base pressure for open and closed cooling flow.

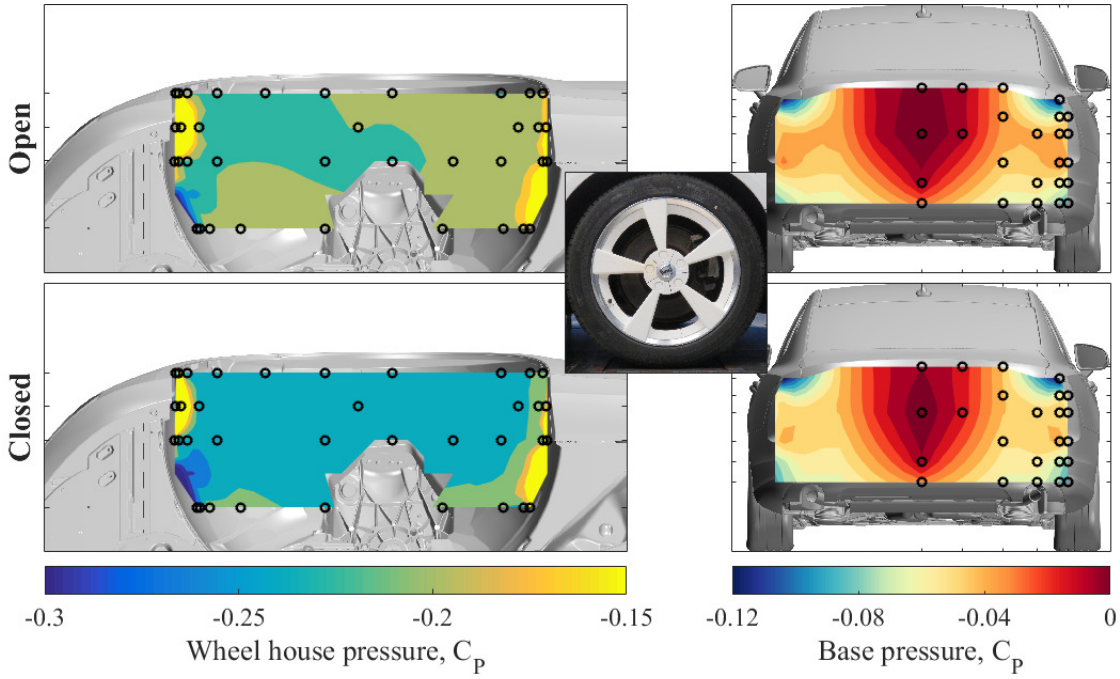

Figure B.19: D15. The wheel house and base pressure for open and closed cooling flow.

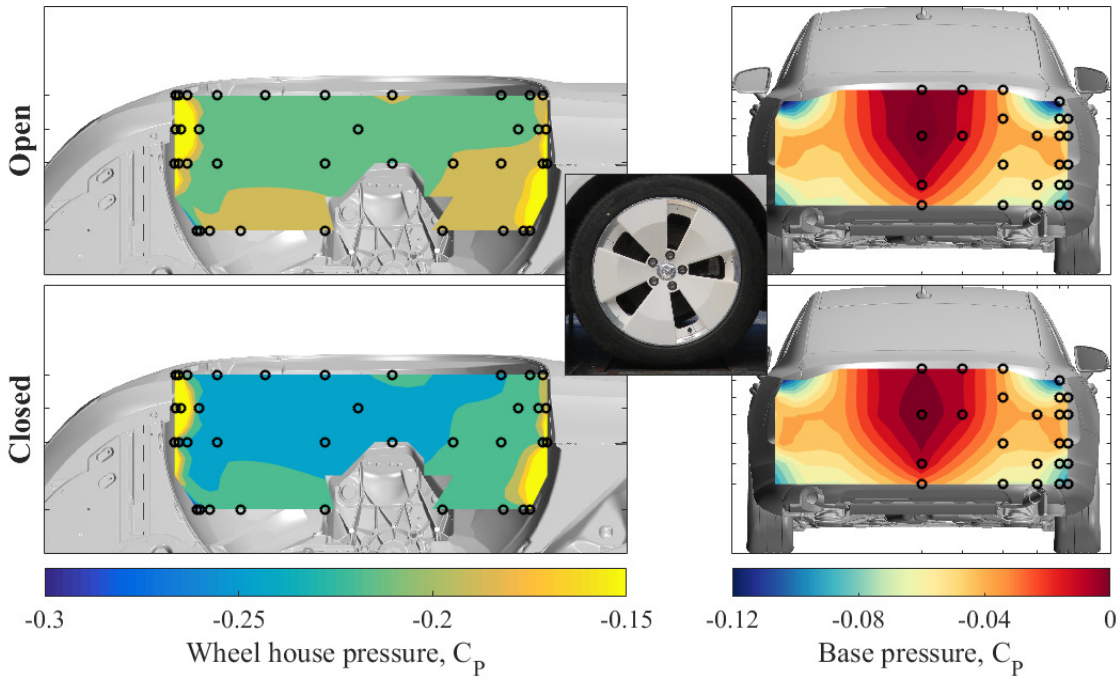

Figure B.20: D16. The wheel house and base pressure for open and closed cooling flow.

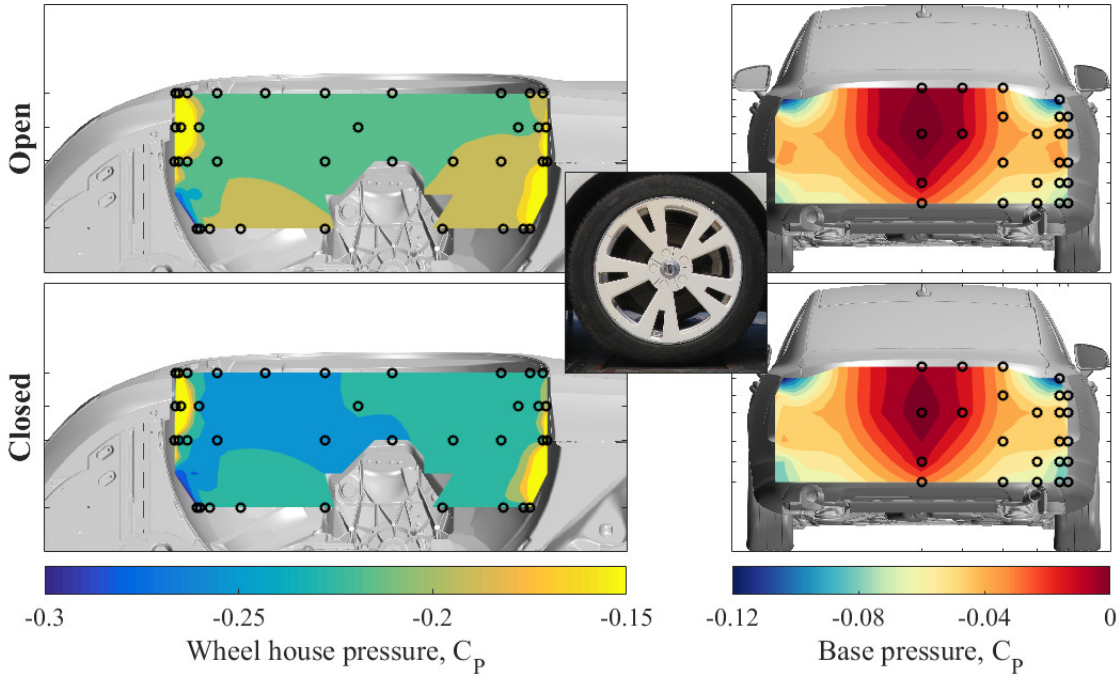

Figure B.21: D17. The wheel house and base pressure for open and closed cooling flow.

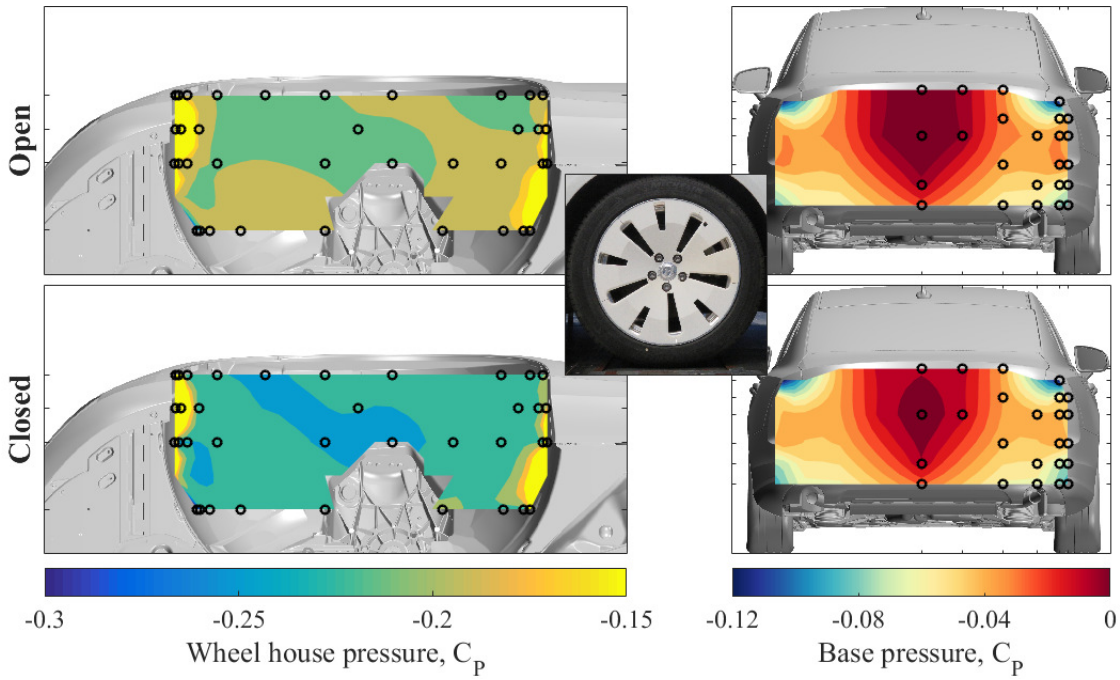

Figure B.22: D18. The wheel house and base pressure for open and closed cooling flow.

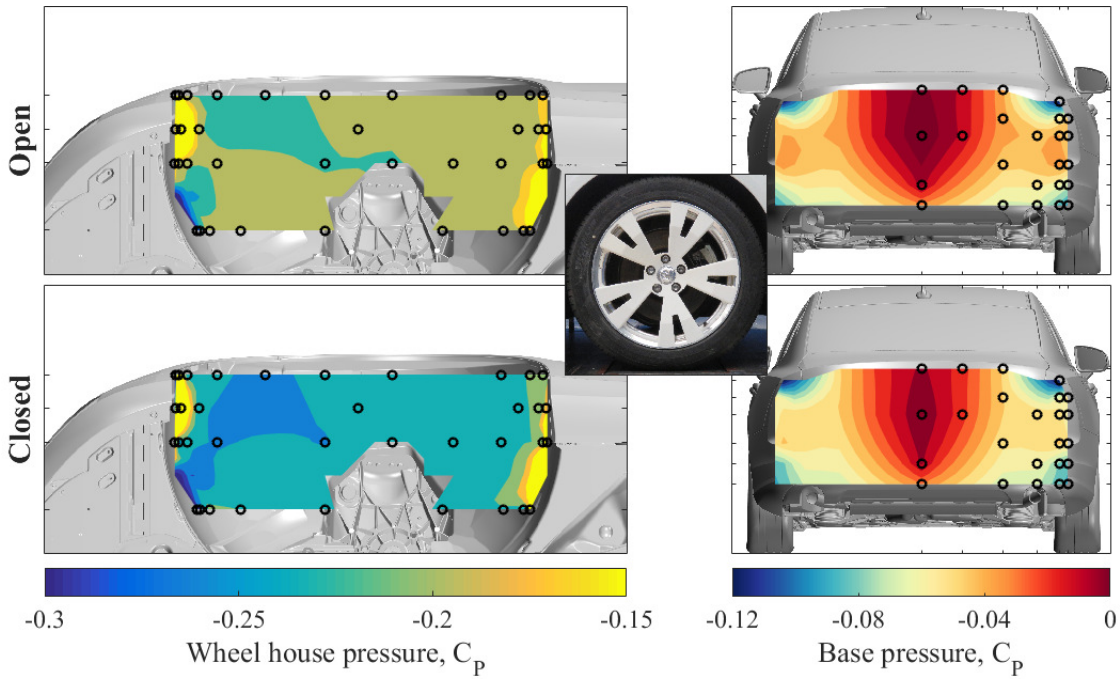

Figure B.23: D19. The wheel house and base pressure for open and closed cooling flow.

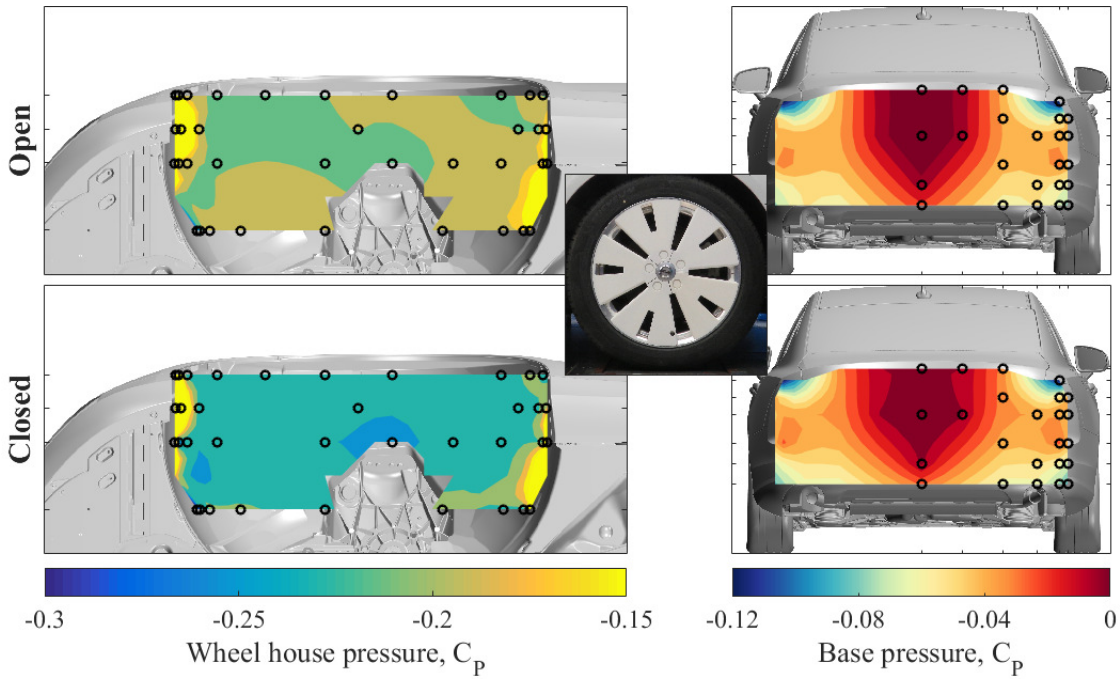

Figure B.24: D20. The wheel house and base pressure for open and closed cooling flow.

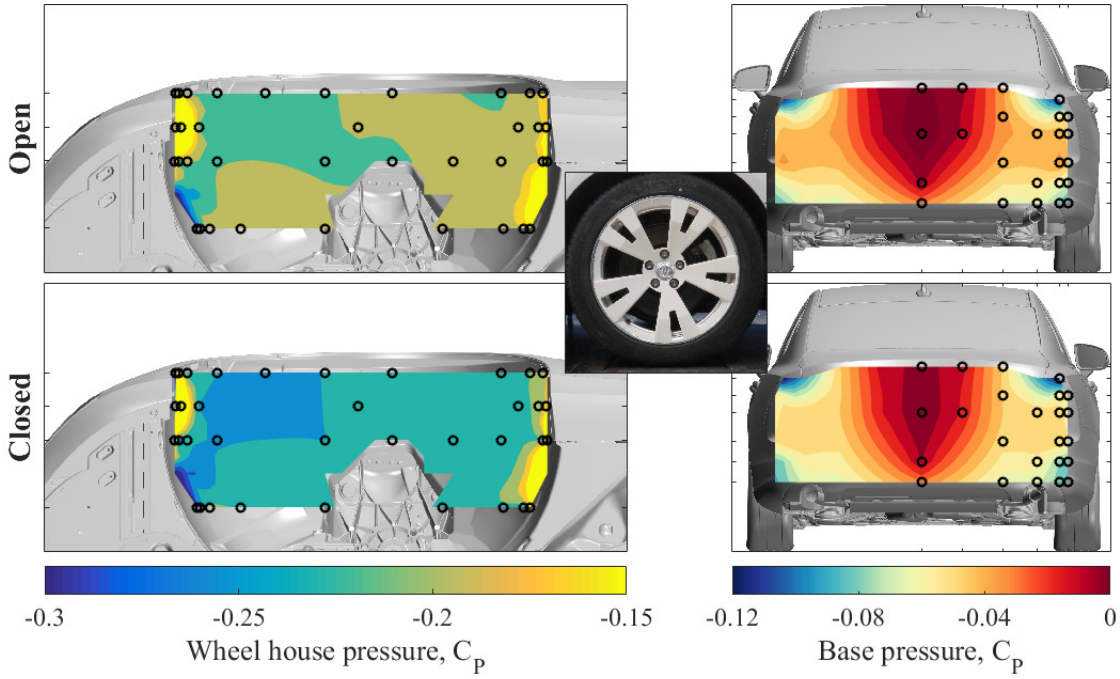

Figure B.25: D21. The wheel house and base pressure for open and closed cooling flow.

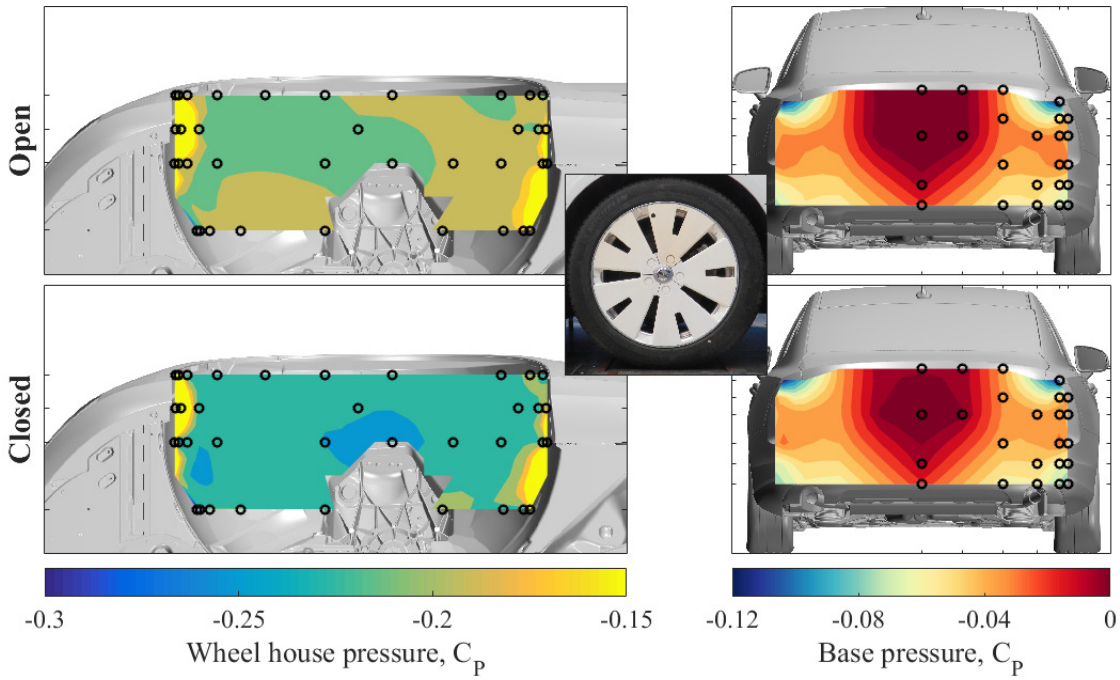

Figure B.26: D22. The wheel house and base pressure for open and closed cooling flow.

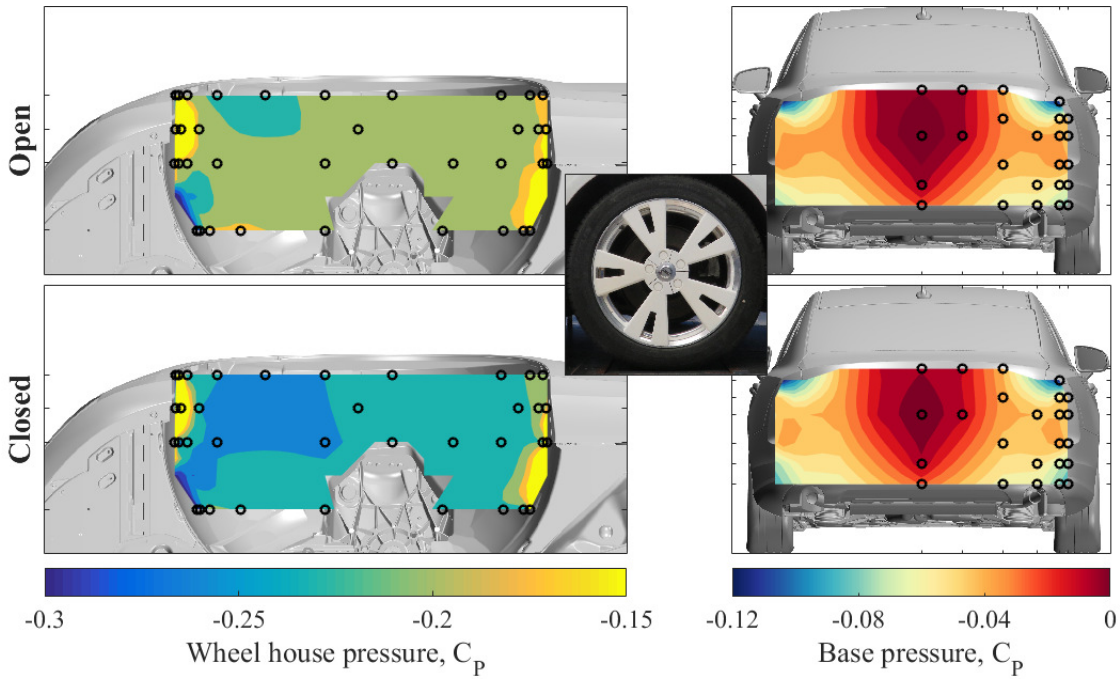

Figure B.27: D23. The wheel house and base pressure for open and closed cooling flow.

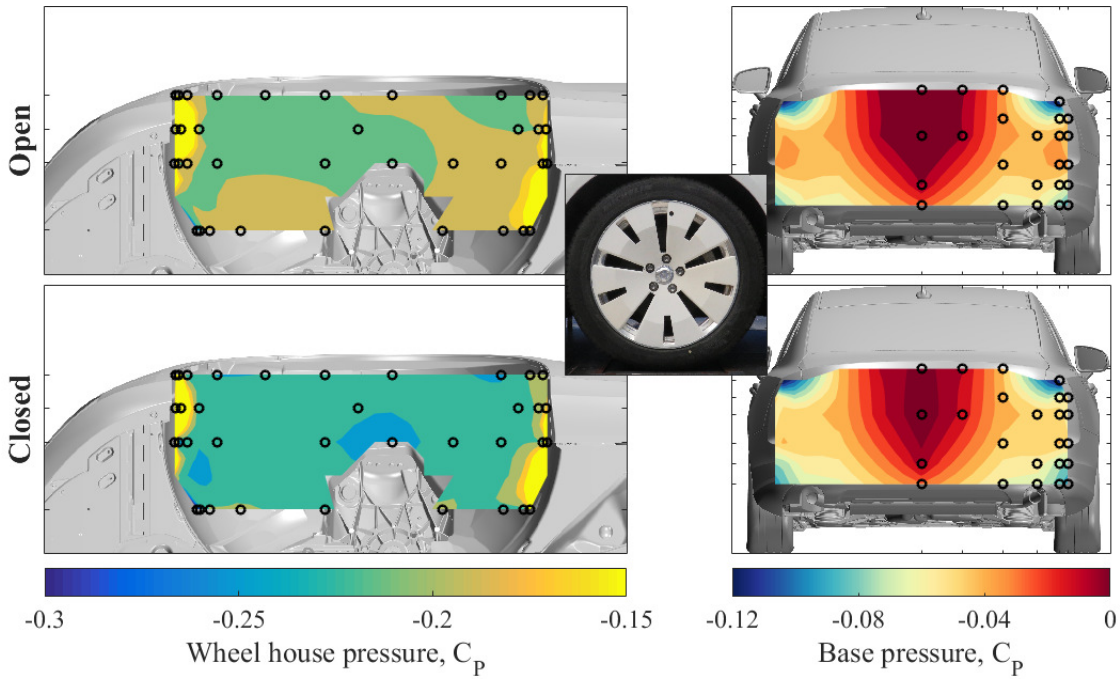

Figure B.28: D24. The wheel house and base pressure for open and closed cooling flow.

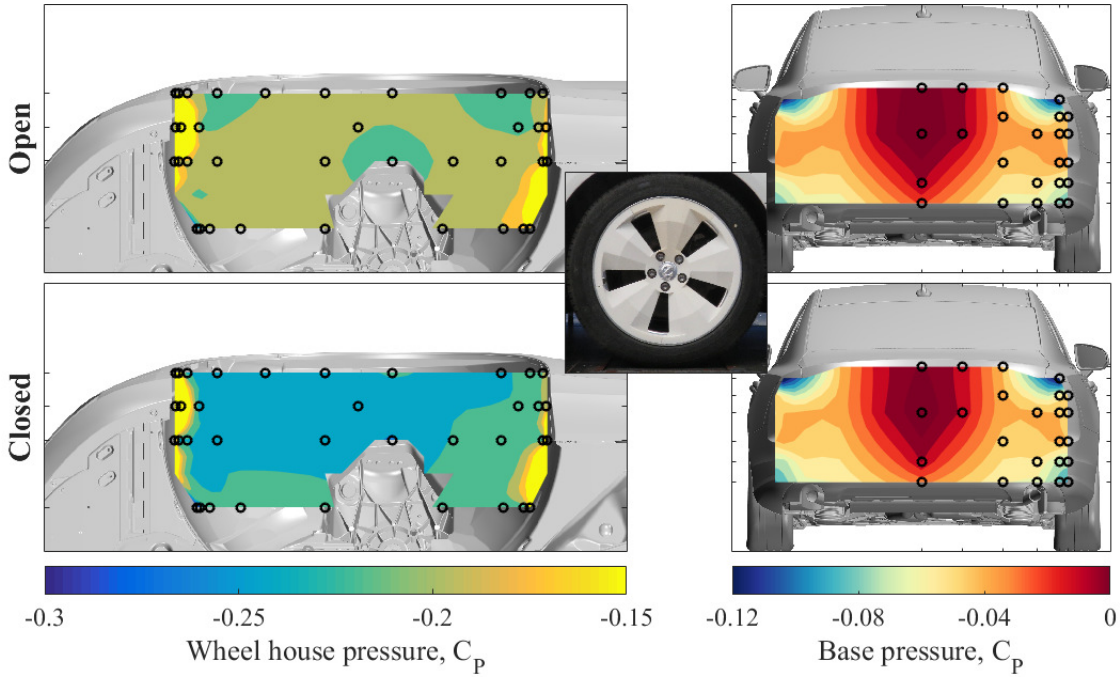

Figure B.29: D25. The wheel house and base pressure for open and closed cooling flow.

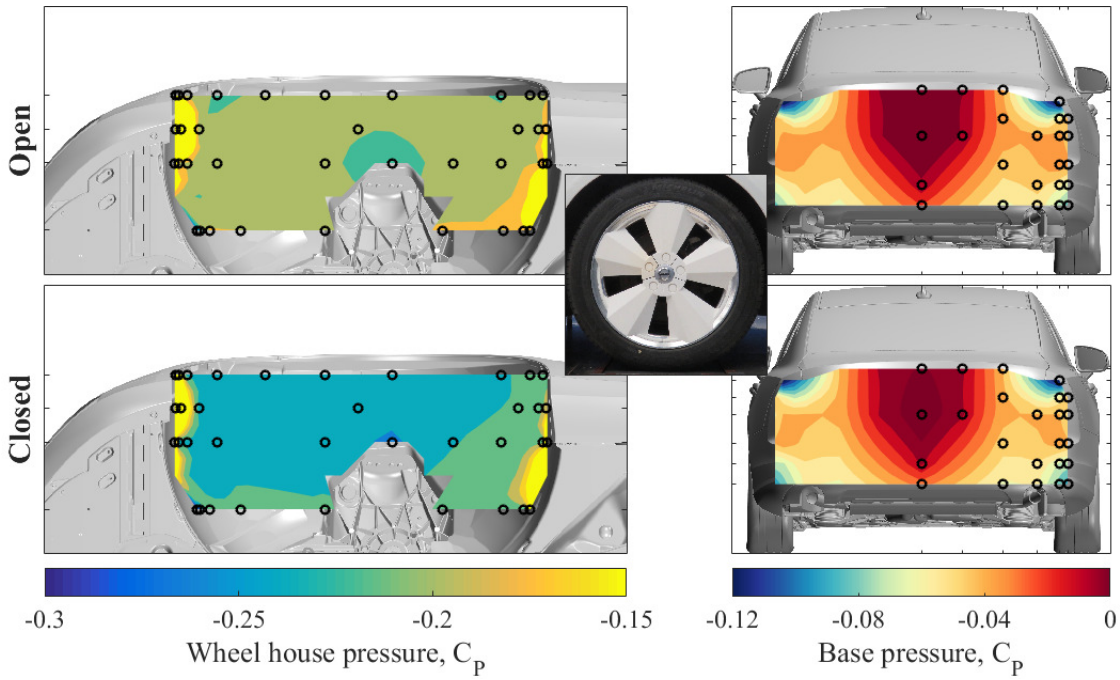

Figure B.30: D26. The wheel house and base pressure for open and closed cooling flow.

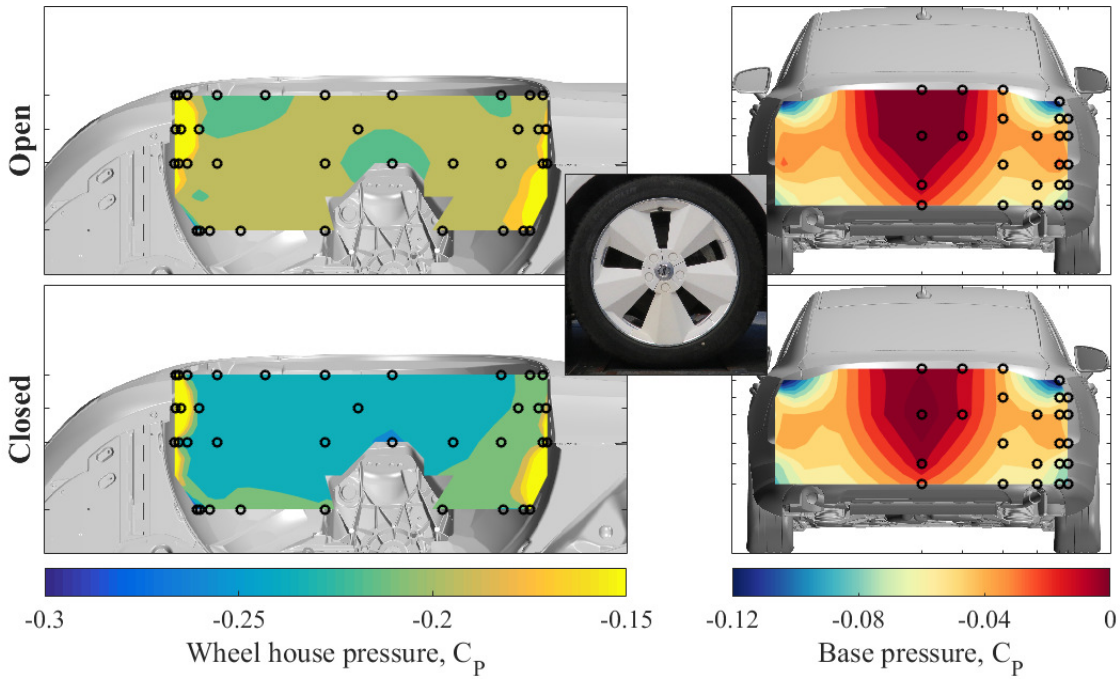

Figure B.31: D27. The wheel house and base pressure for open and closed cooling flow.

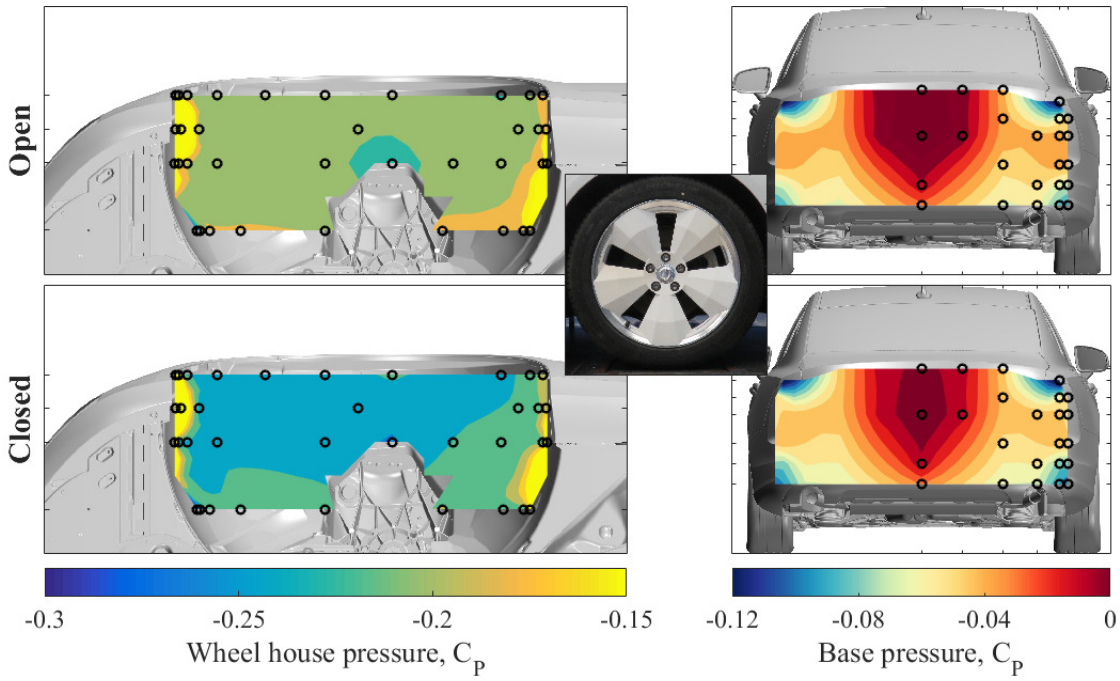

Figure B.32: D28. The wheel house and base pressure for open and closed cooling flow.

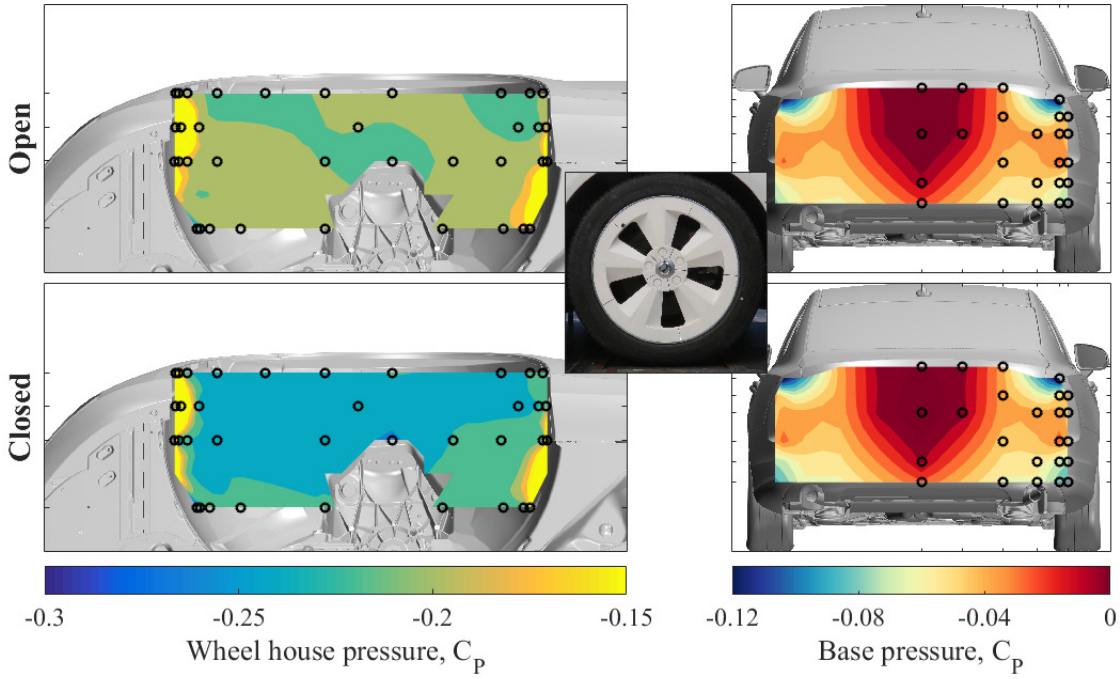

Figure B.33: D29. The wheel house and base pressure for open and closed cooling flow.

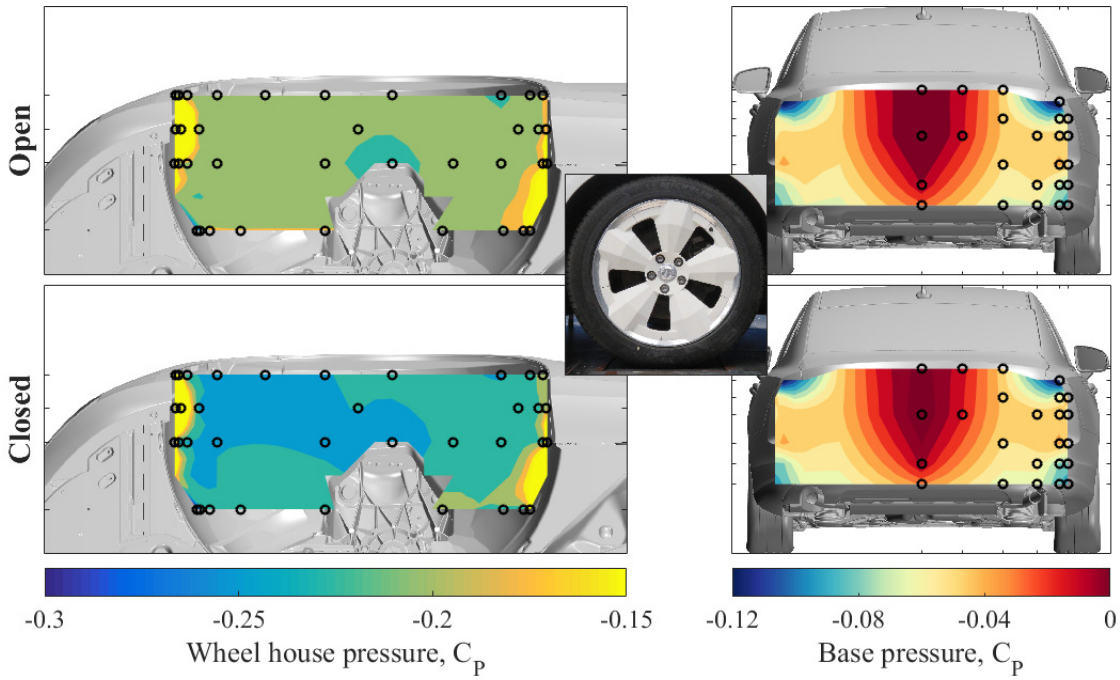

Figure B.34: D30. The wheel house and base pressure for open and closed cooling flow.

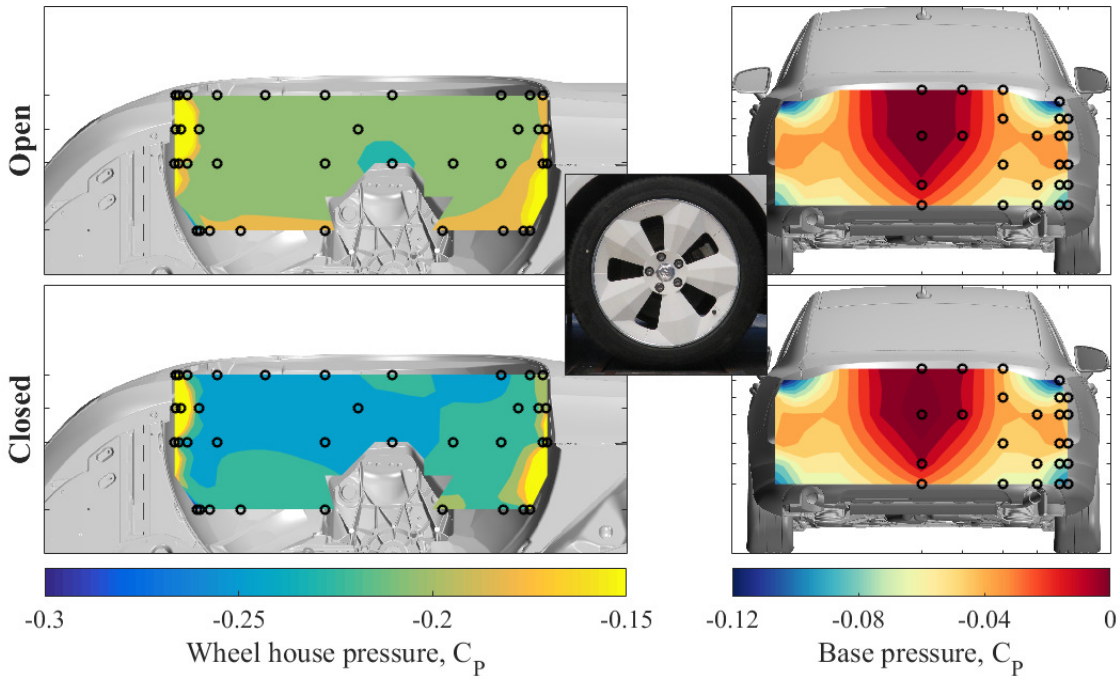

Figure B.35: D31. The wheel house and base pressure for open and closed cooling flow.

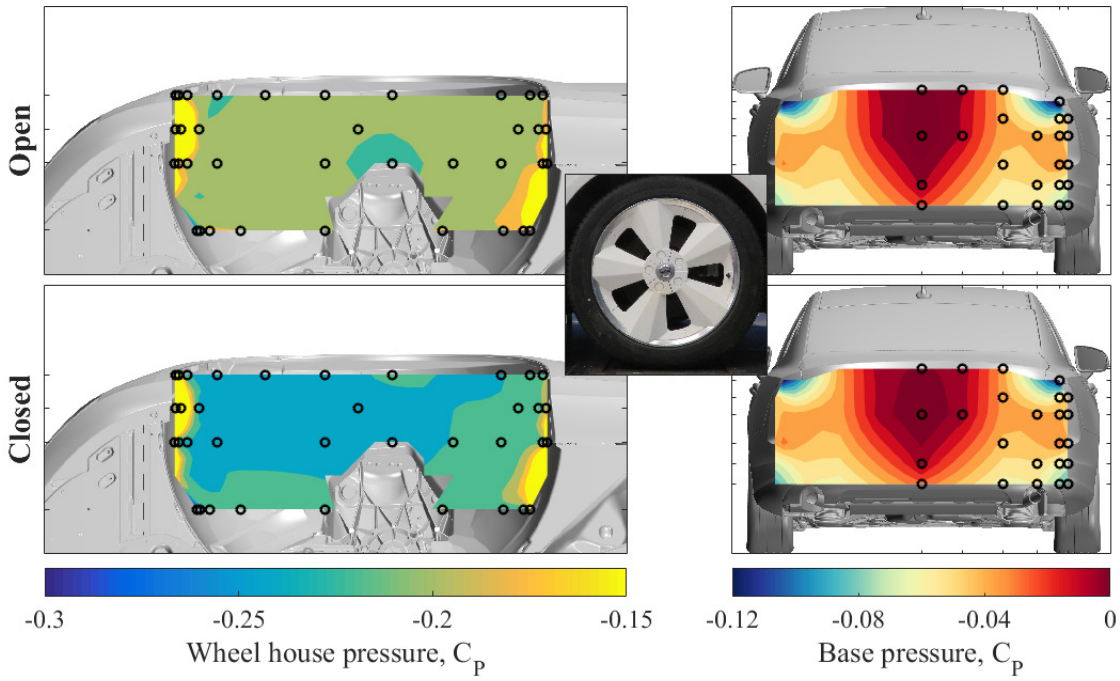

Figure B.36: D32. The wheel house and base pressure for open and closed cooling flow.

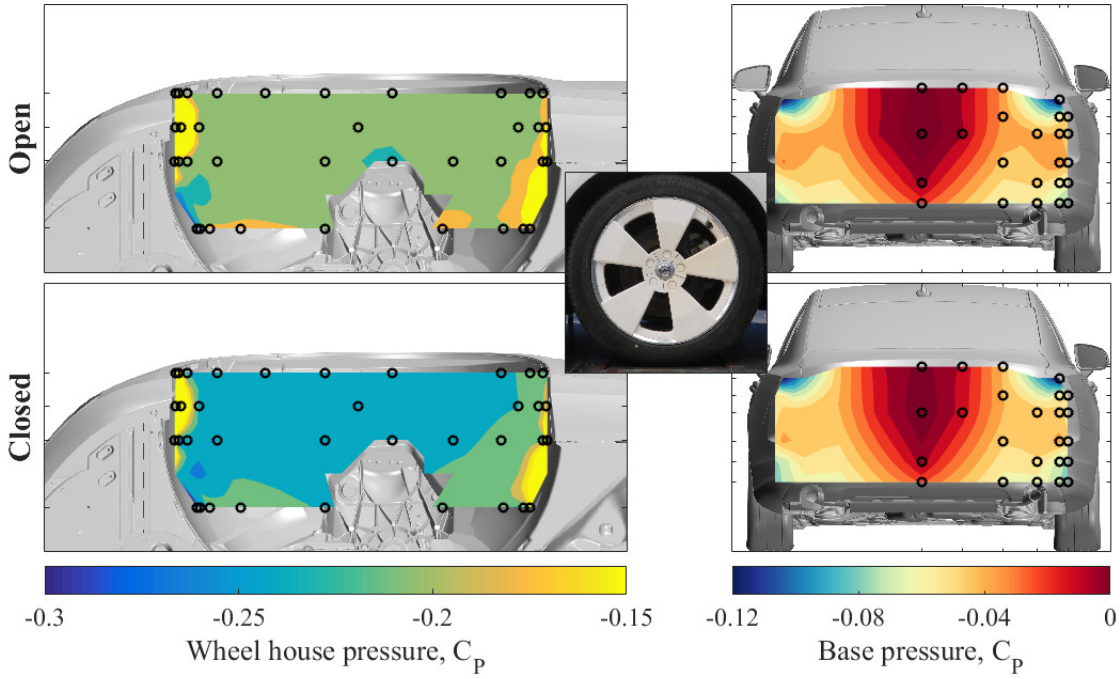

Figure B.37: D33. The wheel house and base pressure for open and closed cooling flow.

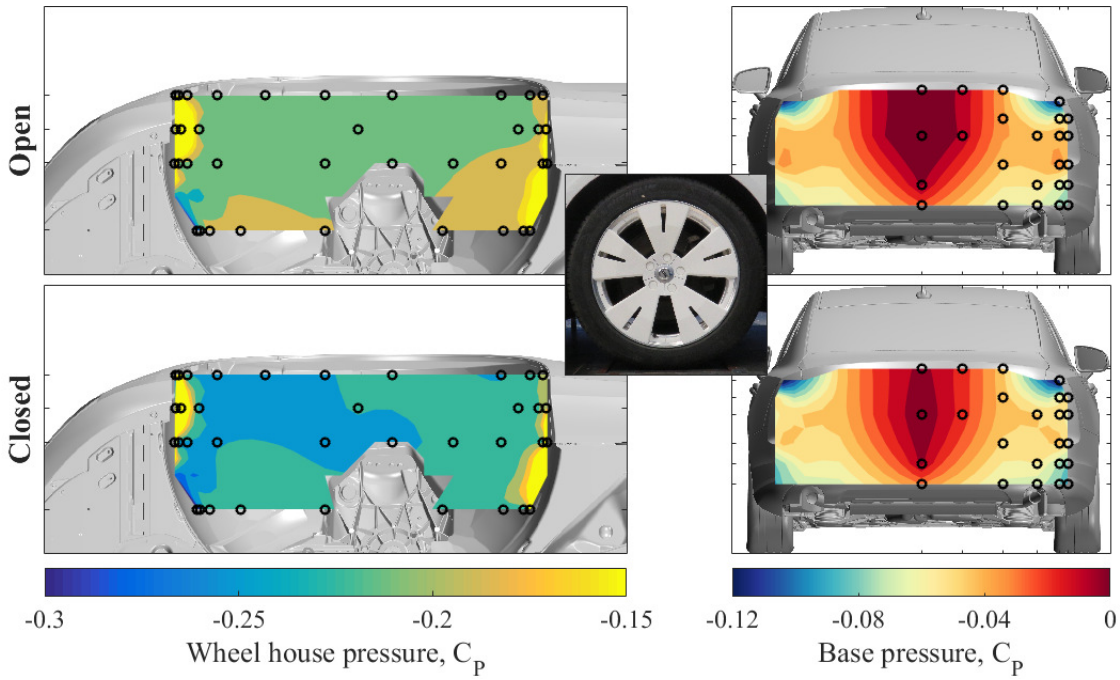

Figure B.38: D34. The wheel house and base pressure for open and closed cooling flow.

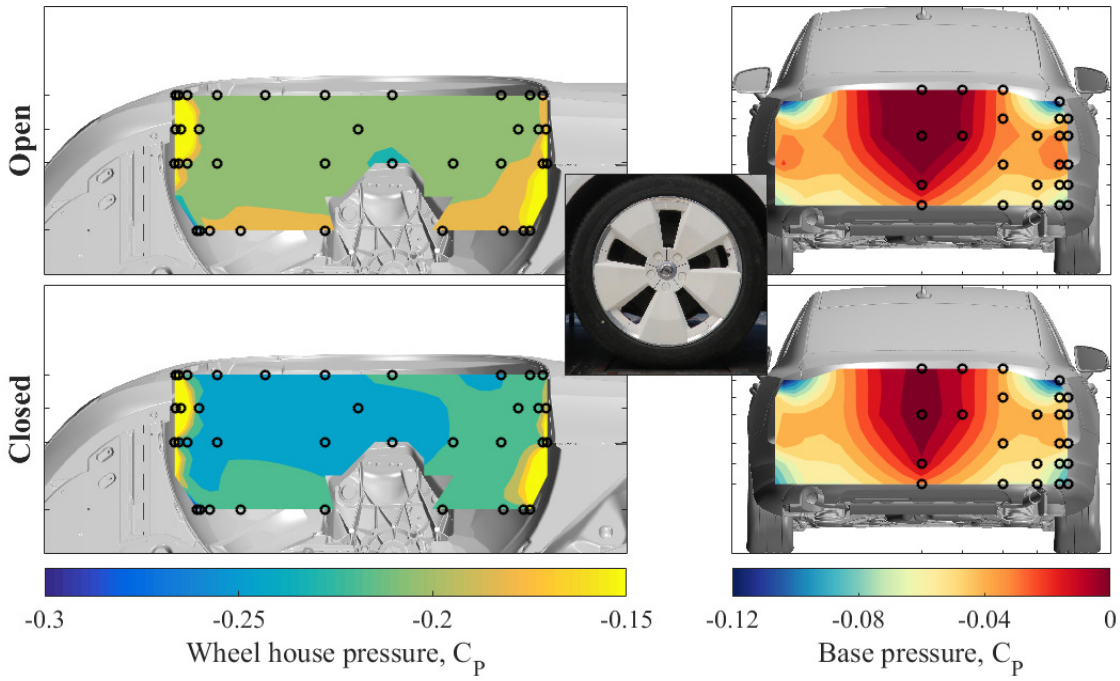

Figure B.39: D35. The wheel house and base pressure for open and closed cooling flow.

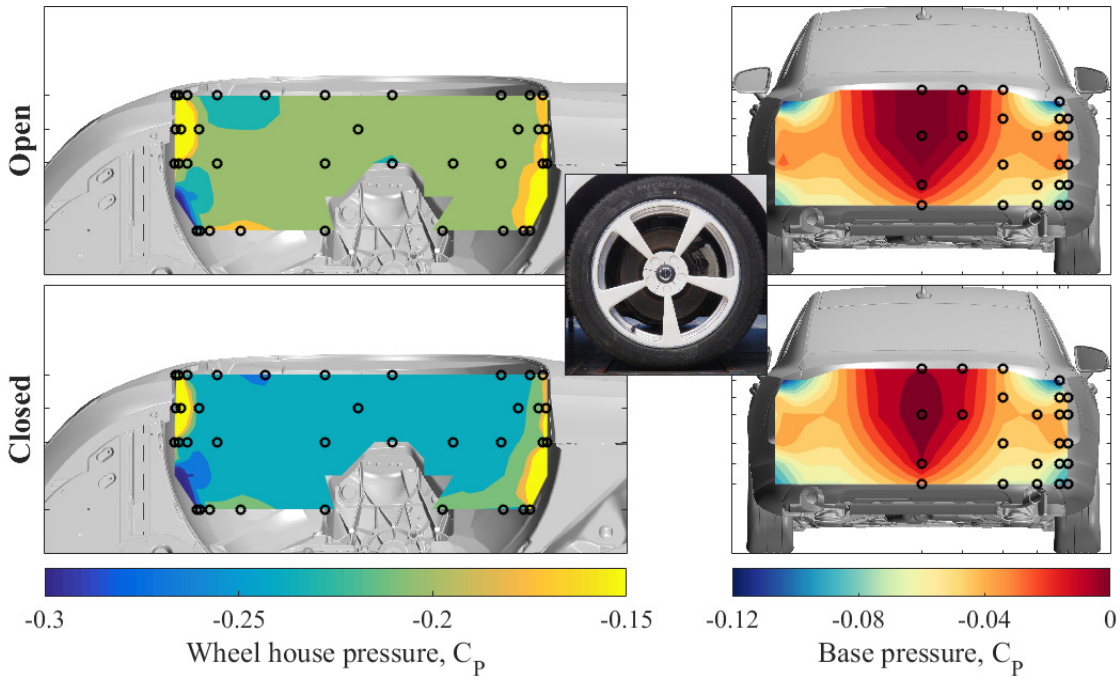

Figure B.40: D36. The wheel house and base pressure for open and closed cooling flow.

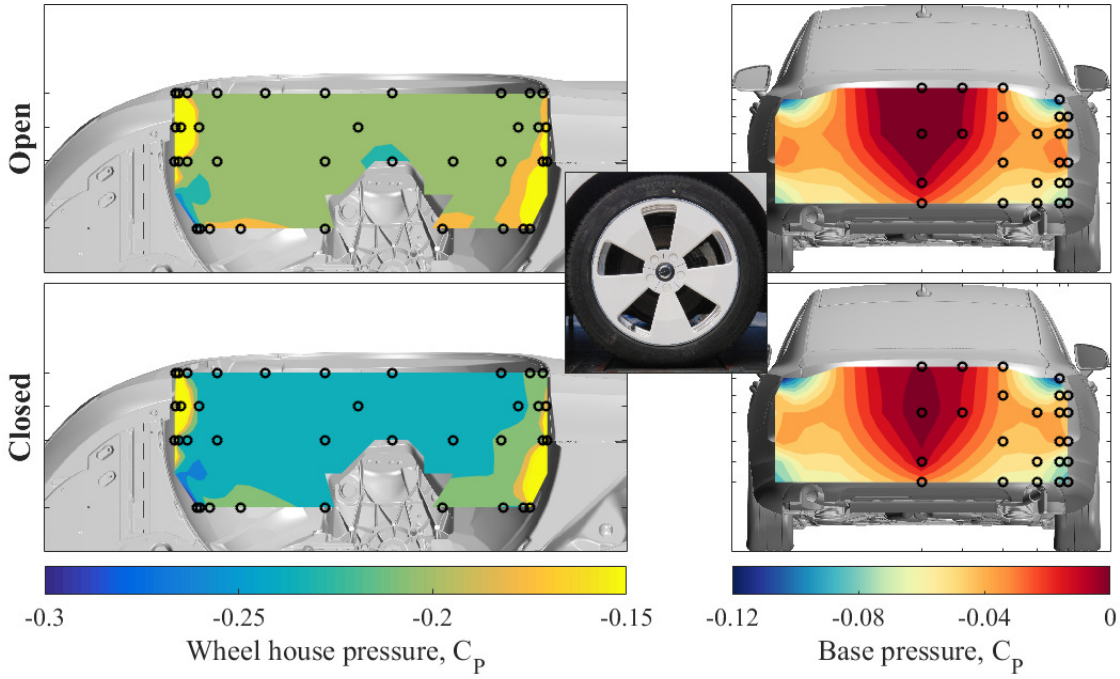

Figure B.41: D37. The wheel house and base pressure for open and closed cooling flow.

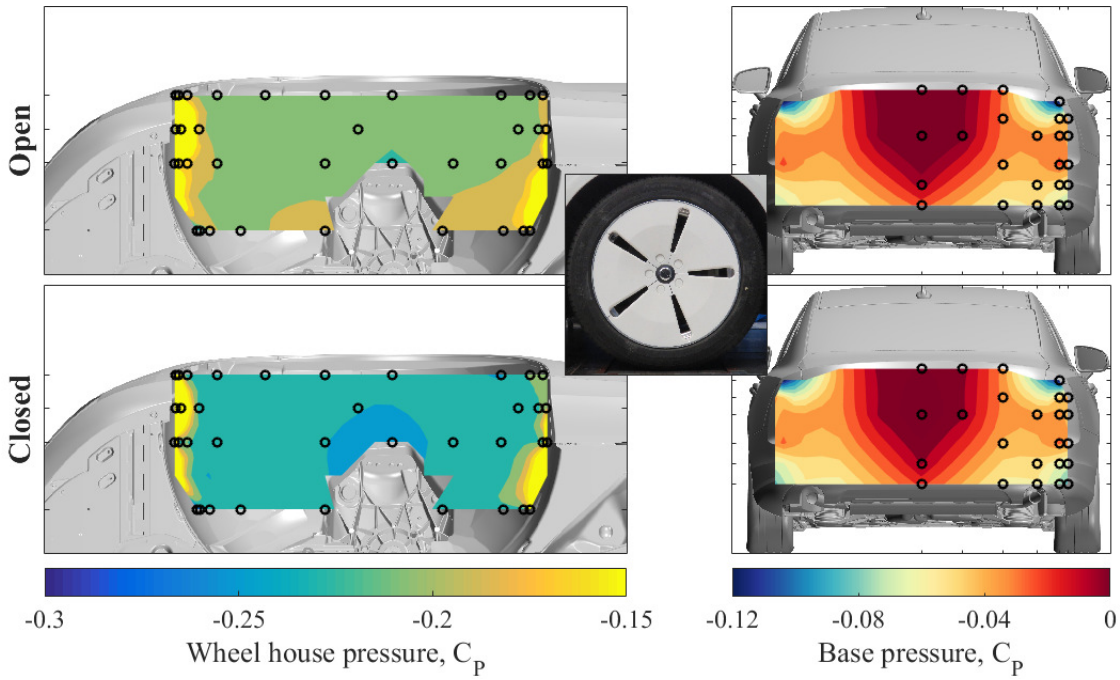

Figure B.42: D38. The wheel house and base pressure for open and closed cooling flow.

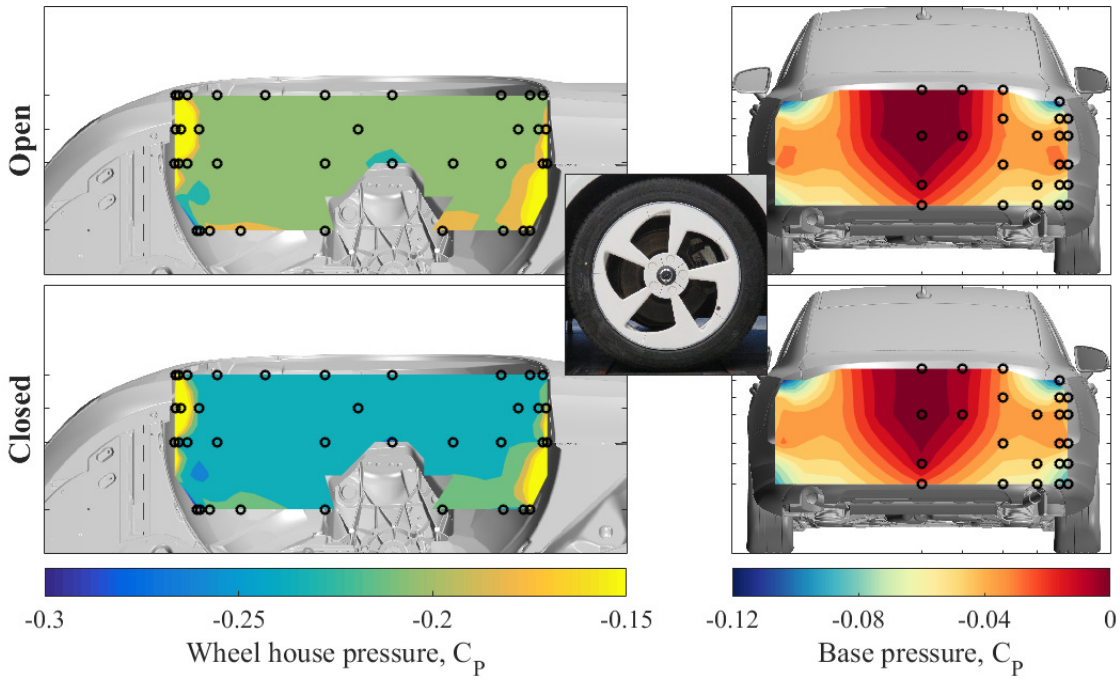

Figure B.43: D39. The wheel house and base pressure for open and closed cooling flow.

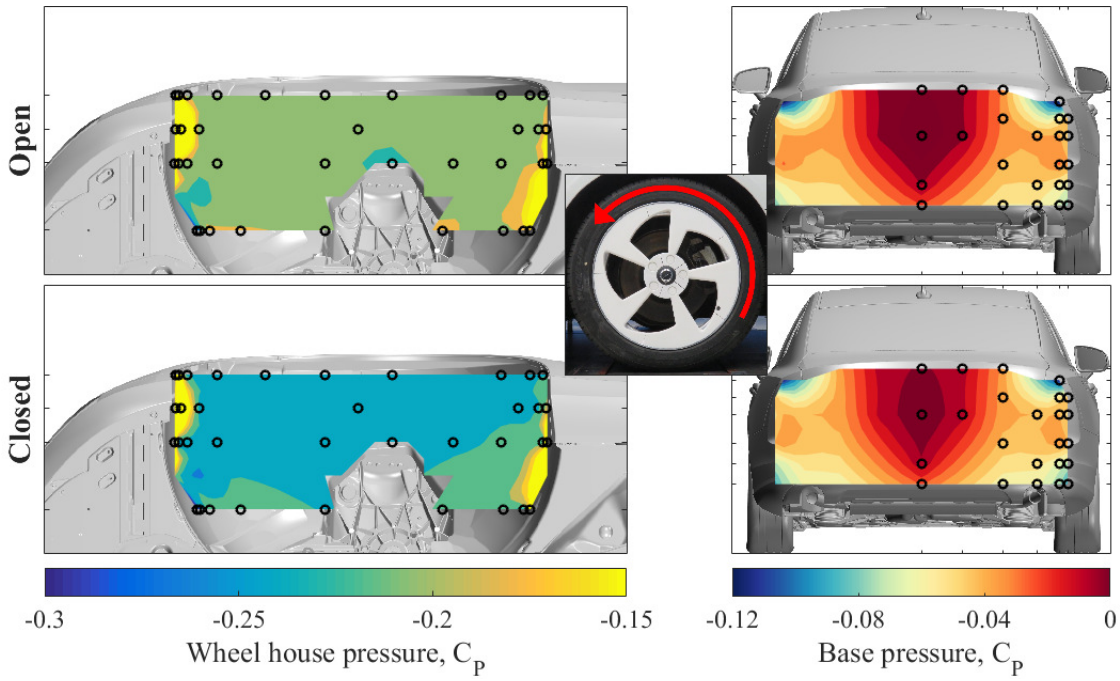

Figure B.44: D40a. The wheel house and base pressure for open and closed cooling flow.

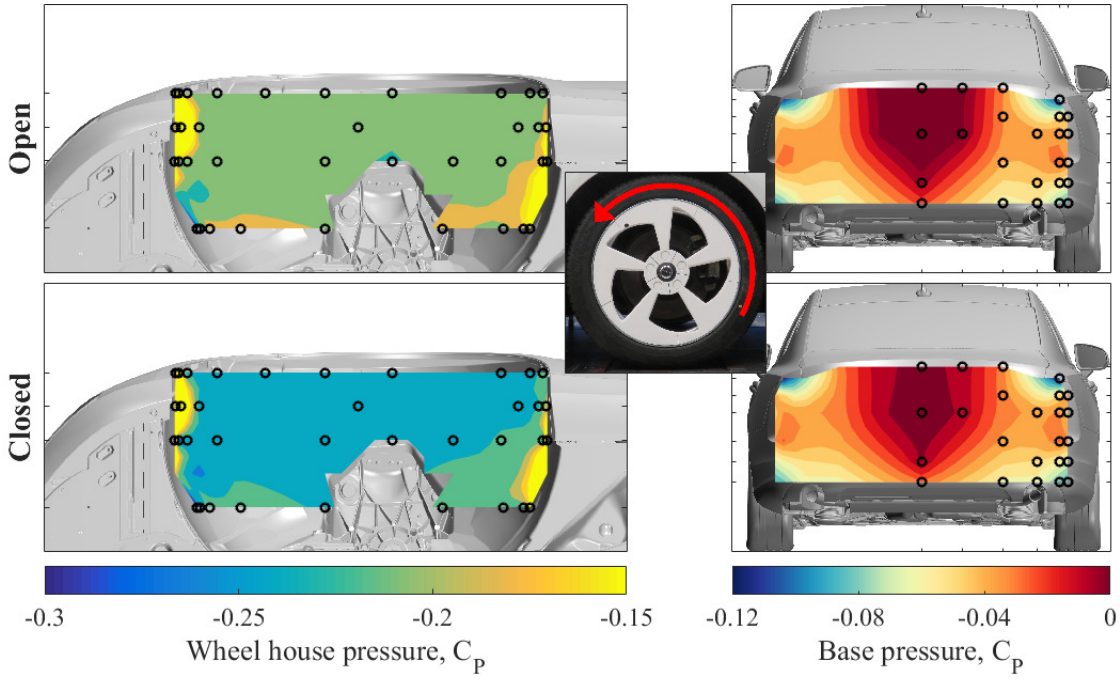

Figure B.45: D40b. The wheel house and base pressure for open and closed cooling flow.

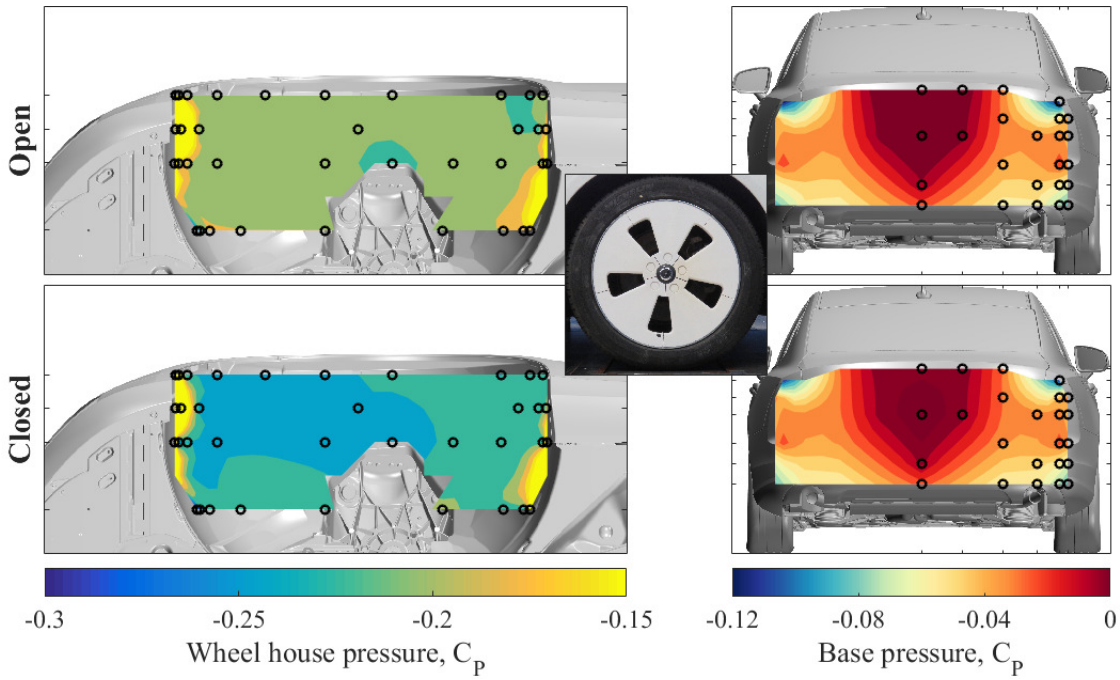

Figure B.46: D41. The wheel house and base pressure for open and closed cooling flow.

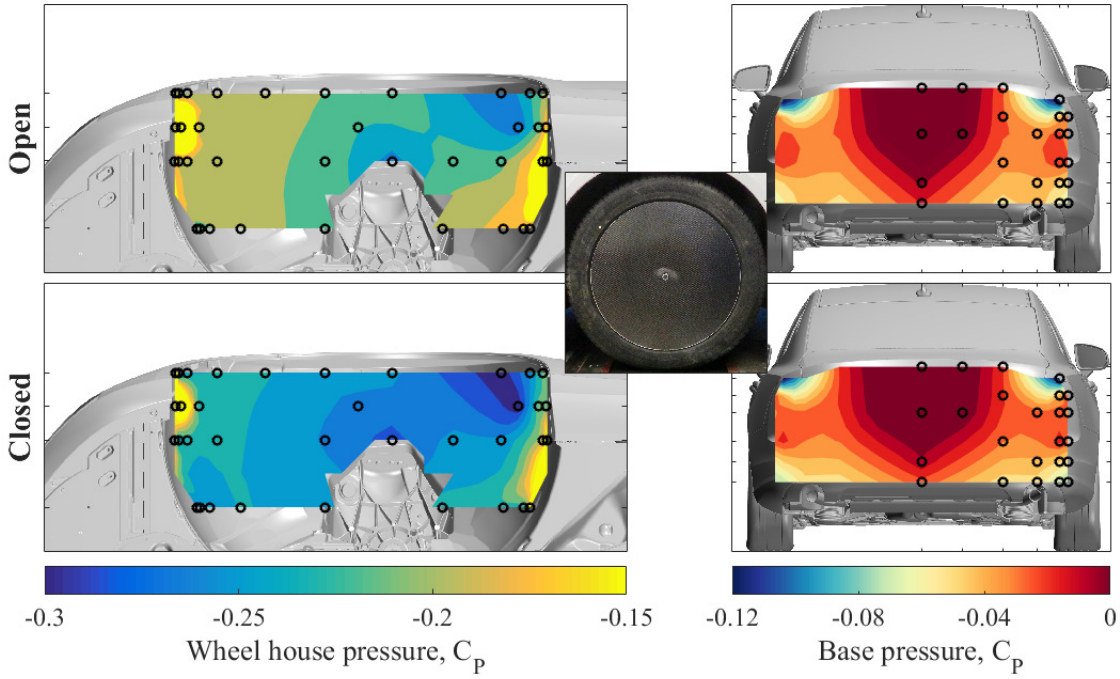

Figure B.47: D41 - Covered. The wheel house and base pressure for open and closed cooling flow.